Arcing in Very Large Area Plasma-Enhanced Chemical Vapour Deposition Reactors

THÈSE N^{O} 5090 (2011)

PRÉSENTÉE LE 30 JUIN 2011

À LA FACULTÉ SCIENCES DE BASE
CENTRE DE RECHERCHES EN PHYSIQUE DES PLASMAS
PROGRAMME DOCTORAL EN PHYSIQUE

ÉCOLE POLYTECHNIQUE FÉDÉRALE DE LAUSANNE

POUR L'OBTENTION DU GRADE DE DOCTEUR ÈS SCIENCES

PAR

Boris LEGRADIC

acceptée sur proposition du jury:

Prof. G. Meylan, président du jury
Dr C. Hollenstein, Dr A. Howling, directeurs de thèse
Prof. C. Ballif, rapporteur
Prof. J.-P. Booth, rapporteur
Dr C. Ellert, rapporteur

ÉCOLE POLYTECHNIQUE
FÉDÉRALE DE LAUSANNE
Suisse
2011

Abstract

This thesis presents an investigation into arcing and parasitic plasmas in large area plasma enhanced chemical vapour deposition reactors. Two types were investigated: RF breakdown in millimetric gaps in absence of plasma (e.g. dark space shielding), in a millibar pressure range, and RF hollow cathodes in glow discharges. RF breakdown curves (voltage vs. pressure) for parallel plate electrodes generally show a steep left-hand branch at low pressures and a flatter right hand branch at higher pressures. Introducing protrusions or holes in parallel plate electrodes will lower the breakdown voltage in certain conditions. This is, however, not due to the increased electric field at sharp edges or ridges. Instead, both experiments and simulation show that breakdown at high pressure will occur at the protrusion providing the smallest gap, while breakdown at low pressure will occur in the aperture providing the largest gap. This holds true as long as the feature in question is wide enough: Features that are too narrow will lose too many electrons due to diffusion, either to the walls of the apertures or to the surroundings of the protrusion, which negates the effect on the breakdown voltage. An analytical approximation of breakdown in parallel plates with cylindrical protrusions supports this argument. The simulation developed to study breakdown in structured parallel plate electrodes also presents a tool to aid the design of complex RF parts for dark-space shielding. A method was developed to measure the pressure-limits of ignition for RF hollow cathodes, and it could be shown that these limits not only depend on gas type, diameter and depth of the hollow cathode, but also on the presence and/or absence of other hollow cathodes in the vicinity. It could also be conclusively shown that hollow cathodes damage the electrode by sputtering and/or evaporation.

Version abrégée

Le propos de cette thèse est l'étude des claquages et des plasmas parasites dans des réacteurs de grande surface utilisés pour les dépôts de type PECVD. Deux phénomènes ont été étudiés: Premièrement le claquage radio-fréquence dans des distances de l'ordre du millimètre, en absence de plasma (p. ex. dark space shielding) et dans une gamme de pression de quelque millibars, et deuxièmement les plasmas parasites génères par des cathodes creuses (hollow cathodes) dans le cadre d'une décharge 'glow'. Les courbes de claquage rf (tension en fonction de la pression) pour des électrodes planes parallèles montrent en général une pente raide dans la zone des basses pressions, et une tendance plate pour les pressions plus élevées. L'introduction de reliefs (trous ou proéminences) sur électrodes planes parallèles entraine une chute de la tension de claquage dans certaines conditions. Cependant, cet effet n'est pas dû au champs électriques élevés associés aux coins ou aux arêtes franches. Les données expérimentales comme les simulations montrent qu'á haute pression les claquages se produisent au niveau de la proéminence la plus grande, (distance inter-électrodes la plus petite), tandis qu'á basse pression ceux-ci se produisent au niveau du trou le plus profond (distance inter-électrode la plus grande). Cette règle n'est valide que si le rapport d'aspect hauteur/largeur du relief est assez petit: En effet, pour un rapport trop grand un grand nombre d'electrons est perdu par diffusion dans les parois internes des trous ou dans l'environnement des proéminences, ce qui annule l'effet de la tension de claquage élevée. Une modèle analytique du claquage entre électrodes planes parallèles avec proéminence cylindriques conforte cet argument. Par ailleurs, nous avons développé une simulation du claquage entre plans parallèles structurés qui se révèle être un outil efficace pour le développement des parties complexes des électrodes vis-à-vis du dark-space shielding. Une

méthode de mesure des limites en pression pour l'allumage des cathodes creuses rf a été développée, et des expériences ont montré que ces limites ne dépendent pas seulement du type de gaz, du diamètre et de la profondeur des cathodes creuses, mais aussi de la présence ou absence d'autres cathodes creuses à proximité. Finalement nous avons mis en évidence le fait que les plasmas parasites liés aux cathodes creuses sont susceptibles d'endommager les électrodes par sputtering et/ou évaporation.

Contents

Chapter 1

Introduction

Chemically reactive plasmas are widely used in industry and research. Uses include, but are not limited to:

- modification of surface properties
- deposition of thin films
- cleaning and etching

One important use of plasma-enhanced chemical vapour deposition (PECVD) is the fabrication of thin-film transistor (TFT) displays and photovoltaic solar cells (see figure 1.1) based on amorphous and micro-crystalline silicon. The substrates commonly used have grown from 350 mm x 450 mm in 1992 to 2850 mm x 3050 mm in 2007 [1, 2]. This means a 7-fold growth in diagonal, from half a meter to about 4.2 meters, and an increase of surface area by a factor of 55! This demand for ever-larger substrates, coupled with new production techniques (e.g. the step from amorphous cells to amorphous-micro-crystalline cells for photovoltaics) translates into progressively bigger RF power requirements.

Increasing the production area is unfortunately not so easy as up-scaling existing reactors and using more powerful generators. Edge-effects (for example standing wave effects [3, 4, 5, 6]) have to be taken into account as the reactor dimensions reach a significant fraction of the RF wavelength, and parasitic plasmas as well as arcing can occur in power supply and showerheads. The latter effects can lead to a reduced lifetime, damaged or even destroyed rectors.

Figure 1.1: Final installation and layout of Uni-Solar Ovonicś Thin Film Flexible Solar PV panels. Photographer: Ken Fields.

1.1 Plasma

Plasma is often called the fourth state of matter [8]. If we take any solid and increase its temperature while holding the pressure fixed, it will eventually enter a fluid phase, and then a gaseous phase. Adding more energy will then start to dissociate molecules, if present, and then the constituent atoms or molecules are ionised so that the resulting quasi-neutral gas becomes highly conductive and responsive to magnetic fields. First described in a lecture by Sir William Crookes [9] as *radiant matter*, and further by J.J. Thomson [10] in 1879, the phenomenon was finally given its name *plasma* by I. Langmuir [11] in 1928.

To generate a plasma, energy has to be introduced into a gas until a certain fraction of the neutral particles are ionised. When the sphere around a particular particle, with the radius of the Debye-length

$$\lambda_{\mathrm{D}} = \sqrt{\frac{\varepsilon_0 k_{\mathrm{B}} T_{\mathrm{e}}}{n_{\mathrm{e}} e^2}} \tag{1.1}$$

contains an average number of charge carriers greater than one, i.e. the plasma parameter

$$N_{\mathrm{D}} = \frac{4\pi}{3} n \lambda_{\mathrm{D}}^3 > 1, \tag{1.2}$$

and the Debye length is smaller than the physical dimensions of the system in question, we call the gas a weakly coupled plasma, the kind of plasma the present work is concerned with. Here ε_0 is the permittivity of free space,

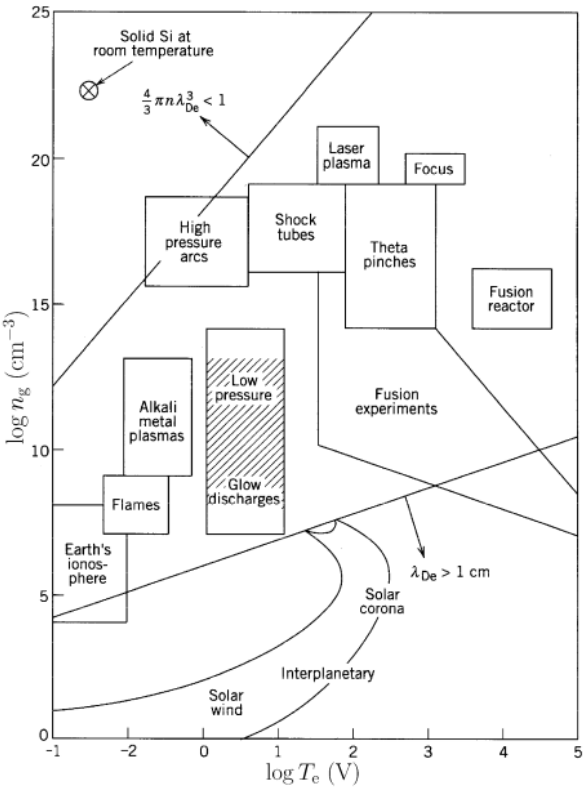

Figure 1.2: Various types of plasmas on a log-log scale, plasma density n_g versus electron temperature T_e (after [7]). λ_{De} is the Debye-length.

Parameter	Capacitive discharge	High density discharge
Pressure (mbar)	0.01-5	0.05-70
Frequency (MHz)	0.1-67.8	0-2450
Area (m^2)	0.03-4	0.03-0.05
Plasma density n (cm^{-3})	10^9-10^{11}	10^{10}-10^{12}
Electron temperature T_e (V)	1-5	2-7
Ionisation	10^{-6}-10^{-3}	10^{-4}-10^{-1}

Table 1.1: Range of parameters for capacitively coupled and high density discharges

k_B is the Boltzmann constant, T_e the electron temperature, n_e the electron density and e the elementary charge.

Ionising neutrals can be done in many different ways, from heat to electron beams, lasers and electrical fields. Most industrial plasmas employ the latter method, using either DC or AC electromagnetic fields to transfer energy to intrinsic free electrons or ions in the gas, which in turn ionise more neutrals to form a plasma.

In the simplest case, a plasma then consists of a gas of neutral particles A, positive ions A^+ and negative electrons e^-. Despite the charged particles, the plasma as a whole is neutral, giving rise to the term of quasi-neutrality. While local variations may produce space-charges, taken in its entirety the discharge has to consist of an equal number of positive and negative charges. Given a plasma of multiple species of neutrals A_m and ions A_m^{k+} we get

$$n_e = \sum_{k,m} k n_{A_m^{k+}}, \tag{1.3}$$

with $n_{A_m^{k+}}$ the density of the m-th species, ionised k times. Since some molecules of electronegative gases tend to form negative ions via attachment, equation 1.3 has to take them into account, and with $n_{A_m^{k-}}$ the negative ion densities, the charge balance is

$$n_e + \sum_{k,m} k n_{A_m^{k-}} = \sum_{k,m} k n_{A_m^{k+}}. \tag{1.4}$$

The properties of the generated plasma depend on the density and type of the neutral gas, the material and shape of the boundaries and the amount and method of energy input. Plasmas exist over an enormous range of parameters, as shown in figure 1.2, which shows laboratory and space plasmas over a range of 7 orders of magnitude for the electron temperature T_e, and 21 orders of magnitude for the plasma density n.

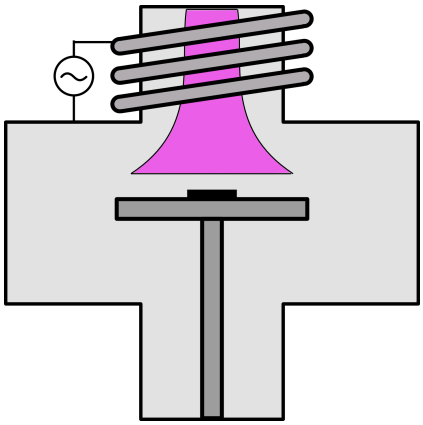

Figure 1.3: Schematic view of an inductively coupled plasma.

In this work we will mainly deal with weakly ionised, electro-positive plasmas, (hatched area in figure 1.2), where we can use equation 1.3 with only one or two species.

1.1.1 RF plasmas

Radio frequency plasmas use a high frequency (multiple megahertz) electric field to transfer energy to the plasma. The energy couples into the plasma mainly via electrons, the ions being to heavy to accelerate during the short time of one RF period. There are two main types, inductively coupled and capacitively coupled plasmas. Inductively coupled plasmas use an antenna emitting high-frequency RF radiation to induce electric currents in the plasma, thereby supplying it with energy. Figure 1.3 shows a schematic of an inductively coupled reactor: the antenna is wound around the top of the vacuum chamber, producing a plasma that reaches down to the substrate. Inductively coupled plasmas can reach relatively high electron density (on the order of 10^{15} cm^{-3}), and benefit from the possibility of locating the antenna outside the discharge chamber, which avoids a possible source of contamination. On the other hand, it is difficult to use inductively coupled sources for uniform large area deposition.

Capacitively coupled plasmas take their name from using a configuration similar to a capacitor: A flat, planar electrode (see figure 1.4) driven by an RF power supply, separated by the discharge gap from the grounded electrode. The energy is coupled into the plasma by the electric field generated between the electrode, which rapidly oscillates the electrons in the gas or plasma.

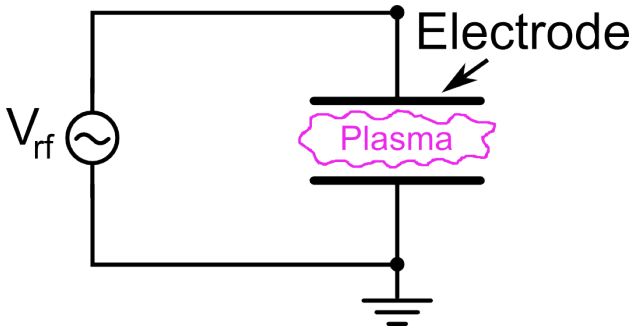

Figure 1.4: Schematic view of a capacitively coupled plasma.

1.1.2 Plasma Parameters for Industrial Plasmas

For the low-pressure discharges commonly used in industrial plasma applications the plasma is not in thermal equilibrium. Electrons and ions are decoupled, with the ions and neutrals assuming a temperature near room temperature (0.026 eV; 1 eV $\sim$ 11600 K), or the temperature of the heated reactor, which in deposition-plasmas is around 250 centigrade. The electrons absorb the biggest part of the electrical power, and transfer it only inefficiently to ions and neutrals via collisional processes. This means the electron temperature T_e is much higher than the ion and neutral temperatures T_i and T, typically attaining between 2 and 5 eV.

The plasma density can vary over several orders of magnitude, with lower densities predominantly used in large area plasma enhanced chemical vapour deposition, and for sterilising plasmas, while higher densities are more common in etching applications. The degree of ionisation also varies greatly, with capacitive discharges for deposition at the low end, while helicon and inductive discharges as well as DC arc plasmas can reach a very high degree of ionisation.

1.1.3 Dark space shielding

In the design of plasma-enhanced chemical vapour deposition (PECVD) reactors there are instances where the working gas will have to flow between parts of the RF electrode and grounded surfaces, or areas where it is not possible to isolate RF parts from grounded parts via the use of a dielectric. An example of the latter occurs in PECVD reactors for silicon deposition, where the cleaning process involves fluorine-plasma (SF_6 or F_2) which are too aggressive for any dielectric except for alumina, which cannot stand up to the thermal expansion of the machine during operation. The solution to this problem is dark space shielding [12], small gaps in the range from one

to a few millimetres. These gaps are supposed to be small enough so that no glow discharge can form, but wide enough to avoid problems of mechanical tolerance and thermal expansion, as well as to limit large capacitive currents and prevent metal vapour arcing due to field emission. RF breakdown in these small gaps is of high interest to the thin-film industry, since arcing and parasitic plasmas in small gaps in PECVD reactors can represent a failure point preventing the up-scaling to larger substrates and/or higher power regimes for micro-crystalline silicon deposition. The ignition of these parasitic plasmas can result in uneven distribution of RF currents and therefore non-uniform deposition at best to the destruction of the reactor at worst. To properly design such gaps, it is important to understand the mechanisms which result in breakdown, especially in geometries more complex than the much-studied parallel-plate breakdown.

1.2 Objectives

The objectives of this thesis are to investigate the arcing and parasitic plasma events in very large area reactors. Arcing can damage the reactor itself, while parasitic plasmas disturb the deposition process. Both restrict the parameter space available for the process in terms of power and pressure. These events are most likely the result of multiple fundamental physical phenomena. Those phenomena should therefore be isolated and investigated. With these results in mind, a way should be found to push the parameter space in which the reactor can operate to higher powers and/or pressures and to prevent arcing and parasitic plasma events from damaging the reactor or disrupting the deposition process.

Members of the industry [13] identified four tentative 'families' of parasitic plasma in their reactors:

1. RF breakdown in micron gaps between surfaces which are nominally in contact
2. RF non-contact breakdown across gaps (mm, cm) in absence of plasma
3. RF plasma hollow cathodes
4. RF plasma with insulating layers & DC circulating currents

The present work concentrates on 2) RF non-contact breakdown across gaps (mm, cm) in absence of plasma, in particular on the effects of structures, i.e. holes or protrusions on the breakdown curve. This is not the same as vacuum breakdown which depends mainly on field emission. To a lesser degree 3) RF plasma hollow cathodes are briefly considered in chapter 6.

1.3 Organisation

This work is organised as follows: After the present introduction, the breakdown theory for DC and RF plasmas is presented, with a special focus on capacitively coupled RF breakdown. Breakdown conditions for 1d and 2d parallel plate RF breakdown are derived, as well as a method for stating the drift-diffusion equation for arbitrary electric fields in 2d. The next chapter gives an overview of the experimental setup, such as working gases and pumps, electrical characteristics, matching and automation, as well as the various diagnostics (voltage probes, breakdown detection and optical spectroscopy) used. Then the main experimental results for RF breakdown between parallel plates are shown, for plane parallel plates and structured parallel plates. The influence of different structural elements on the breakdown voltage is discussed, together with the influence of the gas type and the electrode material. The chapter finishes with an analytical discussion and physical interpretation of the results. After that, a chapter on breakdown simulation introduces 1d and 2d drift-diffusion simulations, and compares their prediction of breakdown voltage with that of experimental results. The influence of the swarm parameters (electron drift velocity, diffusion and Townsend coefficient) on the breakdown voltage is shown. The penultimate chapter deals with hollow cathode discharges, discussing the detection of sputtered/evaporated material from the discharge, and their prevention in industrial plasma reactors. Lastly, in the conclusion, the most important results are summarised and further work is discussed.

Chapter 2

Plasma Breakdown Theory

In this chapter the theoretical background for plasma breakdown is presented for both DC and capacitively coupled RF plasmas. Breakdown conditions can be found analytically for DC plasmas, and with certain approximations also for RF breakdown in 1d and 2d parallel plate cases. With the help of these conditions it is easy to find approximate values for parallel plate experiments, and, as will be shown in chapter 4, they can even give an indication of the minimum breakdown voltage for more complex geometries.

2.1 DC Plasma Breakdown

Before concentrating on breakdown for capacitively coupled plasmas, it is instructive to look at the breakdown of a DC discharge, as it is both historically important and in a way simpler than an RF discharge, as it has no macroscopic time dependency [8]. The usual configuration is a long glass cylinder, with the (positive) anode at one and the (negative) cathode at the other end. A voltage of typically a few hundred volts is applied between the two electrodes. Figure 2.1 shows the general characteristics of such a discharge.

Unlike the capacitively coupled RF discharge (discussed below), a DC discharge depends very much on ions for breakdown. Incident ions in the gas are accelerated by the applied electric field until they impact the cathode. If their impact energy is sufficient, i.e. the applied voltage is high enough, they will produce secondary electrons, which are then accelerated back to the anode, ionising more gas molecules. The threshold condition for DC breakdown requires each ion to produce enough secondary electrons for at least one neutral molecule to be ionised before the electrons reach the anode.

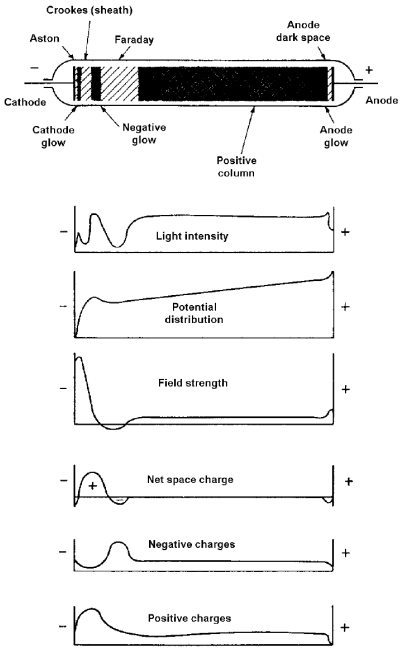

Figure 2.1: A direct current discharge, qualitative characteristics, from [8].

Therefore, DC breakdown is strongly dependent on both cathode material and neutral gas, as shown in figure 2.2.

The breakdown curve for DC breakdown is commonly known as *Paschen curve*, and when plotted as breakdown voltage over the product of electrode distance and pressure pd, different electrode distances will nevertheless result in the same curve: the breakdown voltage is mostly dependent on pd.

Kihara [15] presented a mathematical model for breakdown in microwave, RF and DC discharges. In a discharge with the electrode gap length d and an applied electric field E, an electron emitted from the cathode will ionise $e^{\alpha d}$ neutrals, where α is the third Townsend coefficient. The number of positive ions created is therefore $e^{\alpha d} - 1$, which, with the threshold condition mentioned above gives the breakdown condition

$$\gamma_{\mathrm{i}} \left[e^{\alpha d} - 1 \right] = 1 \tag{2.1}$$

where γ_{i} is the secondary electron emission coefficient for ions (or second Townsend coefficient), the number of electrons emitted via the impact of one ion at the cathode. We can write the above equation 2.1 as

$$\alpha d = \Gamma, \quad \text{where} \quad \Gamma = \ln \left(\frac{1 + \gamma_{\mathrm{i}}}{\gamma_{\mathrm{i}}} \right). \tag{2.2}$$

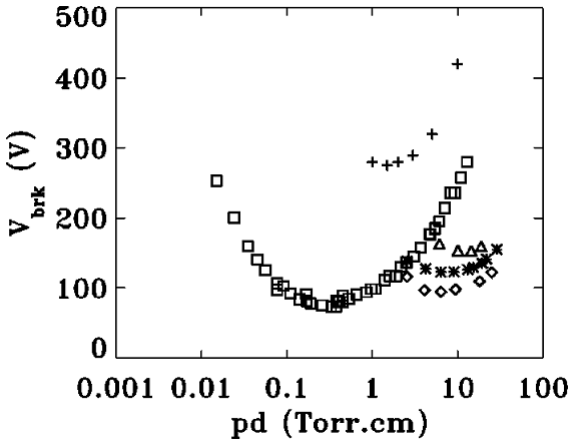

Figure 2.2: Comparison between capacitively coupled RF breakdown curve (□, 10 cm electrode separation, 13.56 MHz) and DC paschen curves, both in argon. The DC curves are shown for different materials: iron (+), aluminium (△), magnesium (*) and barium (♢). From [14].

This process is also called γ-process. Its physical mechanisms are fairly involved; photoemission and electron emission via excited neutrals in metastable states can also play a large role in the production of electrons at the cathode besides ion impact. But since equation 2.2 shows that the breakdown voltage is fairly independent of changes in γ_{i}, we can, together with the third Townsend coefficient given by

$$\alpha = A_0 p e^{\frac{-B_0 p}{E}} \tag{2.3}$$

with A_0, B_0 molecular constants, arrive at an expression for the breakdown voltage V_{bd}:

$$V_{\mathrm{bd}} = \frac{B_0 pd}{\ln \frac{A_0 pd}{\Gamma}} \tag{2.4}$$

Like the experimental results shown in figure 2.2, this expression depends on pd, as well as on γ_{i} for DC breakdown.

2.2 Capacitively Coupled RF Breakdown

In contrast to the DC breakdown discussed above, ions play only a very minor role in capacitively coupled RF breakdown. Usually the frequency of the RF electric field is so high that the ions vibrate more or less in place: from first

principles, by equating the electric force acting on a charged particle with Newton's second law of motion, $ma = qE_0 \sin(\omega t)$ and integrating we get the displacement in time

$$s(t) = \frac{-qE_0}{m\omega^2} \sin(\omega t) \tag{2.5}$$

and the oscillation amplitude A=max($s(t)$) of

$$A = \frac{qE_0}{m\omega^2}, \tag{2.6}$$

with q the charge of the particle, m its mass and E_0 the amplitude of the RF electric field. For example, an applied electric field with an amplitude of 10 kV/m at 40.68 MHz would result in an oscillation amplitude of 0.4 μm for Ar^+. The maximum kinetic energy reached by the ions in this oscillation is

$$E_{\text{kin}}^{\max} = \frac{m v_{\max}^2}{2} = \frac{q^2 E_0^2}{2m\omega^2} = \frac{mA^2\omega^2}{2} \tag{2.7}$$

or 615 μeV in the example above, not enough by far for an ionising collision.

Plasma ignition via RF electromagnetic fields depends therefore on an electron avalanche. Free electrons are accelerated by the field, until they have enough energy to ionise neutrals, producing secondary electrons that ionise more neutrals in turn. This process is called a Townsend avalanche, and is the dominant process for the pressure ranges discussed in this work, i.e. tenths to tens of millibars. At low pressures ($\lesssim$ 1 mbar, depending on the geometry of the electrodes) surface effects like secondary electron emission start to play a role, and become dominant for multipactor breakdown [16, 17] in the Pascal range.

Ignoring surface-effects for the moment, breakdown happens as follows: The gas in the vacuum chamber contains a few free electrons, for example due to ionisation by cosmic radiation. Said electrons are accelerated by the applied electric field. If they become fast enough, i.e. the energy of at least some electrons surpasses the ionisation energy of one of the neutral species, ionisation and diffusion (and possibly volume recombination, depending on the neutral gas) are the two competing processes determining further evolution of the proto-discharge. If diffusion prevails, the Townsend-avalanche does not start, and no breakdown happens. If ionisation prevails, the avalanche is launched, and breakdown achieved. The electrons, much lighter and therefore faster than the ions, are quickly lost to the electrode walls, and the positive ions generate a space charge, forming the sheath-bulk-sheath structure which characterises a plasma discharge [8, 18].

The breakdown process is rapid ($< 1\ \mu s$, [19]), and was first described analytically by Kihara in 1952 [15]. An approximate analytical expression for the breakdown voltage can be found as follows:

Since, as shown above, ions cannot play a big role in RF breakdown, due to their low kinetic energy, we can disregard them completely, and start with the electron continuity equation

$$\frac{\partial n_\mathrm{e}}{\partial t} + \nabla \cdot \mathbf{\Gamma} = \nu_\mathrm{i} n_\mathrm{e}. \tag{2.8}$$

Here n_e is the electron density and $\mathbf{\Gamma}$ the electron flux. The source term on the right-hand side consists of the ionisation frequency ν_i times the electron density. The electron flux can be expressed as $\mathbf{\Gamma} = n_\mathrm{e}\mathbf{V}_\mathrm{e}$ with $\mathbf{V}_\mathrm{e}$ the mean electron velocity. If we regard electrons as a fluid, we can further split the electron flux in a convective and a diffusive part: $\mathbf{\Gamma} = n_\mathrm{e}\mathbf{V}_\mathrm{e} + \mathbf{j_e}$, where $\mathbf{V}_\mathrm{e}$ is the electron fluid drift velocity and $\mathbf{j_e}$ the diffusive flux. The drift velocity can be written as $\mathbf{V}_\mathrm{e} = \mu\mathbf{E}$ by definition of the mobility μ, and according to Fick's law [20] $\mathbf{j_e} = -D\nabla n_\mathrm{e}$, with D the diffusion coefficient, here assumed homogeneous. Putting the above together, the continuity equation 2.8 becomes

$$\frac{\partial n_\mathrm{e}}{\partial t} = \nu_\mathrm{i} n_\mathrm{e} + D\nabla^2 n_\mathrm{e} - \mathbf{V}_\mathrm{e} \cdot \nabla n_\mathrm{e} \cos(\omega t), \tag{2.9}$$

a drift diffusion equation that can be used to write a fluid model to simulate breakdown, see chapter 5.

2.2.1 1d Breakdown Condition

Following Kihara [15] and Lisovskiy et al [21], we can solve equation 2.9 for a parallel plate geometry. We will assume that the voltage that leads to the steady state $\frac{\partial n_\mathrm{e}}{\partial t} = 0$ corresponds to the breakdown voltage, since it clearly delineates between a negative electron growth rate that can never lead to breakdown, and a positive growth rate that must lead to breakdown, multiplying the electron density until the formation of sheaths.

To solve the case for an infinite parallel plate, it is instructive to first take a look at how equation 2.9 behaves for microwaves. In this case, we can neglect the convection term $\mathbf{V}_\mathrm{e} \cdot \nabla n_\mathrm{e} \cos(\omega t)$, since the RF frequency is so high that the electron oscillation amplitude is negligible compared to the gap distance. The differential equation then simplifies to

$$\frac{\partial n_\mathrm{e}}{\partial t} = \nu_\mathrm{i} n_\mathrm{e} + D\nabla^2 n_\mathrm{e}, \tag{2.10}$$

which, using the Ansatz $n_e(z) = n_0 \cos(\lambda z)$ and separation of variables can be shown to have the solution

$$n_e(z,t) = n_0 \cos\left(\sqrt{\frac{\nu_i}{D}} z\right) e^{-kt}, \tag{2.11}$$

the fundamental mode of diffusion, with k the separation constant. Lowering the frequency will reintroduce the convection term, now with $\mathbf{V}_e = \mu E \hat{z} \equiv V_e$ (with $\hat{z}$ the unity vector in z-direction) since we are solving a one-dimensional case:

$$\frac{\partial n_e}{\partial t} = \nu_i n_e + D \frac{\partial^2 n_e}{\partial z^2} - V_e \cos(\omega t) \frac{\partial n_e}{\partial z}, \tag{2.12}$$

and we will have to find a new solution, one that should satisfy both equations 2.12 and 2.10. We look to extend solution 2.11

$$n_e(z) \to n_e\left(z'(z,t)\right) = n_0 \cos\left(\sqrt{\frac{\nu_i}{D}} z'(z,t)\right), \tag{2.13}$$

such that

$$z' = z + f(t), \tag{2.14}$$

in effect demanding that the new solution $n_e(z,t)$ be time-dependent. Inserting this into the diffusion-drift differential equation 2.12 gives us $f(t)$ as

$$f(t) = -\frac{V_e}{\omega} \sin(\omega t). \tag{2.15}$$

Therefore, the electron density between infinitely large parallel plates is

$$n_e(z,t) = n_0 \cos\left[\sqrt{\frac{\nu_i}{D}} \left(z - \frac{V_e}{\omega} \sin \omega t\right)\right]. \tag{2.16}$$

If we assume the plates to be perfect electron absorbers, we get the boundary conditions $n(\pm d/2, t) = 0$. Unfortunately, no closed-form breakdown condition can be obtained. However, a look at what is physically happening in between the electrode plates allows for an important simplification. If we assume the electrodes to be perfect electron absorbers, and disregarding secondary electron emission from the surface, and we furthermore assume that the drift velocity is much larger than the diffusion velocity (which holds true except at low pressures), then the electrons will move as shown in figure 2.3. The empty space between electron cloud and wall will not be filled in one RF cycle, since, as stated above, the drift velocity is much larger than the diffusion velocity. Consequently, we can move our reference frame with the

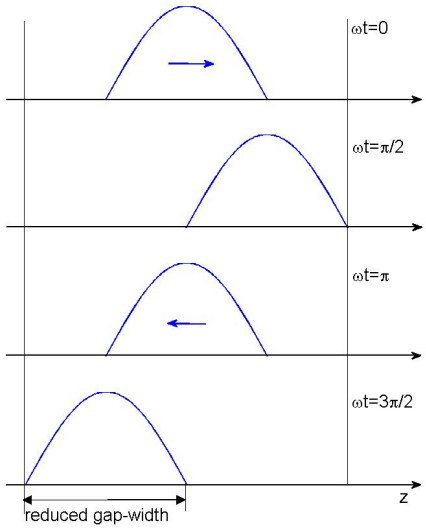

Figure 2.3: Electron density oscillations between parallel plates in an RF cycle.

electron cloud, and therefore treat it as if it was stationary, with a gap width reduced by the oscillation amplitude of the electrons:

$$d' = d - \int_{-\pi/2}^{\pi/2} V_\mathrm{e} \cos(\omega t) dt = d - \frac{2V_\mathrm{e}}{\omega} \tag{2.17}$$

The electron cloud we are treating is now stationary, so there is no electron oscillation to take into account, and we can use the solution of the microwave case (equation 2.11) with the new boundary conditions $n_\mathrm{e}(\pm d'/2) = 0$. This results in the required 1d breakdown condition

$$\frac{1}{\pi^2}\left(d - \frac{2V_\mathrm{e}}{\omega}\right)^2 = \frac{D}{\nu_\mathrm{i}}. \tag{2.18}$$

2.2.2 2d Breakdown Condition

Having found a solution for the one-dimensional problem, we can return to equation 2.9, and search for the two-dimensional solution. Again, we will assume that $\frac{\partial n_\mathrm{e}}{\partial t} = 0$ defines the breakdown condition. Separating the variables so that $n_\mathrm{e}(r, z, t) = R(r)Z(z, t)$, we find we have to solve

$$\frac{D_{\mathrm{T}}}{R}\frac{\partial^2 R}{\partial r^2} + \frac{D_{\mathrm{T}}}{rR}\frac{\partial R}{\partial r} + \nu_{\mathrm{i}} = k^2 \tag{2.19}$$

$$-\frac{1}{Z}\frac{\partial Z}{\partial t} + \frac{D_{\mathrm{L}}}{Z}\frac{\partial^2 Z}{\partial z^2} - \frac{V_{\mathrm{e}}}{Z}\frac{\partial Z}{\partial z}\cos(\omega t) = k^2 \tag{2.20}$$

with k^2 the separation constant. Here the term $\mathbf{V}_{\mathrm{e}} \cdot \nabla[R(r)Z(z,t)]\cos(\omega t)$ from equation 2.9 becomes $V_{\mathrm{e}}\frac{\partial Z}{\partial z}\cos(\omega t)$, as the E-field is taken to be in z-direction, so the drift velocity $\mathbf{V}_{\mathrm{e}}$ only has a component in z.

Solving in R

We can now solve the differential equation in r, rearranging equation 2.19:

$$r^2\frac{\partial^2 R}{\partial r^2} + r\frac{\partial R}{\partial r} + \frac{\nu_{\mathrm{i}} - k^2}{D_{\mathrm{T}}}r^2 R = 0, \tag{2.21}$$

which is Bessel's differential equation [22].

The solution is found to be

$$R(r) = J_0\left(\sqrt{\frac{\nu_{\mathrm{i}} - k^2}{D_{\mathrm{T}}}}r\right), \tag{2.22}$$

and with the cylindrical boundary condition $n_{\mathrm{e}}(R_0, z) = 0$ the separation constant is

$$k^2 = \nu_{\mathrm{i}} - \left(\frac{2.405}{R_0}\right)^2 D_{\mathrm{T}} \tag{2.23}$$

where 2.405 is the first root of the zero-order Bessel function J_0. With equation 2.23 the solution for the R-component of 2.9 is

$$R(r) = J_0\left(\sqrt{\frac{2.405}{R_0}}r\right), \tag{2.24}$$

which is the fundamental diffusion mode distribution (with J_0 the zero-order Bessel function of the first kind) [23].

Solving in Z

Now we can find the solution to the differential equation in z, equation 2.20. Rearranging, we find

$$\frac{\partial Z}{\partial t} = -k^2 Z - D_{\mathrm{L}}\frac{\partial^2 Z}{\partial z^2} + V_{\mathrm{e}}\cos(\omega t)\frac{\partial Z}{\partial z}. \tag{2.25}$$

This is basically the same as the differential equation for 1d, equation 2.12, and we can therefore use the 1d solution, equation 2.16, with the appropriate terms from equation 2.25:

$$Z(z,t) = Z_0 \cos\left[\sqrt{\frac{k^2}{D_\mathrm{L}}}\left(z - \frac{V_\mathrm{e}}{\omega}\sin(\omega t)\right)\right] \tag{2.26}$$

Inserting k^2 from equation 2.23 we find the solution to equation 2.20 as

$$Z(z,t) = Z_0 \cos\left[\sqrt{\frac{\nu_\mathrm{i} - \frac{2.4^2 D_\mathrm{T}}{R_0^2}}{D_\mathrm{L}}}\left(z - \frac{V_\mathrm{e}}{\omega}\sin(\omega t)\right)\right] \tag{2.27}$$

which, together with equation 2.24 gives us the 2d solution as

$$n_\mathrm{e}(r,z,t) = J_0\left(\left(\frac{2.405}{R_0}\right)^2 r\right) Z_0 \cos\left[\sqrt{\frac{\nu_\mathrm{i} - \frac{2.4^2 D_\mathrm{T}}{R_0^2}}{D_\mathrm{L}}}\left(z - \frac{V_\mathrm{e}}{\omega}\sin(\omega t)\right)\right]. \tag{2.28}$$

With the boundary conditions $n_\mathrm{e}(r, \pm d/2, t) = 0$ and the same assumptions as in the 1d case we can then get a 2d breakdown condition:

$$\frac{\nu_\mathrm{i}}{D_\mathrm{T}} = \left(\frac{2.405}{R_0}\right)^2 + \frac{D_\mathrm{L}}{D_\mathrm{T}} \frac{\pi^2}{\left(d - \frac{2V_\mathrm{e}}{\omega}\right)^2} \tag{2.29}$$

Figure 2.4 shows a comparison between this expression and experimental data for parallel plate breakdown of 45 mm radius electrodes with a gap of 4 and 9 mm, in argon. Expression 2.29 is transcendental in the RF voltage V, since the parameters $\nu_\mathrm{i}, D_\mathrm{T}, D_\mathrm{L}$ and V_e are all functions in V. The swarm parameters were accordingly fitted with the expressions shown in section 5.1, and a MATLAB program was written to solve it numerically, by simply starting at a low voltage and stepping the voltage up in a loop until

$$\frac{\nu_\mathrm{i}}{D_\mathrm{T}} - \left(\frac{2.405}{R_0}\right)^2 + \frac{D_\mathrm{L}}{D_\mathrm{T}} \frac{\pi^2}{\left(d - \frac{2V_\mathrm{e}}{\omega}\right)^2} < \xi \tag{2.30}$$

was true, where ξ was an arbitrary parameter, chosen small enough that the step-size had to be below 1 V.

As expected, the left-hand branch of the breakdown curve is not modelled correctly. This is due to surface effects such as secondary electron emission, which the model described above does not take into account, playing a large

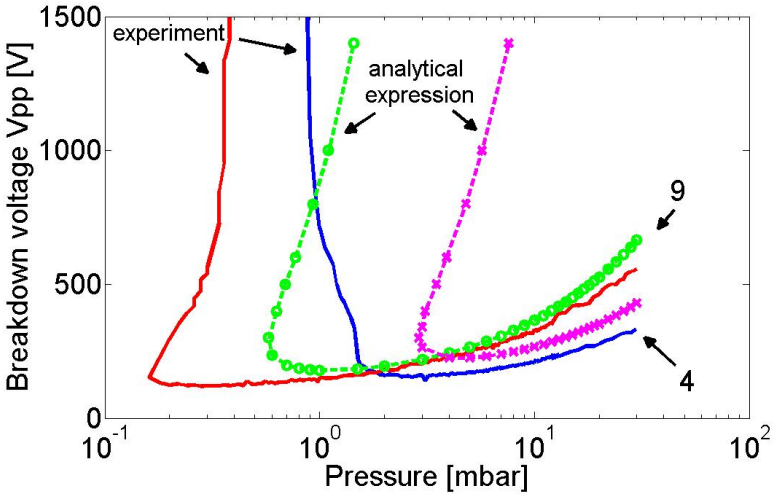

Figure 2.4: Comparison of the 2d breakdown condition 2.29 (broken lines) and experimental data (solid lines) in argon, for 4 and 9 mm (see arrows).

role for low-pressure breakdown. See also section 4.1.2 for comparisons between different electrode materials.

Another feature that can be explained by the lack of an appropriate treatment of surface effects is that breakdown in a 9 mm gap is modelled more accurately than in a 3 mm gap. Since the surface-to-volume ratio in a 3 mm gap is larger, this lack has a larger effect on the accuracy of the model.

2.2.3 Drift-diffusion in 2d with Arbitrary Electric Fields

To develop a simulation for anisotropic diffusion in an arbitrary geometry (see chapter 5) it is useful to generalise the drift-diffusion equation 2.36 [24], by introducing the diffusion tensor $\mathfrak{D}$:

$$\mathfrak{D}_{ij}^{E} = \begin{pmatrix} D_{\mathrm{T}} & 0 \\ 0 & D_{\mathrm{L}} \end{pmatrix} \tag{2.31}$$

aligned with the principal axes of the electric field, where D_{T} is the transversal and D_{L} the longitudinal diffusion coefficient. Then equation 2.9 can be written as

$$\frac{\partial n_{\mathrm{e}}}{\partial t} = \nu_{\mathrm{i}} n_{\mathrm{e}} + \nabla\left(\mathfrak{D} \cdot \nabla n_{\mathrm{e}}\right) - \mathbf{V}_e \cdot \nabla n_{\mathrm{e}} \cos(\omega t). \tag{2.32}$$

We can then use a basis transformation to rotate the diffusion tensor locally to the prevalent electric field. Taking, for example, $\mathbf{E}_i = \begin{pmatrix} E_r \\ E_z \end{pmatrix}$ as a

2d, axisymmetric representation of an electric field with the unit vector $\hat{\mathbf{E}}_\mathbf{i}$, and $\hat{\mathfrak{E}}^{-1}_{ij} = \begin{pmatrix} \hat{E}_r & \hat{E}_z \\ -\hat{E}_z & \hat{E}_r \end{pmatrix}$ the inverse basis transformation, in essence a rotation matrix which rotates a vector along the electric field $\mathbf{E}_i$ back to the r-axis, we get

$$\mathfrak{D}_{ij} = \mathfrak{E}^{-1}_{ik}\mathfrak{E}^{-1}_{jl}\mathfrak{D}^{E}_{lk} = \tag{2.33}$$

$$= \begin{pmatrix} D_\mathrm{L}\hat{E}^2_\mathrm{r} + D_\mathrm{T}\hat{E}^2_\mathrm{z} & \hat{E}_\mathrm{r}\hat{E}_\mathrm{z}(D_\mathrm{T} - D_\mathrm{L}) \\ \hat{E}_\mathrm{r}\hat{E}_\mathrm{z}(D_\mathrm{T} - D_\mathrm{L}) & D_\mathrm{T}\hat{E}^2_\mathrm{r} - D_\mathrm{L}\hat{E}^2_\mathrm{z} \end{pmatrix} \tag{2.34}$$

for the diffusion tensor with respect to the axes r and z. With this, Equation 2.32 becomes

$$\begin{aligned} \frac{\partial n_\mathrm{e}}{\partial t} = \nu_\mathrm{i} n_\mathrm{e} + \left(\frac{1}{r}\frac{\partial}{\partial r}(r D_\mathrm{L}\hat{E}^2_\mathrm{r} + r D_\mathrm{T}\hat{E}^2_\mathrm{z}) - \frac{\partial}{\partial z}[\hat{E}_\mathrm{r}\hat{E}_\mathrm{z}(D_\mathrm{T} - D_\mathrm{L})] \right) \frac{\partial n_\mathrm{e}}{\partial r} + \\ + \left(\frac{1}{r}\frac{\partial}{\partial r}[r\hat{E}_\mathrm{r}\hat{E}_\mathrm{z}(D_\mathrm{T} - D_\mathrm{L})] + \frac{\partial}{\partial z}[D_\mathrm{T}\hat{E}^2_\mathrm{r} + D_\mathrm{L}\hat{E}^2_\mathrm{z}] \right) \frac{\partial n_\mathrm{e}}{\partial z} - \mathbf{V}_\mathrm{e} \cdot \nabla n_\mathrm{e} \cos(\omega t). \end{aligned} \tag{2.35}$$

In the case of a parallel plate electrode with an axial, homogeneous electric field $\mathbf{E} = E_\mathrm{z}$, we have $\hat{E}_\mathrm{r} = 0$, $\hat{E}_\mathrm{z} = 1$, and consequently constant diffusion coefficients $\frac{\partial}{\partial r,z} D_{T,L} = 0$, and Equation 2.35 reduces to

$$\frac{\partial n_\mathrm{e}}{\partial t} = \nu_\mathrm{i} n_\mathrm{e} + D_\mathrm{T}\frac{1}{r}\frac{\partial}{\partial r}\left(r\frac{\partial n_\mathrm{e}}{\partial r} \right) + D_\mathrm{L}\frac{\partial^2 n_\mathrm{e}}{\partial z^2} - \mathbf{V}_\mathrm{e} \cdot \nabla n_\mathrm{e} \cos(\omega t), \tag{2.36}$$

as used by Lisovskiy et al. [21] and Sato and Shoji [25]. For homogeneous diffusion $D_\mathrm{T} = D_\mathrm{L}$, equation 2.36 reverts to Kihara's drift-diffusion equation 2.12.

2.3 RF Breakdown Curve

To close this chapter, we will have a closer look at the RF breakdown curve, its features and the physical mechanisms behind them.

If we fix gas type, frequency and geometry (i.e. the plate radius and the gap width) in a parallel plate setup, we are left with only two parameters: gas pressure p and the voltage V applied between the parallel plates. By varying both, the parameter space can be divided into two regions as shown in figure 2.5, one in which a plasma will be formed (hatched) and one in which it will not (outside the solid line). The line which separates the two regions is

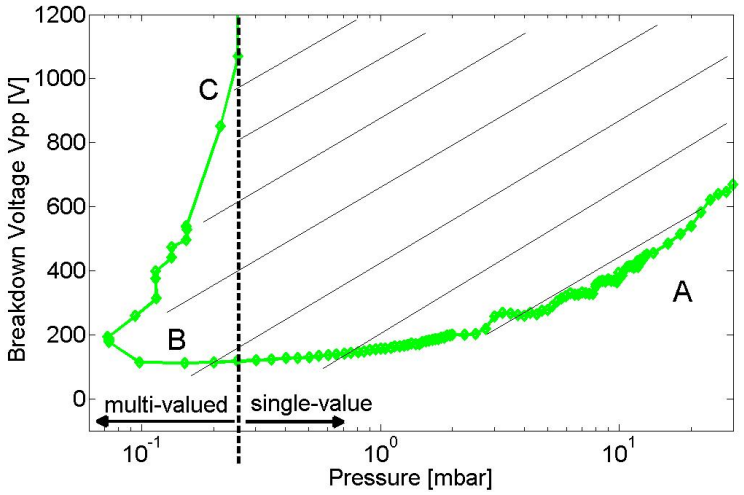

Figure 2.5: Example of a breakdown curve. 12 mm gap-width, argon, 40.68 MHz.

called a *breakdown curve*. Note that this separation does not necessarily hold if moving out from the plasma region in the parameter space (p, V); once established a plasma will generally extinguish at lower voltages/pressures than where it formed.

For breakdown, i.e. the development of a space-charge and the eventual formation of sheaths, some kind of ionisation will have to take place. In the high-frequency field typically applied in industrial plasma deposition reactors (multiples of 13.56 MHz), the only mechanisms for ionisation are ionising collisions between electrons and neutrals, metastables, ions or walls. The oscillation amplitudes of incident ions are much too small to gather enough energy for ionising collisions.

Let us first investigate the high-pressure branch on the right-hand side, denoted by 'A' on figure 2.5. The electron oscillation amplitude A_e is similar to the oscillation of charged particles in vacuum, see equation 2.6, except that now we have to take into account the loss of energy due to elastic collisions with neutrals. The net energy force per unit volume on electrons f_e is then

$$m_\mathrm{e}\frac{\partial u}{\partial t}n = f_\mathrm{e} = (-eE - m_\mathrm{e}u\nu_\mathrm{el})n, \tag{2.37}$$

with n the neutral density, $E = E_0 e^{i\omega t}$ the RF electric field, u the electron velocity and ν_el the electron-neutral collision frequency. This differential equation can be solved with the Ansatz $u = Ce^{i\omega t}$:

$$u = -\frac{e}{m_\mathrm{e}} \frac{E_0}{i\omega + \nu_\mathrm{el}} e^{i\omega t} \tag{2.38}$$

and, integrating,

$$s = -\frac{ieE_0}{m_\mathrm{e}\omega(i\omega + \nu_\mathrm{el})} e^{i\omega t}. \tag{2.39}$$

The maximum of 2.39 provides the electron oscillation amplitude A_e:

$$A_\mathrm{e} = \frac{eE_0}{m_e\omega\sqrt{\nu_\mathrm{en}^2 + \omega^2}} \approx \frac{eE_0}{m_e\nu_\mathrm{en}\omega} \tag{2.40}$$

for $\nu_\mathrm{en} \gg \omega$.

A_e is generally small when compared to the gap-width. For example, at point A in figure 2.5 the electric field is $E_{rf} = V_{pp}/2d = 400/2 * 12 \times 10^{-3} \approx 16700$ V/m. With the elementary charge $e = 1.6 \times 10^{-19}C$, the electron mass $\mathrm{m_e} = 9.1 \times 10^{-31}kg$, the electron-neutral collision frequency (not to be confused with the ionisation frequency ν_i) $\nu_\mathrm{en} \approx 5$ GHz (from [8]) and the angular frequency $\omega = 2\pi f = 2.6 \times 10^8$rad/s the electron oscillation amplitude A_e is approximately 200 μm. Electrons can therefore gain energy in the RF electric field, and the electron loss to the walls will be dominated by diffusion, not convection due to the RF field. For breakdown to happen, the number of electrons generated via ionising collisions must exceed those diffusion losses. Decreasing the pressure (i.e. moving left in figure 2.5) will decrease the electron-neutral collision frequency, which in turn will increase the oscillation amplitude. A larger amplitude means a higher electron energy (since the average kinetic energy of an electron $\varepsilon_\mathrm{e} = \frac{m_\mathrm{e}A_\mathrm{e}^2\omega^2}{2}$), so ionisation events will increase and the breakdown voltage drops. It is important to note that since the electron energy loss due to collisions is a stochastic process, the expression for the electron energy represents the average over the electron energy distribution, and therefore the low value of 7 meV for the example given above does not mean no ionisation takes place.

As we near the minimum breakdown voltage (designated by 'B' on figure 2.5), the electron oscillation amplitude increases. At the minimum, the convective loss of electrons to the walls becomes bigger than the increased ionisation rate and the breakdown voltage rises again. This is also when surface effects such as secondary electron emission start to contribute to the source of ionisation. At the turning point, when the oscillation amplitude reaches half the inter-electrode gap width [21] the breakdown curve starts to double back on itself, resulting in a multi-valued breakdown voltage for this range of pressure. Contrary to the behaviour described above, which is similar if occurring at different pressures and voltages to the behaviour of a

DC breakdown, this is a trait that is unique to RF breakdown, due to its periodic nature. Most of the electrons are now lost to the walls every half-cycle, and an increase of pressure is needed for breakdown to occur. The left-hand branch (denoted by 'C' in figure 2.5) rises steeply, inclined to the right. The higher the voltage, the larger the electron oscillation amplitude and the shorter the time available for ionisations each half-cycle. Only at very high voltages (>2 kV in this case) will the breakdown curve bend back to lower pressures again.

Chapter 3

Experimental Setup

This chapter provides a description of the experimental setup used in the experiments of this thesis. Since the main focus was on discovering why arcing happens in PECVD reactors, and arcing is a local phenomenon, a decision was taken early on to use a small vacuum chamber instead of an industrial PECVD reactor. The ease of access, modification and fast pump-down times allowed for a great number of experiments to be done in short time, which would not have been possible with an industrial reactor. Furthermore, any eventual damage to a full-sized large area PECVD reactor would have been both costly and difficult to repair. A smaller-sized experiment can thus serve as a test-bed to investigate RF breakdown in critical large-area reactor components.

Figure 3.1 shows a simplified view of the experimental setup. The vacuum chamber chosen (see figure 3.2) is cubic with a side of 33.5 cm, and DN 160 ISO-K access ports on all sides. Smaller ports on top allow access for pressure gauges.

The vacuum chamber contains two cylindrical electrodes of 130 mm diameter (see figure 3.3 for a more detailed view); the left connected to ground, while the right electrode is connected to the RF generator (Dressler WLPG) via a modified Advanced Energy RF navigator matchbox. The RF electrode features an exchangeable electrode plate, shown in light grey in figure 3.1. To ensure an even gap between RF and ground electrode, the electrodes are separated by 20 mm wide Perspex rings, with an inner diameter of 90 mm. The discharge takes place in the gap between the two electrodes, whose width was set by the Perspex ring thickness. A metal ground shield, connected to electrical ground, surrounds the electrodes to prevent spurious premature breakdown at the electrode edges. Both electrodes are water-cooled, to prevent any problems at the high RF power-densities used in the experiments, due to ohmic heating from skin-currents associated with high RF voltages in

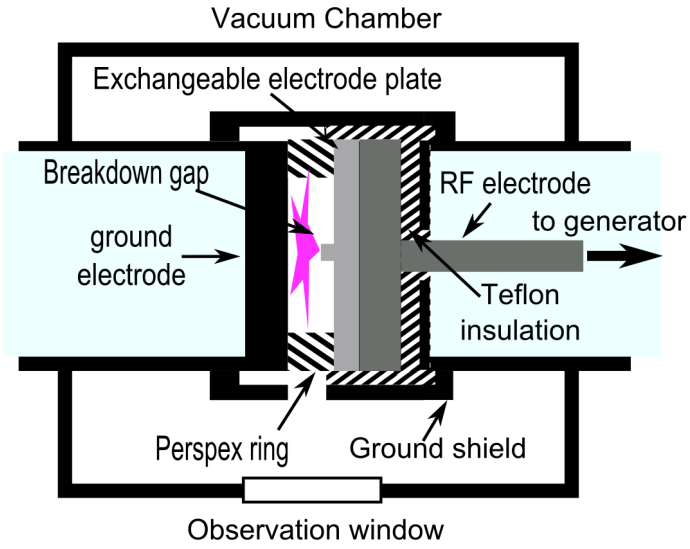

Figure 3.1: Experimental setup. The ground shield is a closed cylinder with a small aperture opposite the observation window. The perspex ring thickness determines the parallel-plate gap width. All electrode surfaces are aluminium unless otherwise noted, to replicate conditions found in industrial reactors. See text for dimensions.

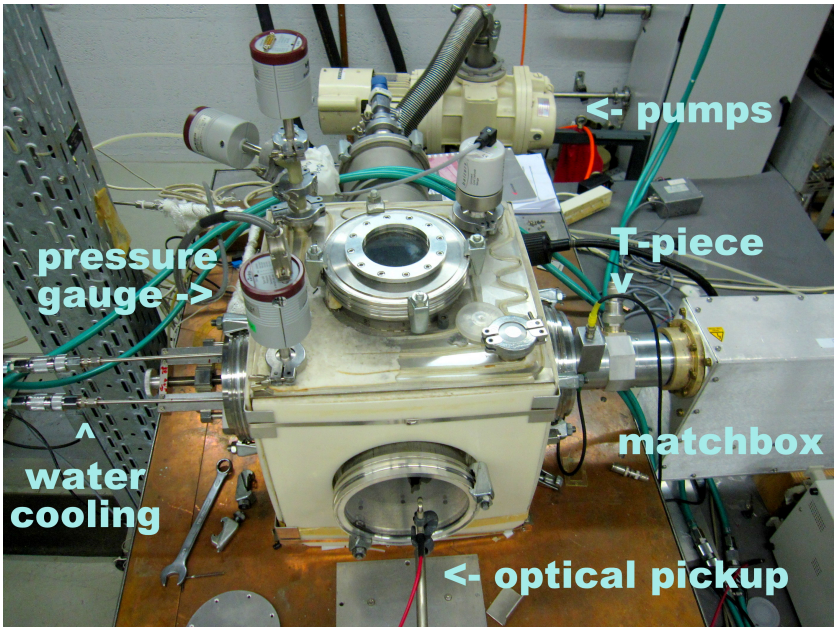

Figure 3.2: A photo of the vacuum vessel, with pumps, pressure gauges and matchbox visible.

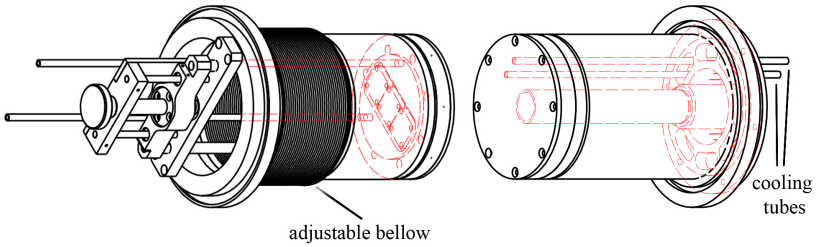

Figure 3.3: The watercooled ground and RF electrodes. The exchangeable electrode plates in figure 3.4 were screwed onto the RF electrode.

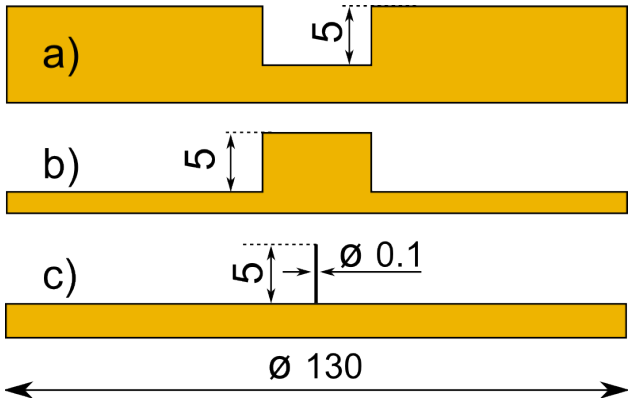

Figure 3.4: Exchangeable electrodes: a) hole electrode, b) cylindrical electrode, c) electrode with protruding wire.

low impedance systems.

3.1 Working Gases and Pumping

The base pressure of the vacuum chamber was 0.035 mbar using a primary and a Roots pump. The working gas was injected into and removed from the vacuum chamber via Tylan FC2900 and Bronkhorst F-201C flowmeters with a maximum flow of 200 sscm outside the discharge gap. The gas pressure was controlled by a MKS butterfly valve, and monitored via MKS capacitance manometers (2 mTorr, 10 mTorr and 1000 mBar ranges), likewise located outside the discharge gap. Measurements were taken between 0.1 and 30 mbar. The capacitance manometers were calibrated as follows: A small chamber with a volume V_1=14.5 cm^3 was filled with air at ambient pressure p_a (reading taken from the local weather station). A valve was then opened, connecting to a larger chamber (pumped down to base pressure) with a vol-

ume V_2=1244 cm^3. The connecting valve and the capacitance manometer together represented a volume V_3=6.3 cm^3. The resulting pressure in the combined volumes was then expected to be

$$p = p_{\mathrm{a}} \frac{V_1}{V_1 + V_2 + V_3}, \tag{3.1}$$

which the 10 Torr capacitance manometer measured to within 2%. The same procedure was repeated with two more, differently sized volumes V_2, with the same result. The calibrated manometer was then used to confirm the calibration of the two other manometers.

Argon and hydrogen were used as working gases. Argon as a representative for atomic gases, and because its use is widespread in the literature, and hydrogen for its molecular characteristics and as an equivalent to highly depleted silane (SiH_4), which is used in the industry as a working gas for the deposition of silicon. Measurements were taken in the range of 0.1 to 30 mbar. The measurement error for pressure was below 5%.

3.2 Electrical Characteristics

The variable frequency RF generator (Dressler WLPG) used can supply up to 500 W RF power at frequencies from 1 to 100 MHz. Since its signal was not purely sinusoïdal, but highly distorted with strong harmonics, notch filters for 13.56, 27.12 and 40.68 MHZ were used between generator and matching network to ensure a power supply relatively free of harmonics. All measurements in this thesis, except if otherwise noted, were made at 40.68 MHz. 13.56 MHz and its harmonics are industry standards, since they form part of the ISM radio bands kept reserved for industrial, scientific and medical purposes other than communications.

The breakdown voltage could not be directly controlled, as the RF generator used only allows for control of the RF power. The maximum voltage slew rate was 50 V_{pp}/ms.

Measuring the RF voltage at the electrode accurately can present surprising difficulties [26]. At 40.68 MHz the wavelength is 7.1 metres, and the connection between RF electrode and matchbox is short ($\tilde{6}$0 cm), so one might assume that it is possible to measure the voltage outside the vacuum chamber, via a T-shaped connector (subsequently called T-piece for brevity) between matchbox and reactor. This means the measuring point is only about 30 cm from the electrode, or less than a twentieth of the RF wavelength. However, the measured voltage at the T-piece (to the left of the matchbox in figure 3.2) was up to a factor of 5.4 smaller than the actual

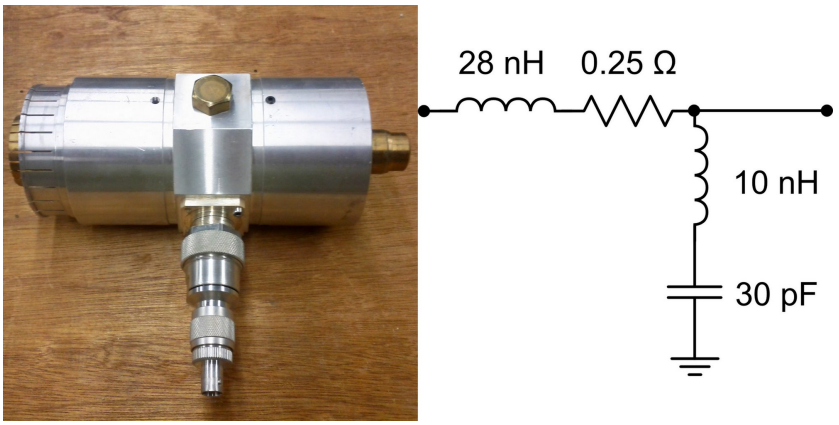

Figure 3.5: Photo (left) and equivalent circuit (right) of the T-connector. The reactor would be connected to the left, the matchbox to the right. A voltage probe would be connected to the BNC-connector at the bottom.

voltage at the RF electrode. To understand this behaviour, a careful analysis of the electrical system is necessary.

The electrical characteristics of the reactor were measured via a Rohde & Schwarz Vector Network Analyser. In order to understand the reactor's behaviour, five different impedance measurements were made: The T-piece between matchbox and reactor, the RF electrode outside the vacuum chamber, the RF electrode installed in the vacuum chamber, RF and ground electrode separated by a 1 mm gap and finally RF and ground electrode separated by a 1 mm gap with the ground shield in place.

The T-piece was measured both open and shorted out at the reactor side. Its equivalent circuit diagram is shown in figure 3.5, and figure 3.6 shows a comparison between the open circuit measurement and the equivalent circuit model.

Figures 3.7 and 3.8 show the equivalent circuit and measurement of the open circuit RF electrode, outside of the vacuum chamber, without the ground electrode present. The electrode can be modelled as a simple LC series circuit, with a capacitance of 50 pF and an inductance of 5 nH. The same capacitance was obtained by using the geometry of the electrode in a finite element solver. Calculating the inductance analytically, by modelling the electrode as a short coaxial cable with a parallel plate capacitor where the RF plate is isolated from the ground via Teflon gives a capacitance of 40 pF.

Installing the RF electrode into the vacuum chamber, with a 1 mm gap between it and the ground electrode (see figure 3.3) results in the situation shown in figures 3.9 and 3.10. The large 160 pF capacitance to the left of

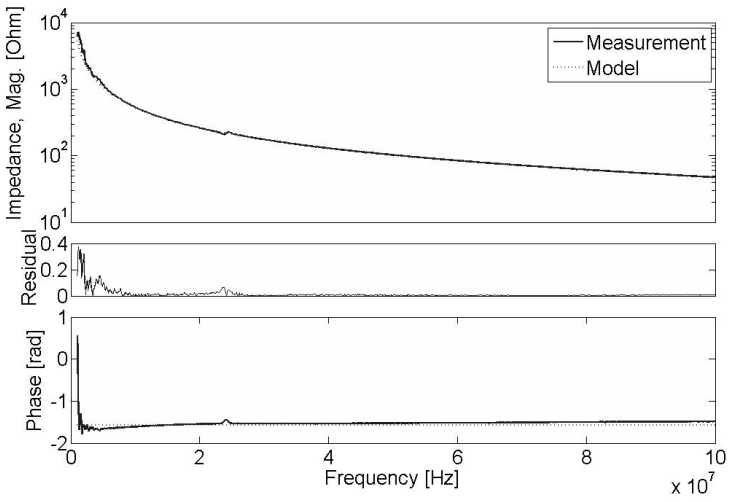

Figure 3.6: Open circuit measurement of the connecting T-piece.

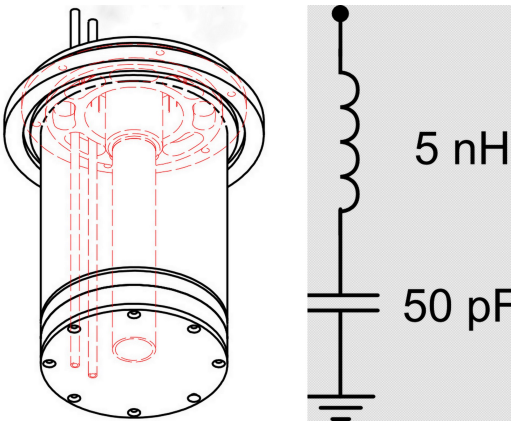

Figure 3.7: RF electrode (left) and equivalent circuit of the RF electrode outside the vacuum chamber (right).

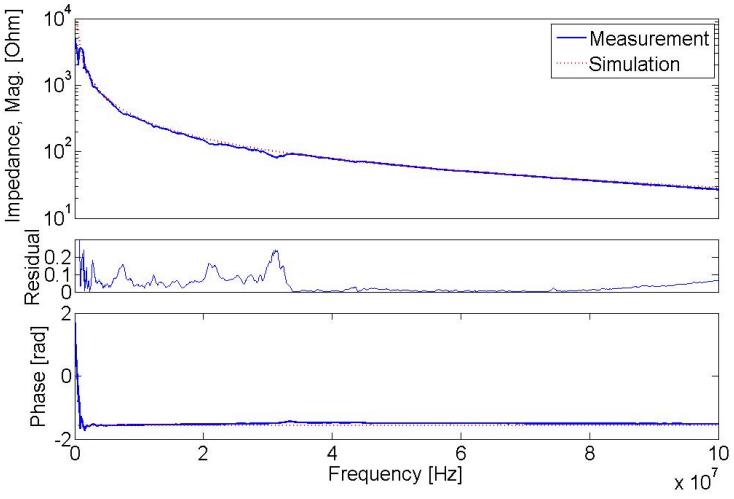

Figure 3.8: Open circuit measurement of the RF electrode.

figure 3.9 can be interpreted as the capacitance of both the gap (60 pF) and the internal capacitance of the RF electrode (50 pF). The 84 nH inductance represents the return current loop which traverses the reactor walls back to the RF electrode (see also 3.16). The series resonance of this circuit lies near $f_{\text{res}} = \frac{1}{2\pi\sqrt{LC}} \approx 38.4$ MHz, with L=84 nH and C=204 pF (see figure 3.10). The resonance is physically due to the inductance of the volume enclosed by the circuitry, and the capacitance of the electrodes.

Attaching a ground screen (see figure 3.1) increases the capacitance to ground to 250 pF, since it brings more of the RF electrode in close contact to grounded metal parts. At the same time, the current loop is made much smaller, cutting the inductance in half to 42.3 nH. It is an unfortunate coincidence that the ground screen reduces the inductivity of the current loop, but at the same time increases the capacitance of the electrode arrangement, so that the new resonant frequency is still close to the operating frequency at 40.68 MHz. Figure 3.11 shows the equivalent circuit diagram, and the impedance is shown in figure 3.12. See also figure 3.16 for a schematic of the different current paths.

If we then attach the T-piece to the reactor we arrive at the situation for a normal parallel plate measurement, with a 1 mm gap, in figures 3.13 and 3.14. A look at the impedance measurement in figure 3.14 shows the reason for the wrong voltage measurements at the T-piece: the resonant frequency of the circuit is very close to the 40.68 MHz normally used in operation. Using the equivalent circuit diagram in figure 3.13, we can calculate the expected voltage multiplication factor, by designating the impedance of the 250 pF

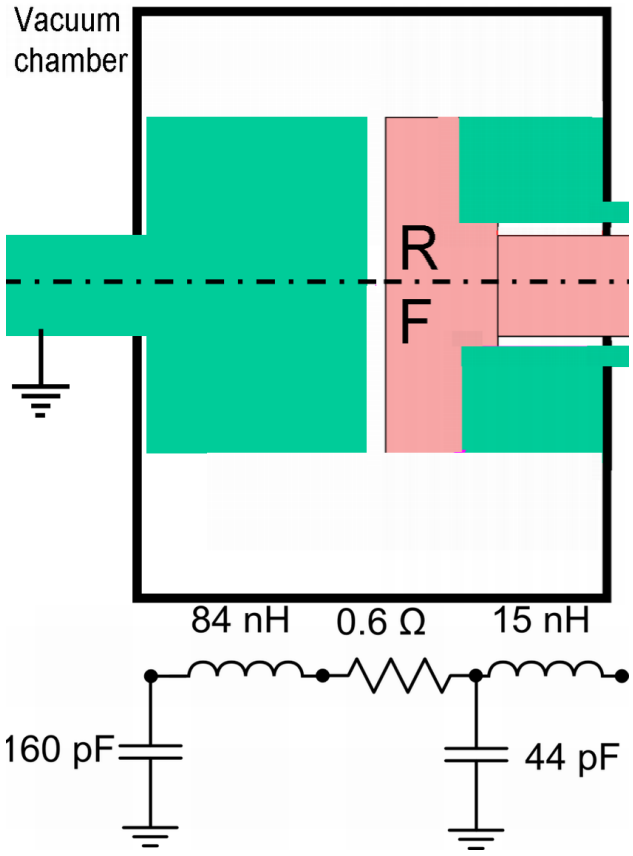

Figure 3.9: Setup without ground screen, with a 1 mm gap between the electrodes (above). RF current bearing parts in pink, labelled "RF". The equivalent circuit diagram is shown below.

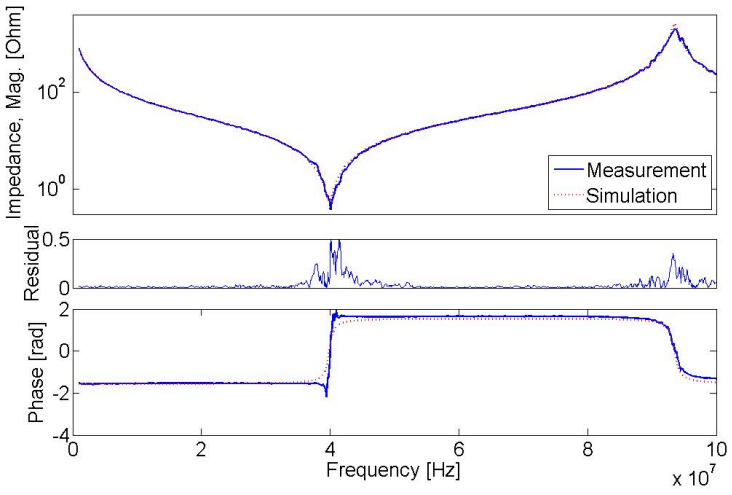

Figure 3.10: Open circuit measurement of a 1 mm gap.

capacitor as Z_C and assuming that it more or less represents the capacitance of the RF electrode to the surrounding structure. The ratio of the voltage U_B at point B to the input voltage U_A at point A is then

$$\frac{U_B}{U_A} = \frac{Z_C}{Z_1}\left(1 - \frac{Z_X}{Z_R}\right). \tag{3.2}$$

The same calculation can be done for the case without a guard screen. Figure 3.15 shows the resulting voltage multiplication factor over frequency. For the working frequency of 40.68 MHz we calculate a multiplication factor of 6.9 with, and 10.4 without a guard screen. These values are close to the measured values (see section 3.3 for a discussion of the voltage probes used) of 5.4 and 10, respectively.

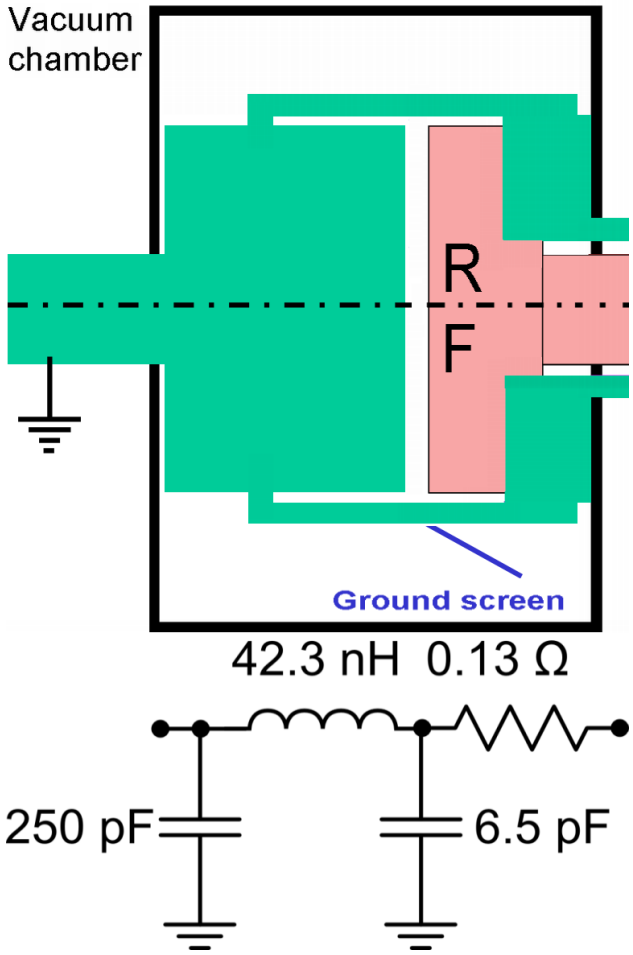

Figure 3.11: Setup with ground screen (above). RF current bearing parts in pink, labelled "RF". Equivalent circuit diagram below.

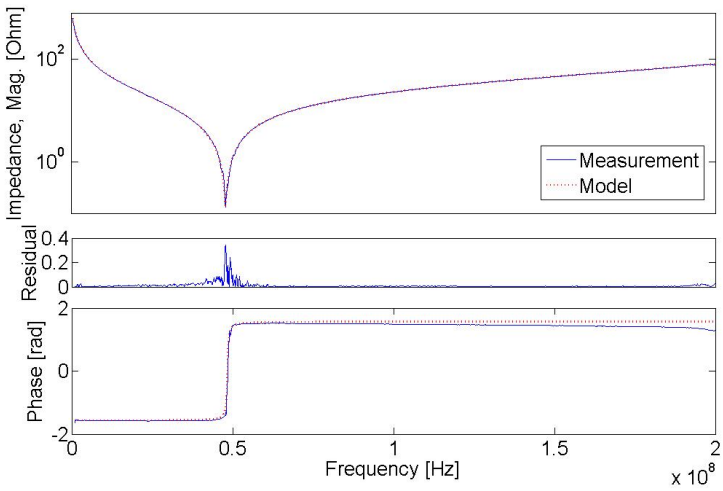

Figure 3.12: Impedance measurement of a 1 mm gap, with attached ground screen

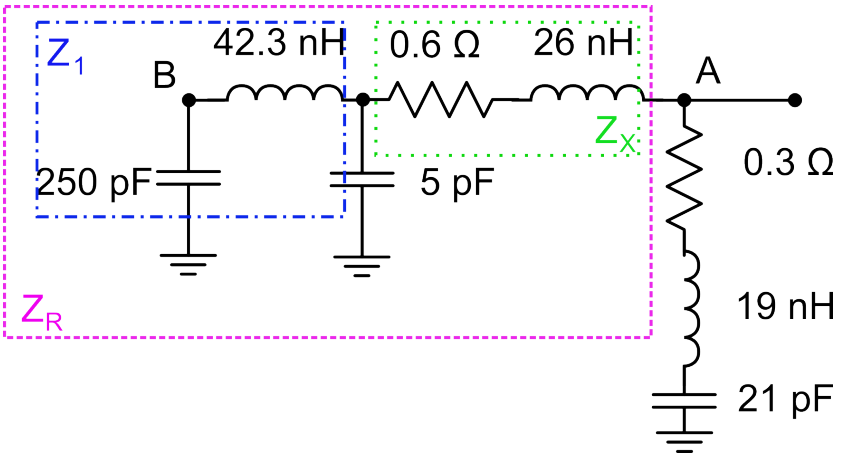

Figure 3.13: Equivalent circuit diagram of the 1 mm gap, with an attached ground screen and T-piece. This is the complete experimental setup, as used throughout the present work. "A" is where exterior voltage measurements were attached, "B" corresponds more or less to the surface of the RF electrode.

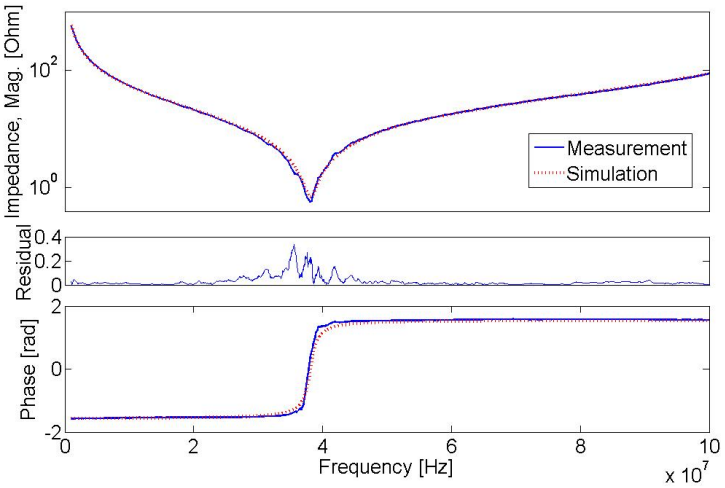

Figure 3.14: Impedance measurement of a 1 mm gap, with attached ground screen and T-piece, i.e. the complete experimental setup.

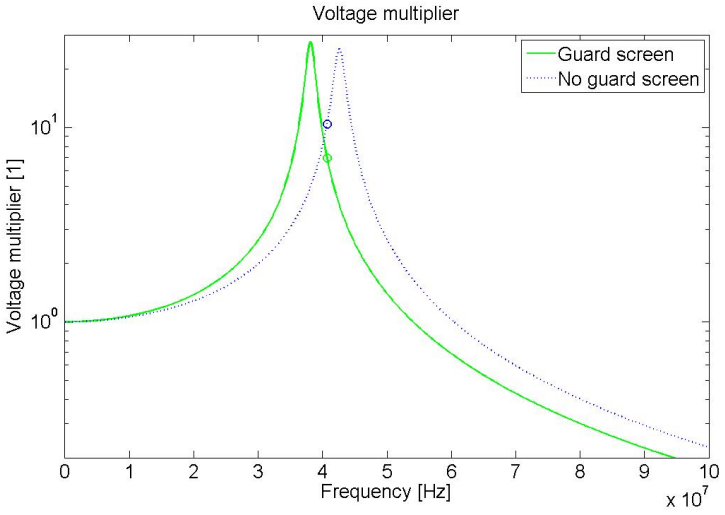

Figure 3.15: Voltage multiplier with (solid line) and without (dotted line) grounded guard screen. The circles show the voltage multiplication factor at 40.68 MHz: 6.9 and 10.4, respectively.

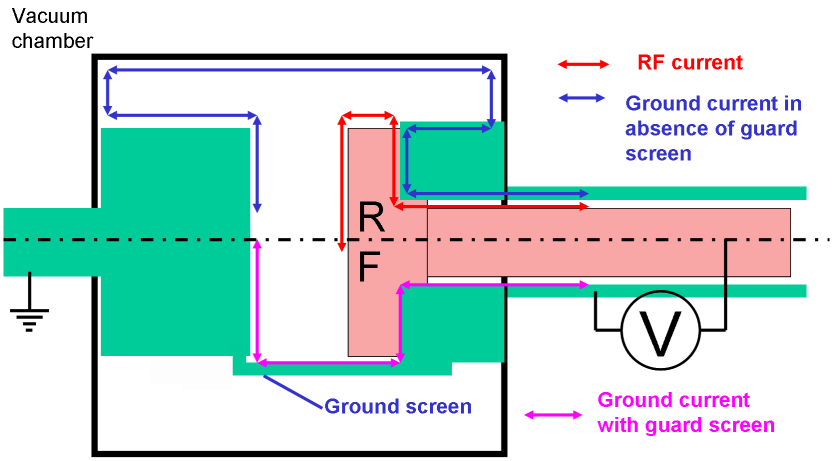

Figure 3.16: Current path with (lower half) and without (upper half) guard screen.

3.3 Voltage Measurement

In almost all the experiments done in the present work we were interested in the breakdown voltage, i.e. the voltage was measured before the plasma formed. This made voltage measurements easier, since the change of impedance a discharge plasma brings about did not have to be taken into account.

With the voltage multiplication on the RF electrode (as described in the previous section), measuring the RF voltage at the T-piece was not practical, since each change of the geometry between the electrodes (gap-width, surface structure) changed the impedance and hence the multiplication factor significantly. Changes in frequency had an even greater effect. Fortunately, the experimental setup allowed direct access to the electrode backplate (see figures 3.1 and 3.3), and measuring the voltage directly at the electrode was possible. Since the RF peak-to-peak voltages (V_{pp}) in the experiments reached 3000 V_{pp} and the space inside the electrode was limited, and to prevent excessive RF currents in the probe, a capacitively coupled two-stage probe was used (see figure 3.17). The first stage was implemented by using short lengths of coaxial cable as capacitances. It reduces the voltage by a factor of about twenty, enough to prevent arcing between the probe components. The second stage consisted of a 10 pF high-voltage metal film capacitor. The coaxial cable connecting the probe to the oscilloscope served as the 50 pF capacitance to ground, thereby completing the 1:151 voltage probe.

Measuring the RF voltage with a LeCroy 1/1000 probe directly applied to the side of the RF electrode with a vacuum chamber open to the atmo-

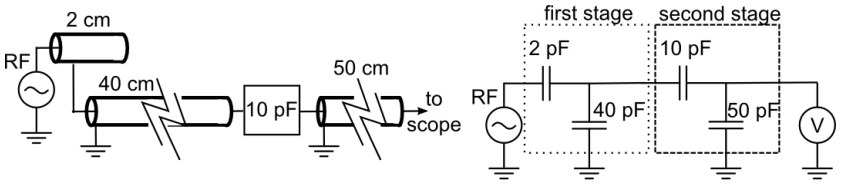

Figure 3.17: 2-stage voltage probe (left) and circuit diagram (right). The 2 and 40 pF capacitances of the first stage were implemented via short pieces of coaxial cable, 2 and 40 cm in length, respectively. The 50 pF capacitance of the second stage was the 50 cm long coaxial cable connecting the probe to the oscilloscope.

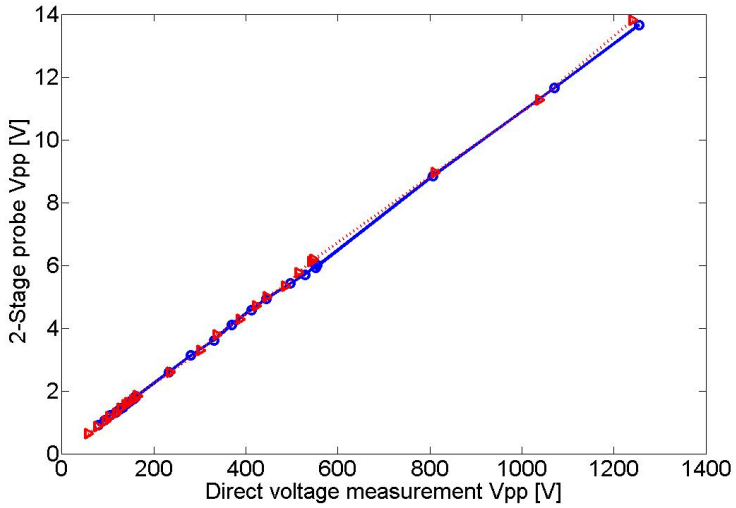

Figure 3.18: Voltage linearity of the 2-stage voltage probe, for parallel plate electrodes with gap-widths of 2 (circles) and 12 mm (triangles), at 40.68 MHz

sphere showed that the two-stage probe division factor was actually about 1:90 for 40.68 MHz, and 1:150 for 27.12 MHz, most probably due to stray capacitances and inductances introduced in the construction. The division factor was mostly independent of the discharge gap geometry (see figure 3.18, showing the probe voltage linearity at constant frequency), but was nevertheless measured each time the geometry was changed, to ensure the most accurate measurement possible.

The first breakdown of the day had a breakdown voltage up to 20% higher than the subsequent measurements. This phenomenon, called a memory effect [27, 28] is probably due to surface contamination (water, oil, etc.) which is removed by the ion impacts and surface heating of the first plasma of the day. This removal is called "conditioning" in this context. Since reproducing the voltage of the first breakdown needed up to tens of minutes between measurements, the first breakdown measurement for each pressure point was discarded, as the prinicpal aim of the investigation in the course of this thesis was not a precise determination of RF breakdown voltage, but rather the influence of non-planar geometries on the same. In any case, the conditioned, reproducible voltage is the relevant measurement which can be influenced by changing the geometry of the electrode, although it is true that damage in a real reactor may happen with the first arc.

3.4 Matching

Power transfer between generator and reactor is only efficient if the impedances match. If they do not, part of the RF power generated by the reactor will be reflected, with the reflection coefficient Γ:

$$\Gamma = \frac{Z_R - Z_G}{Z_R + Z_G}, \tag{3.3}$$

with Z_R and Z_G the impedances of the reactor and the generator, respectively. To avoid this, it is necessary to use an RF matching network or matchbox to bring the impedance of reactor plus matching network to match the 50 Ω output impedance of the generator. There are various types of matching networks available - in this case a high-pass "T" matching network was used (see figure 3.19) [29]. The network, a modified Advanced Energy matchbox, consisted of a water-cooled 128 pH inductance, a Comet 50-500 pF variable vacuum capacitor at the source side and a Comet 5-170 pF variable vacuum capacitor at the load side. The matchbox was equipped with servo motors, and was controlled via a PC. Although capable of auto-

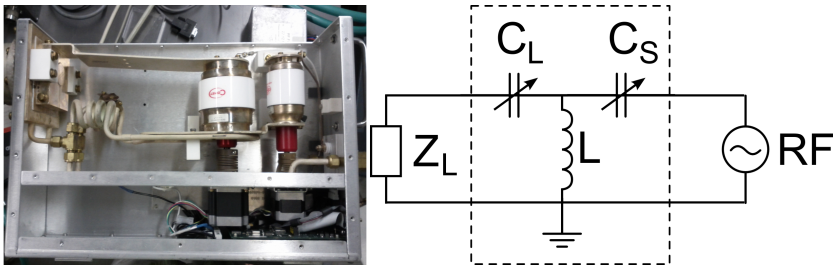

Figure 3.19: Left: Interior of an Advanced Energy matching network. The Comet vacuum capacitors with their stepper motors are to the right, the water-cooled inductance can be seen to the left. Right: Equivalent circuit diagram, T-matching network. The network is inside the dashed box. Z_L represents the impedance of the load.

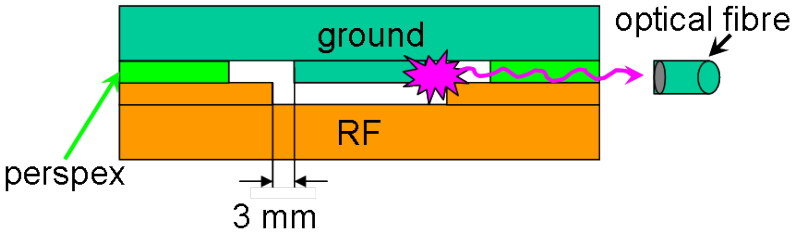

Figure 3.20: Optical emission spectrography and breakdown detection, setup.

matic matching, all experiments done in this work were matched manually, to ensure reproducibility.

Finding the matchpoint was very difficult, due to the high quality factor Q (no power dissipation) of the reactor. Considered in the simplest case as an RLC network with $R \approx 0.2\ \Omega$, $L \approx 100$ nH and $C \approx 300$ pF, the quality factor amounts to

$$Q = \frac{1}{R}\sqrt{\frac{L}{C}} \approx 91 \tag{3.4}$$

which means that the matching network has to be tuned very finely.

3.5 Breakdown Detection and Optical Emission Spectroscopy

Light from the breakdown was monitored via an optical fibre situated outside of the vacuum chamber (see figure 3.20). This allowed for some basic

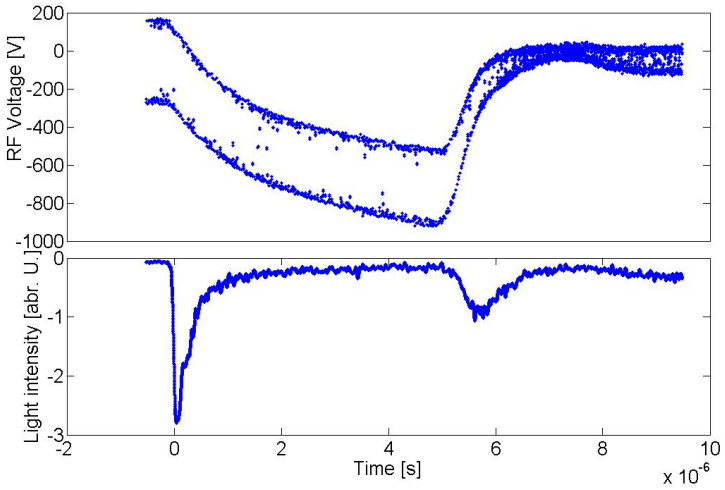

Figure 3.21: Argon, breakdown in a cylinder-in-hole geometry, 0.6 mbar. RF voltage envelope (top) and optical fibre pick-up (bottom, inverse scale). The breakdown event is visible at $t = 0$ s. The following, unusual shape of the voltage envelope is probably due to a combination of expanding plasma in the complex geometry and circuit response.

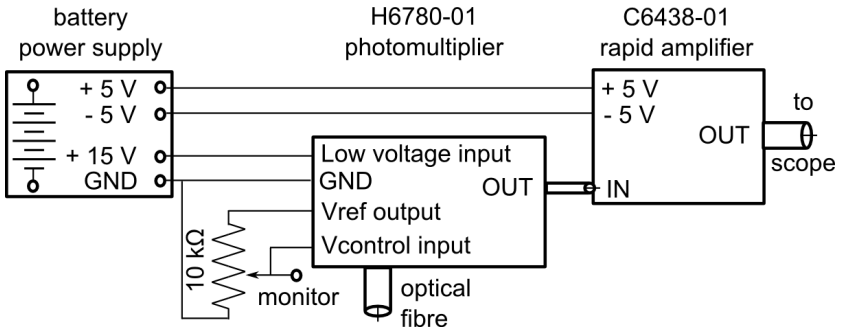

Figure 3.22: Circuit diagram of the light detection circuit.

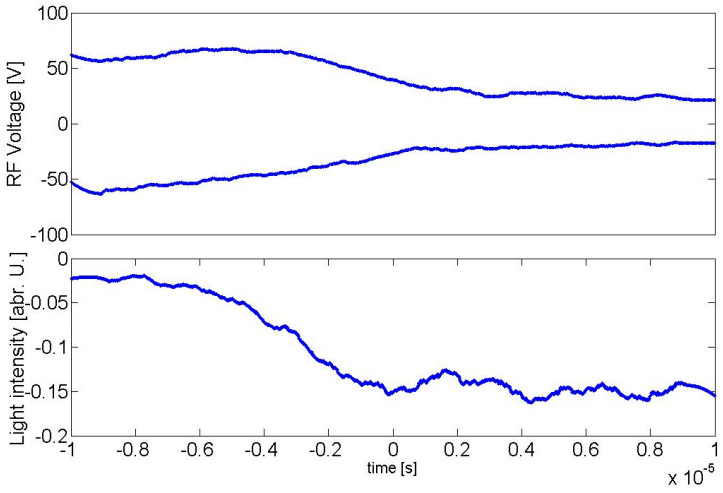

Figure 3.23: Argon, breakdown in a cylinder-in-hole geometry, 0.9 mbar. RF voltage envelope (top) and optical fibre pickup (bottom, inverse scale). The breakdown event is visible at around $t = -60$ μs.

optical emission spectroscopy for hollow cathodes (see chapter 6) and for breakdown detection. Figure 3.21 shows the RF envelope (top) and optical fibre pick-up (bottom) of a breakdown in argon, at 0.6 mbar, in a cylinder-in-hole geometry. The emitted light was detected via a Hamamatsu H6780-01 photomultiplier (spectral range: 300 - 850 nm) whose gain could be controlled by a 10 kΩ potentiometer. The signal was then further amplified by a Hamamatsu C6438-01 rapid amplifier (see circuit diagram in figure 3.22), and then used as a trigger for the oscilloscope, since the sharp peak right at breakdown gives a much better detection method than the voltage envelope: While there is always some reduction in peak-to-peak voltage during breakdown, this reduction can be small and difficult to detect (see figure 3.23). The reliability of breakdown detection using light is significantly higher.

The same setup was also used for some basic optical emission spectroscopy. Spectra were taken using the Ocean USB2000 spectrometer, which only has a resolution of 0.5 nm. Figure 3.24 shows an argon spectrum taken at low RF power (10 W) at 1 mbar. While all major Ar I lines can be identified, the inaccuracies of the spectrometer made identifying all lines in experiments with more complex plasma difficult, especially in the case of degrading Teflon (see chapter 6). Figure 3.25 shows a plot of the difference between reported values of the major Ar I lines (from [30]) and the observed wavelengths from figure 3.24.

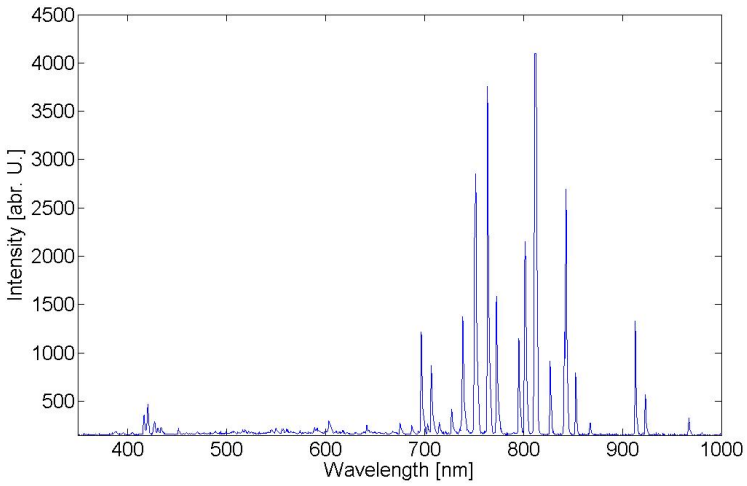

Figure 3.24: Argon spectrum

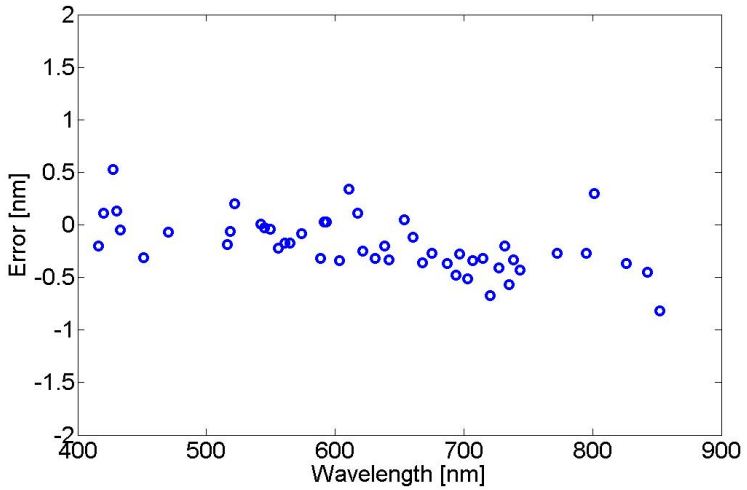

Figure 3.25: Spectrometer error for the major Ar I lines.

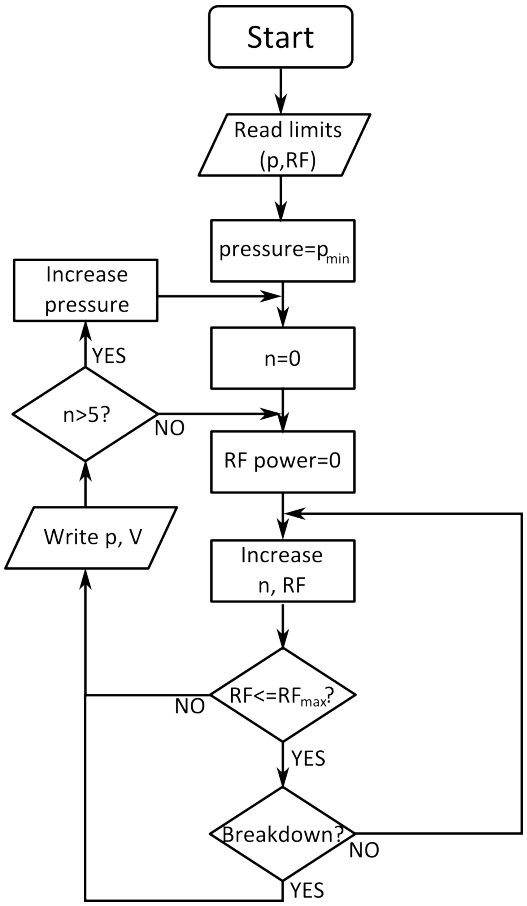

Figure 3.26: Flowchart for automated measurement, RF loop.

3.6 Automation

Since measuring accurate breakdown curves was a major part of the experimental work for this thesis, the measurement was automated, both to ensure similar conditions for all breakdown measurements by removing a human operator, and to speed up the measurement.

The measurements were controlled by a PC running the program LabView, which interfaced with the oscilloscope via GPIB, and with the RF generator and the pressure control via the RS 232 serial interface. Two different programs were used: For the right-hand branch of the breakdown curve up to the turning point (see chapter 4) the pressure was held fixed, while the RF power was gradually increased in deca-logarithmic steps (see flowchart in figure 3.26). After each power-step, the program queried the oscilloscope to see if a breakdown had taken place (i.e. if the oscilloscope

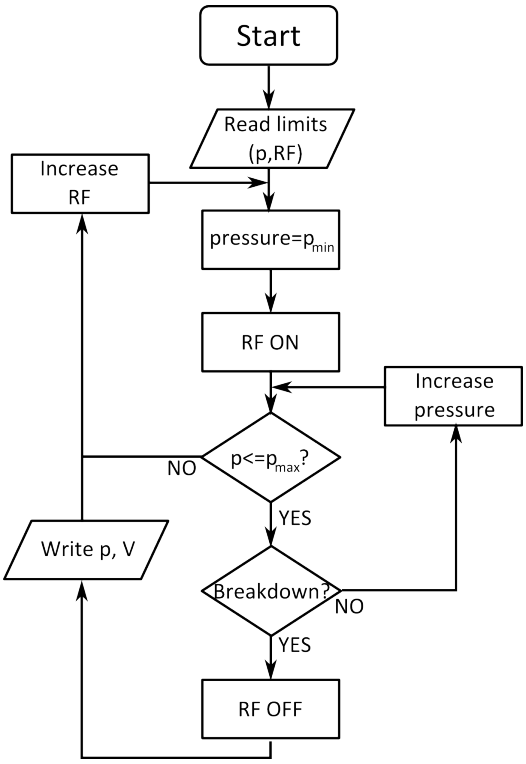

Figure 3.27: Flowchart for automated measurement, pressure loop.

had triggered, the trigger was set to the channel measuring the signal from the photo-multiplier). If so, pressure and voltage were recorded. This was repeated five times for a total of six measurements, after which the pressure was increased for the next set of measurements.

The steep branch on the left-hand side of the breakdown-curve was measured by the method proposed by Levitskii [31] (see figure 3.27): The pressure was set to a low value outside of the anticipated breakdown curve. The RF power was held fixed, while pressure was slowly increased until breakdown occurred. Pressure and voltage were again recorded, and the RF voltage increased to the next level. Since the pressure loop runs much slower than the RF loop, only one measurement was run per data point, after experiments had shown that the values varied in general by less than 10% on subsequent runs of the same loop.

Both RF and pressure loop set a failure flag in case breakdown failed to occur over the available range of pressure or voltage.

Delays were introduced in each loop to ensure pressure equalisation in the chamber of the electrode gap between pressure-steps and breakdowns. Running a pressure loop with ascending and descending pressure (see figure

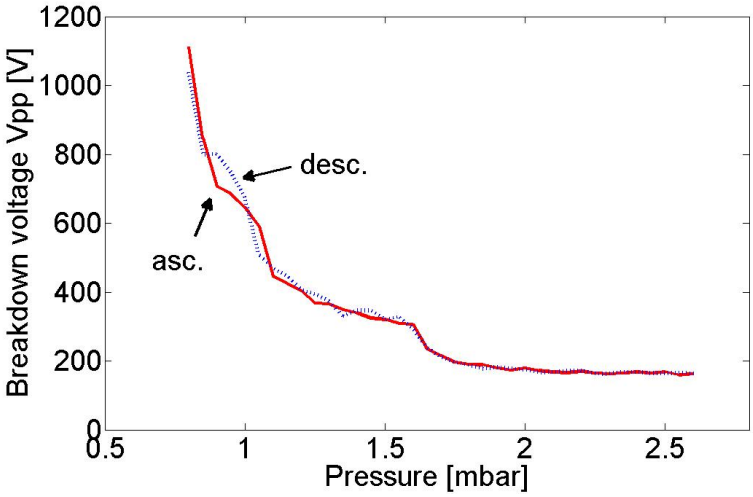

Figure 3.28: Breakdown curves taken with ascending (asc.) and descending (desc.) pressure ramps. The delay between each pressure step (0.1 mbar in this case) and the start of the breakdown measurement was one second in this case, and six seconds for all other measurements.

3.28) proved to be a convenient method to ascertain whether the pressure had equalised after each pressure step, since a direct pressure measurement in the breakdown gap was not possible. If the pressure of the breakdown gap had not reached the pressure of the vacuum chamber, those two curves did not overlap. It proved necessary to cut shallow grooves into the Perspex rings, and to introduce a delay of six seconds after each pressure step to ensure equalisation.

3.7 Hollow Cathodes

The experimental setup for hollow cathodes consisted of the modified RF electrode shown in figure 3.29. Aluminium and Teflon rings with variable widths (1 - 10 mm) were screwed onto the RF electrode as placeholders, and a plate or aluminium foil with a single or multiple holes was added on top. The vacuum vessel served as the ground electrode. A hollow cathode burning at 430 Watts in argon can be seen in figure 3.30. The placeholder ring is made of aluminium in this case, and 4 mm thick. The hollow cathode is burning in a 1.5 mm thick hole-plate.

Another setup used is shown in figure 3.31. A grounded grid plate (see figure 3.32) was attached via 4, 1 cm wide aluminium strips to the grounded

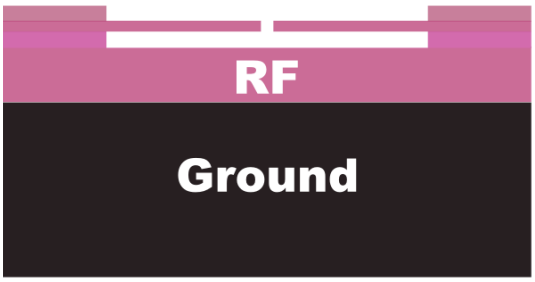

Figure 3.29: Electrode configuration, hollow cathode.

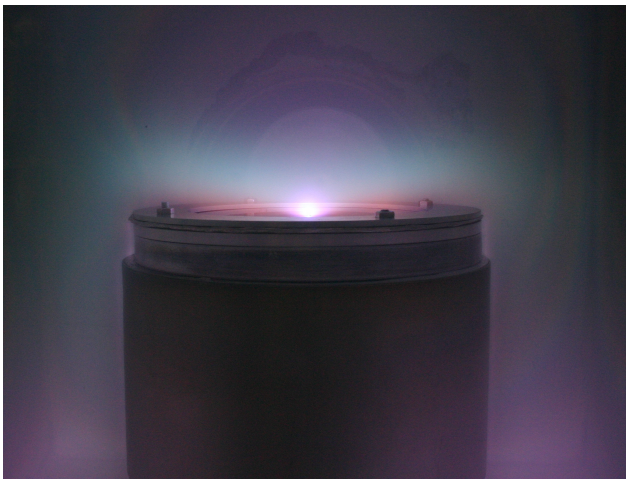

Figure 3.30: Hollow cathode, aluminium electrode, 430 Watts RF power, argon.

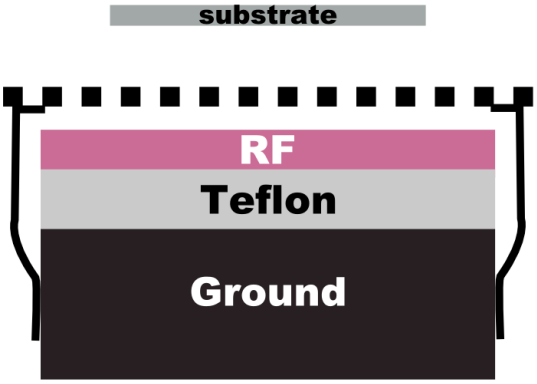

Figure 3.31: Electrode configuration, grounded grid plate.

base of the RF electrode, and suspended over the RF electrode. In this way, the gap between the grounded grid and the RF electrode could be chosen to be anything between 1 and 10 mm. Above the grounded grid plate, a glass substrate could be positioned for deposition experiments (see figure 3.33 for an example of the grid-plate in operation). One of the four strips holding the grounded grid plate in place can be seen in the foreground.

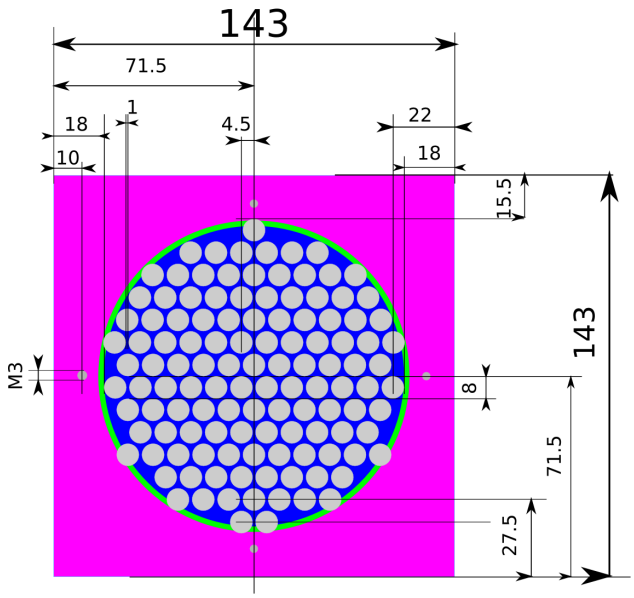

Figure 3.32: Grounded grid plate, 8 mm holes.

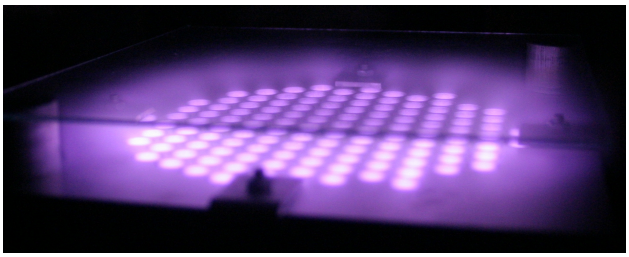

Figure 3.33: Grounded grid plate with glass substrate, argon.

Chapter 4

RF Breakdown Between Parallel Plates

This chapter presents the primary experimental results of the present work. It is split into three parts: First, capacitively coupled RF breakdown in parallel plane geometries is investigated, then, in the second part, more complex structures are examined. Finally, the results are discussed and a way of reducing the breakdown complexity of structured electrodes to multiple overlapping parallel plate breakdown curves is presented at the end of this chapter. As already mentioned (see chapter 3), all measurements presented in this chapter were done at 40.68 MHz, unless otherwise noted.

4.1 Parallel Plate Breakdown

Before investigating breakdown in complicated structures like the showerheads of RF reactors it is important to understand breakdown in its simplest terms: breakdown between parallel plates.

4.1.1 Gap Width and Frequency Dependence

From the description of the breakdown mechanism in chapter 2 we see that gap-width and frequency play a major role in determining the pressure dependence of the breakdown voltage. Figure 4.1 shows the measured breakdown curves for parallel plates with a gap-width of 12 mm (green $\Diamond$), 8 mm (magenta $\triangle$), 6 mm (red $\bigtriangledown$), 4 mm (cyan $\square$) and 2 mm (blue $\bigcirc$). A few features are immediately obvious: increasing the gap-size shifts the breakdown curve to lower pressures. At 6 mm (red $\bigtriangledown$), a multivalued region appears at the point where the flat right-hand side of the curve meets the steep left-hand

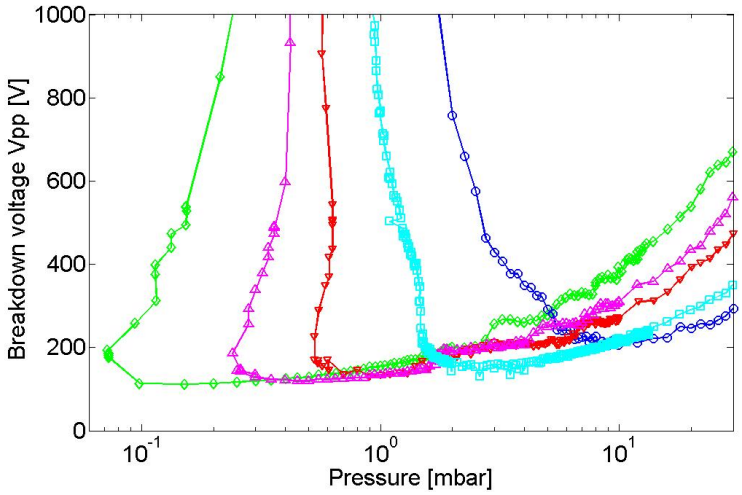

Figure 4.1: Influence of the gap width on the breakdown voltage, argon. 12 mm (green ◊), 8 mm (magenta △), 6 mm (red ▽), 4 mm (cyan □) and 2 mm (blue ◯).

side. This multivalued region is present for all gaps wider than 6 mm, and becomes more pronounced as the gap-size increases.

As mentioned before (see chapter 2), in DC breakdown, the breakdown curves (also called Paschen-curves in this case) usually show a *pd* scaling law [32], i.e. when plotted as breakdown voltage versus the product of pressure times distance, the curves coincide. In the case of the radio-frequency breakdown this only holds true for the high-pressure branch on the right-hand side, as shown in figure 4.2, which shows breakdown curves for the same gap-widths as in figure 4.1, but plotted as voltage versus *pd*. At low pd-values the larger gap-widths extend far to the left, as surface processes such as secondary electron emission start to play a role in breakdown, only rejoining the smaller gap-widths at the top of the multi-valued region, a phenomenon that is not replicated in DC breakdown (see chapter 2). In the region where the curves do not coincide, the breakdown process is a mix between surface processes and volume processes, and the different surface-to volume ratio for different gap-widths is the culprit for the disparity in breakdown voltages. At high voltages or high pressures the curves rejoin, as there the breakdown is dominated solely by surface processes or volume processes, respectively.

Lisovskiy showed a scaling law similar to DC for RF-breakdown [33]. For a constant product of gap-width and frequency the breakdown curves coincide, as shown in figure 4.3.

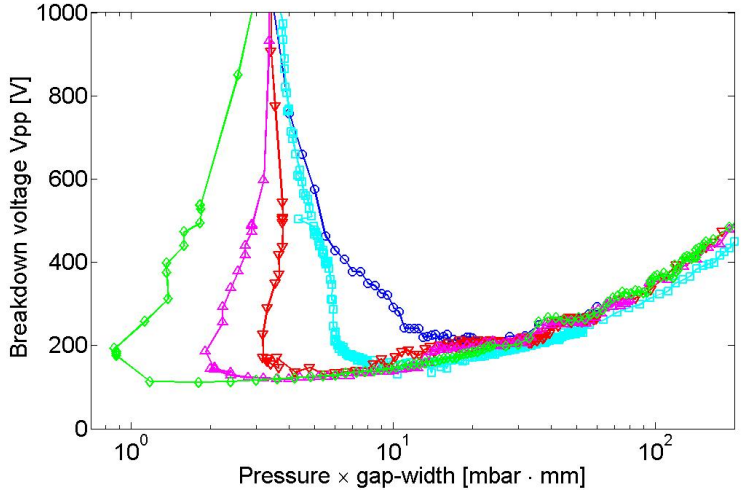

Figure 4.2: Breakdown voltage versus pressure × gap-width in argon, for different gap widths: 12 mm (green ◊), 8 mm (magenta △), 6 mm (red ▽), 4 mm (cyan □) and 2 mm (blue ◯).

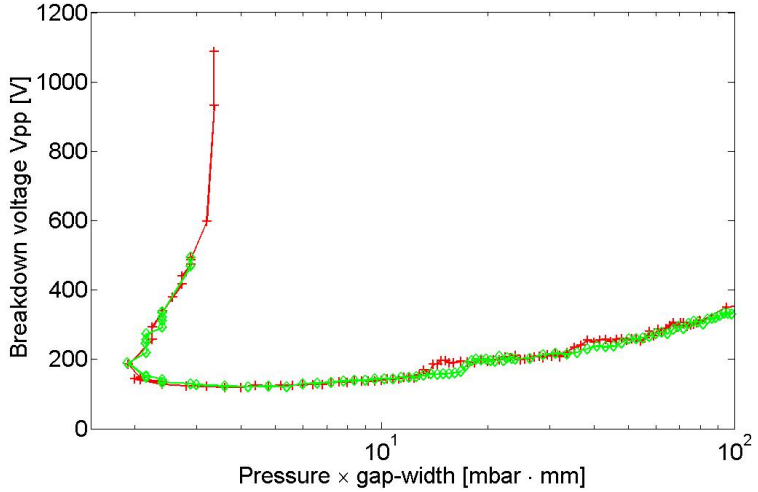

Figure 4.3: Comparison between 12 mm gap at 27.12 MHz (red +) and 8 mm gap at 40.68 MHz (green ◊) in argon

.

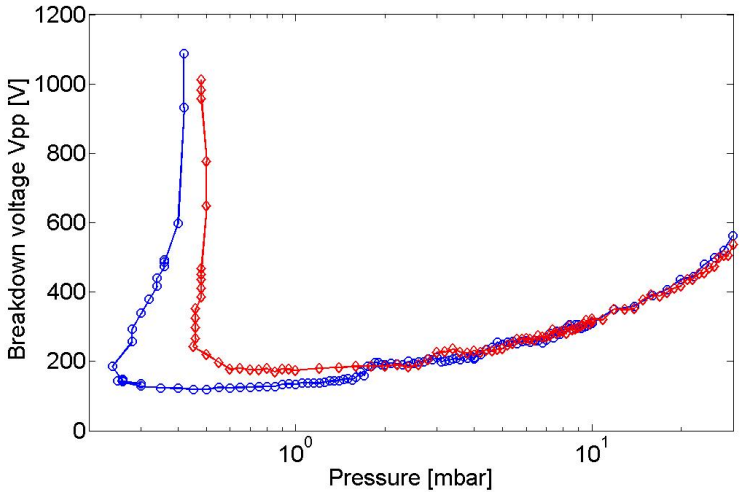

Figure 4.4: Breakdown curves for aluminium (blue circles) and copper (red diamonds) electrodes. Gap width 8 mm, argon.

4.1.2 Electrode Material

The electrode material can have an influence on the breakdown voltage, particularly at the left-hand side of the breakdown curve, where surface effects such as secondary electron emission start to dominate over electron generation in the volume. Figure 4.4 shows a comparison of breakdown curves in a 8 mm gap, for aluminium and copper electrodes. The curves overlap for pressures higher than 2 mbar, where breakdown happens predominantly due to volume processes. At lower pressures, surface processes, particularly secondary electron emission, start to play a role, and the breakdown voltage of the aluminium electrode is lower, since its secondary electron yield is higher, as shown in figure 4.5. The multivalued region of the left-hand side is therefore at lower pressures for aluminium.

Since aluminium is used as an electrode material in plasma deposition reactors, due to its oxide/fluoride layer being able to withstand the rigours of the fluoride plasma cleaning process between deposition, the question whether aluminium or its thin ($\sim$4 nm) intrinsic oxide layer is dominating the surface processes poses itself. This was investigated by comparing an aluminium electrode with its natural aluminium oxide layer with an anodised aluminium plate, where the oxide layer was 50 μm thick.

Figure 4.6 shows no great difference in the breakdown curve between the two materials. This means that the intrinsic aluminium oxide layer present on the aluminium electrodes is responsible for the contribution of secondary

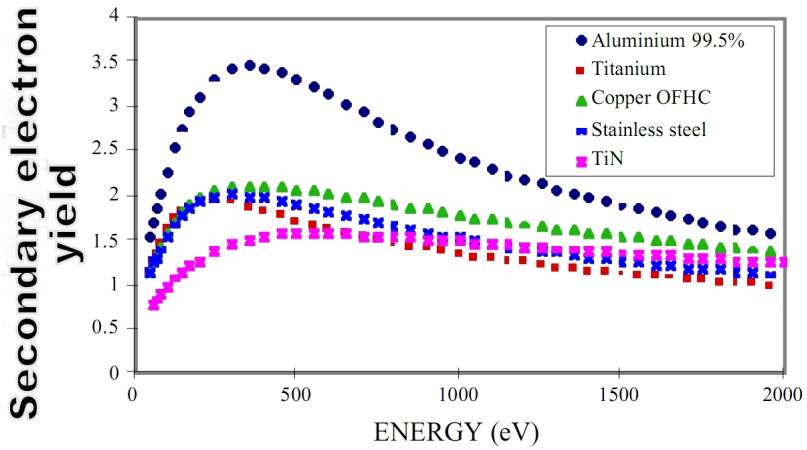

Figure 4.5: Secondary electron yield for different materials, from [34].

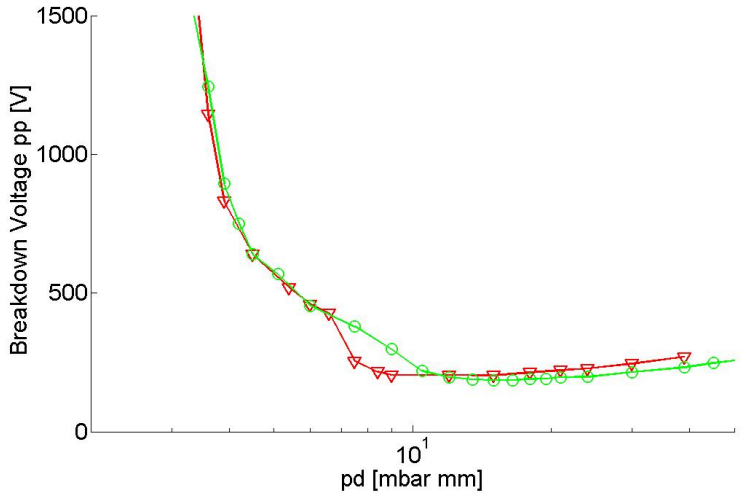

Figure 4.6: Breakdown between parallel plates, 3 mm gap, argon with aluminium electrodes (triangles) and anodized aluminium electrodes (circles).

Argon	SF_6	Oxygen	Hydrogen
15.7	16	13.6	13.6

Table 4.1: Ionisation energies of argon, oxygen and hydrogen from [39], and sulfur hexafluoride [40] in eV

electrons to the breakdown process. This makes sense, since the energy of the incident electrons (with an applied RF amplitude of 500 V a maximum of 500 eV) is not big enough to penetrate the layer: Using Bethe's formula [35] for the penetration depth

$$R = 0.0115E^{1.35} \tag{4.1}$$

with R the penetration depth in mg/cm^2 and E the electron energy in keV we get, with the density of aluminium oxide of 4 g/cm^{-3}, a penetration depth of about 1 nm. This is corroborated by the experimental results of Young [36].

4.1.3 Gas Type

The gas type has a considerable influence on the breakdown voltage, as shown in figure 4.8. Different molecules have different ionisation energies, and this greatly influences the electron avalanche that determines breakdown. However, a look at the ionisation energies involved shows that the breakdown behaviour is not simply dependent on the ionisation energy. Argon, by far the gas with the lowest breakdown voltage, has nearly the highest ionisation energy of the gases involved (see table 4.1).

This discrepancy is due to the presence of metastables (also responsible for the Penning effect [37] in gas mixtures containing a few percentages of argon, where metastable excited neutrals can ionise other neutral gas molecules, and greatly contribute to the breakdown process), who play a major role in the discharge despite making up a very low mole-fraction of the species, because only 4.14 eV are needed for their step-wise ionisation [38]. This results in rate constants for step-wise ionisation being superior to those of ground-state ionisation, see figure 4.7.

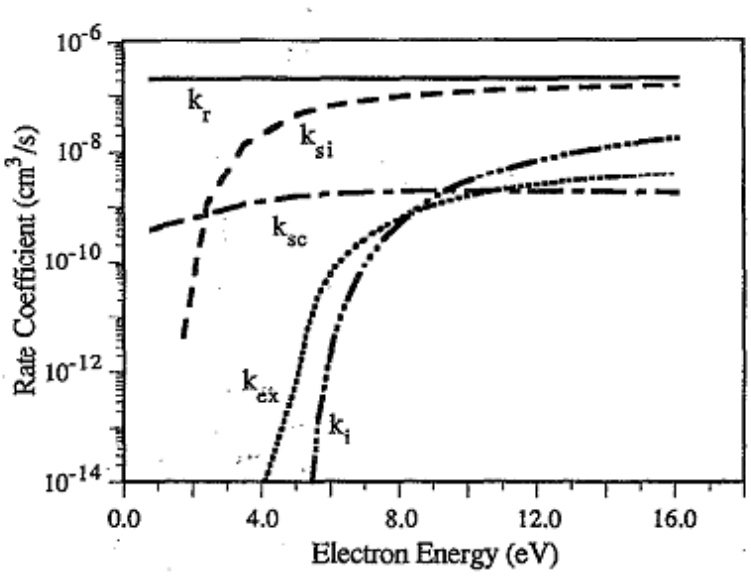

Figure 4.7: Rate constants for argon. k_{r}: quenching to resonant, k_{ex}: ground state excitation, k_{i}: ground state ionisation, k_{si}: step-wise ionisation via metastables, k_{sc}: superelastic collisions. From [38].

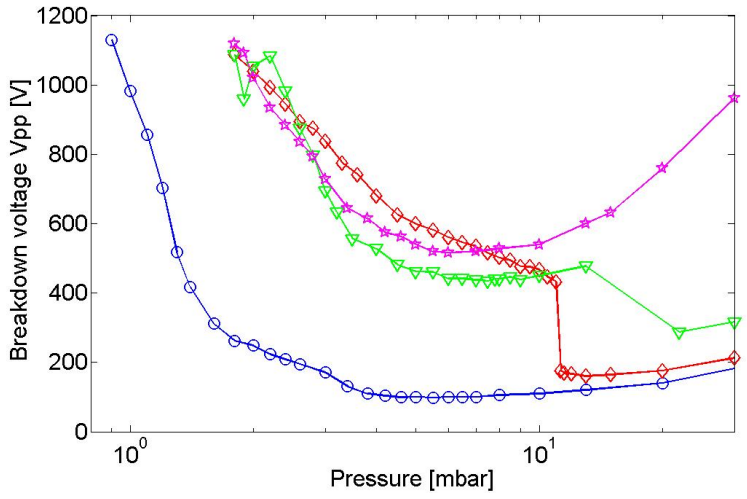

Figure 4.8: Breakdown between 3 mm parallel plates for argon (circles), sulphur hexafluoride (stars), oxygen (triangles) and hydrogen (diamonds)

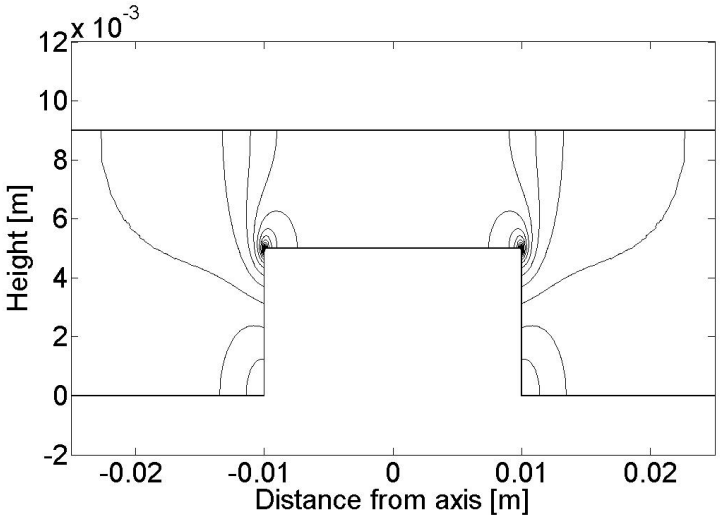

Figure 4.9: Contour lines for the magnitude of the electric field around a cylinder, with an applied voltage of 200 V with respect to the upper plane. The interval between lines is 9 kV/m. The curvature of the corners of the cylinder has a radius of 0.1 mm.

4.2 Structured Parallel Plates

Breakdown between parallel plates with surface structures will, of course, be different from breakdown between parallel plates with an equivalent gap. While small surface structures like scratches or ridges that are significantly smaller than the gap-width are not expected to have much influence, protrusions or holes that are of the same order of magnitude as the distance between the electrodes should significantly change the electric field between the plates, and hence the breakdown voltage.

4.2.1 Electric Field Between Structured Parallel Plates

Depending on the curvature of a point or corner, the electric field can be many times higher than for the surrounding area. Figure 4.9 shows an example of this: A cylinder protruding from the ground plane, its corners rounded with a radius of 0.1 mm. A voltage of 200 V is applied to it with respect to the grounded upper plane. While the parallel plate field between the cylinder and grounded upper plane is 50 kV/m, the field reaches 180 kV/m at the corners of the cylinder. In the extreme case of a protruding whisker, the electric field will be increased by a factor [41, 42]

$$\beta = \frac{h}{R} + 2 \tag{4.2}$$

relative to the parallel plate field V/d, where h is the height and R the radius of the whisker; V the applied voltage and d the gap between the parallel plates. It might be expected that the higher electric field would facilitate breakdown, and this assumption is often made when constructing parts with dark space shielding, i.e. sharp corners are avoided wherever possible. However, it can be shown [24] that sharp corners have in fact no discernible effect on the breakdown voltage, rather (and depending on the pressure) it is the gap-width between RF and ground electrode deviating from the parallel plate case that will lower the breakdown voltage under certain conditions.

To further investigate the behaviour of structured electrodes, the simplified cases of holes and cylindrical protrusions with varying diameters were investigated.

4.2.2 Cylindrical Protrusions

The quickest way to prove the assumption that the enhanced field around sharp corners has no influence on the breakdown voltage is to examine an extreme case: a 0.1 mm thin, 5 mm long wire protruding from an electrode inside a 9 mm wide gap (see also figure 3.4c). According to equation 4.2 the electric field at the tip of the wire should be about 50 times higher than the electric field between the parallel plates. Yet, figures 4.10 and 4.11 show that the breakdown curves are not altered by the wire.

Since sharp edges do not influence the breakdown voltage, parallel plates with either protrusions or holes will have a breakdown voltage only governed by pressure, gas type and the distance between the two electrodes. We therefore expect breakdown to occur at the part of the electrode presenting the most favourable distance for a given pressure. A wider gap breaks down more easily at low pressures (< 1.5 mbar), while a smaller gap breaks down more easily at high pressures. Consequently, an electrode structure presenting, for example, two different gap-widths will exhibit a breakdown curve that is a mixture of the wider gap for low pressures, and the smaller gap for high pressures, depending on the aspect ratio of the structures, (h/d). However, since the radius of a given electrode plate also plays a role in determining the breakdown voltage [21], the breakdown curve of an electrode with two different gap-widths may not simply be a mix of the breakdown curves for the respective parallel plate equivalents (the larger gap for low pressure, and the smaller gap for high pressure).

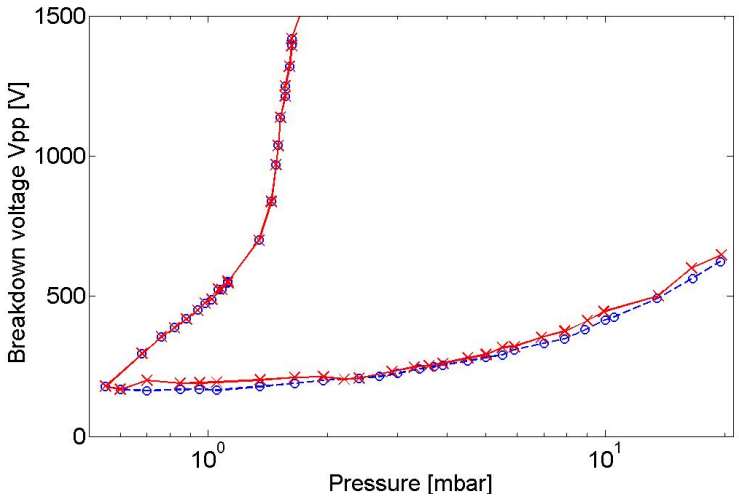

Figure 4.10: Measured breakdown of parallel plate with (crosses) and without (circles) protruding wire, in hydrogen.

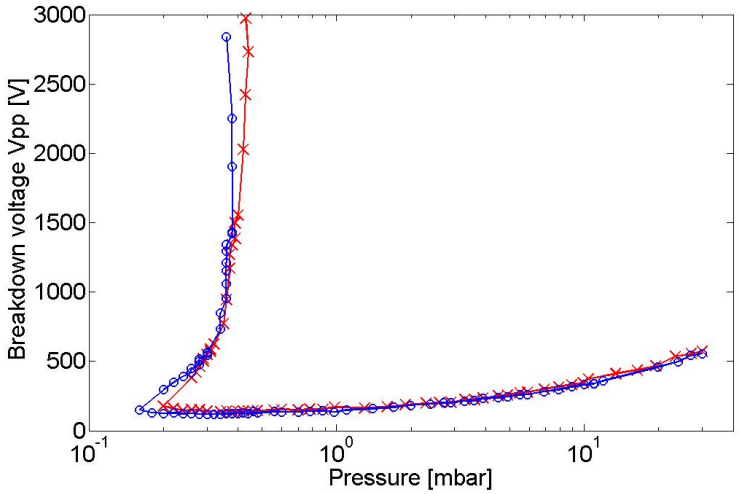

Figure 4.11: Breakdown between parallel plates with (crosses) and without (circles) protruding wire, in argon.

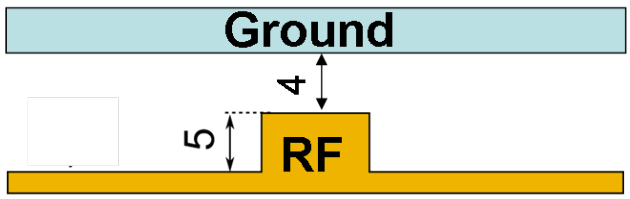

Figure 4.12: Cylinder electrode, schematic. The diameter of the cylinder varied between 4 and 18 mm.

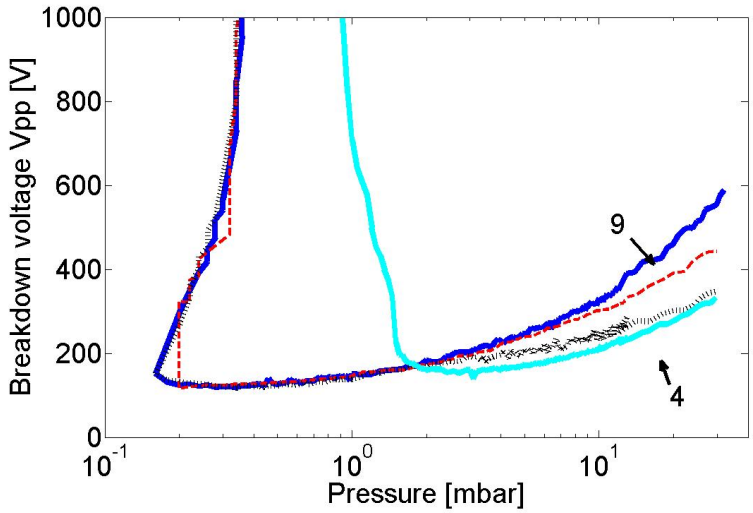

Figure 4.13: Breakdown curve of parallel plates (4 and 9 mm gap, see arrows) and cylinders, 4 (dotted) and 18 mm (dashed) diameter) in argon.

Figure 4.13 shows measurements of parallel plates with a 4 and 9 mm gap, as well as plates with a 4 respectively 18 mm diameter cylinder placed in the centre of the RF electrode (see figure 4.12). The cylinder has no effect on the breakdown voltage on the left-hand side - they all conform to the breakdown curve of the 9 mm parallel plate case for low pressures, as shown by figure 4.13. At higher pressures, the larger the diameter of the cylinder, the more closely the breakdown curves will follow that of the 4 mm parallel plate case. It seems reasonable to assume that breakdown happens at the top of the cylinder when the breakdown voltage conforms to that of a 4 mm parallel plate case, and around the cylinder when it conforms to that of a 9 mm parallel plate case. This assumption can be shown to be true, see chapter 5.

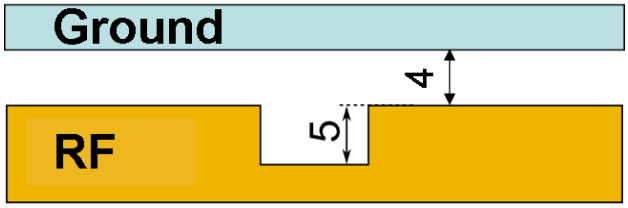

Figure 4.14: Hole electrode, schematic.

4.2.3 Cylindrical Holes

Holes present a behaviour similar to cylindrical protrusions, only this time it is the low pressure side that exhibits the effect of the changed gap-width, while at the high pressure side the breakdown curves of the cylinder plates conform to that of the 4 mm parallel plate gap.

Figures 4.15 and 4.16 show a comparison of parallel plate breakdown and breakdown between parallel plates with holes in the RF electrode (see figure 4.14), exhibiting the above-mentioned mixture of breakdown curves: For pressures higher than the Paschen-minimum of the 4 mm parallel plate electrode, the breakdown curves for the hole plates invariably follows the curve for 4 mm parallel plates. Breakdown in this region then occurs outside the hole, which is confirmed by simulation (see section 5). If the pressure is below the crossover point of the two parallel plate cases, the breakdown will occur at or inside the hole. Now the aspect ratio of the hole determines how much the larger depth of the hole influences the breakdown voltage. As the diameter increases, the breakdown curve for the hole plate approaches that of the 9 mm parallel plates.

4.2.4 Location of the Breakdown Event

From the measurements presented above, we can draw conclusions pertaining to *where* the breakdown in structured parallel plates happens. Adding a 5 mm high cylinder to a 9 mm gap does not change the breakdown behaviour at low pressures - it seems reasonable to assume that breakdown at those pressures happens around the cylinder, where the gap-width remains unchanged. At high pressures the breakdown voltage approaches that of the smaller, 4 mm gap on top of the cylinder, depending on its diameter. Since the only change to the experimental setup was the introduction of the cylinder, and the influence of edge-fields was ruled out via the experiment using a protruding wire (see figures 4.11 and 4.10), we therefore conclude that in this case breakdown happens on top of the cylinder.

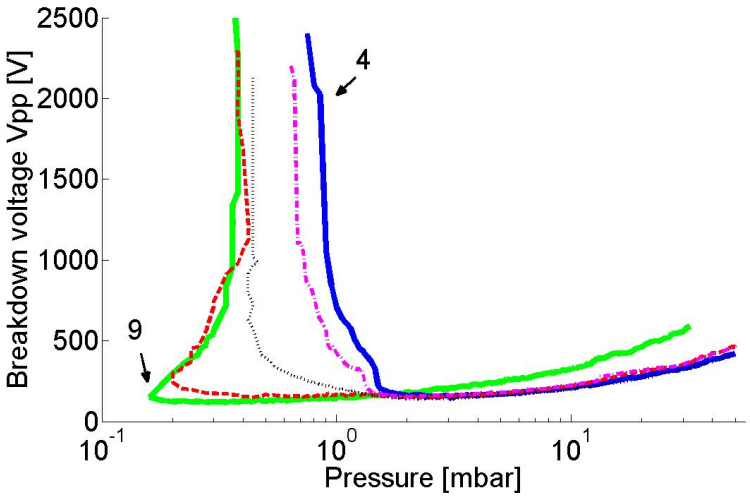

Figure 4.15: Breakdown curve of parallel plates (4 and 9 mm gap, see arrows) and hole plates, 4 (dash-dotted), 8 (dotted) and 18 mm (dashed) diameter in argon.

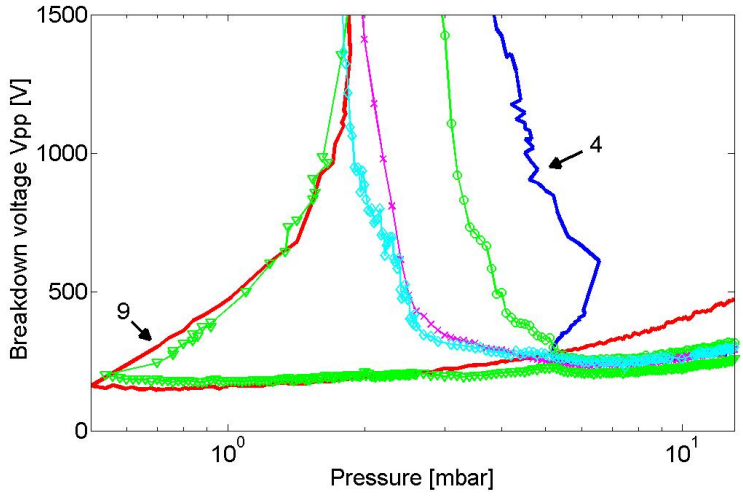

Figure 4.16: Breakdown curve of parallel plates (solid lines, 4 and 9 mm gap, see arrows) and holes, diameter: 4 mm (circles), 6 mm (crosses), 7 mm (diamonds) and 30 mm (triangles), in hydrogen.

The experiments with holes corroborate these assumptions. Adding a 5 mm deep hole to a 4 mm gap does not change the breakdown behaviour at high pressures - breakdown happens in the narrow gap surrounding the hole. At low pressures, however, the breakdown voltage approaches that of the 9 mm parallel plate case - the wider the hole, the greater the resemblance. Breakdown must therefore happen inside the hole.

These conclusions are born out by results of fluid-simulations presented in section 5.

4.3 Discussion

The results in Figures 4.13, 4.15 and 4.16 can be understood by visualising the way breakdown happens for parallel plates on the right and left sides of the minimum of the breakdown curve (which depends on pressure times gap-width). In both cases, initial free electrons (from cosmic rays or other external sources) are accelerated by the RF electric field. On the left, low pressure side of the breakdown curve, few gas molecules are present for ionisation in the gap, and the free electrons are in danger of being lost to the walls before a positive space-charge can be established. The electron oscillation amplitude (see discussion below) is large. A bigger gap translates to a smaller electric field for a given voltage and a longer distance between the electrodes, so fewer electrons are lost to the walls while oscillating in phase with the RF field. The breakdown voltage of a larger gap will therefore be lower. On the right hand side, gas molecules are present in abundance, and the smaller electric field of a larger gap will give the electrons less energy to ionise neutrals. The electron oscillation amplitude will be small, so the electron loss from the convection term will be small in both gaps. The breakdown voltage of a larger gap will be higher. Now, if multiple gap-widths are present, breakdown will naturally occur at the one most favourable for a given pressure. However, if the feature providing the optimal gap-width is too narrow, electrons will diffuse away laterally to the surrounding larger gap in the case of a cylinder-like protrusion, or to the inside walls in case of a hole. This explains why the enhanced electrical field of the wire had no effect in figures 4.10 and 4.11.

But what does *narrow* mean in this context? The following calculations may shed some light on this:

If we consider equation 2.12, and assume a simple parallel plate geometry with a cylindrical discharge chamber of radius R and height H with an axial electric field (see figure 4.17 for a schematic), it has been shown [15, 21, 25] (see also in chapter 2), that by demanding a periodic solution for Equation

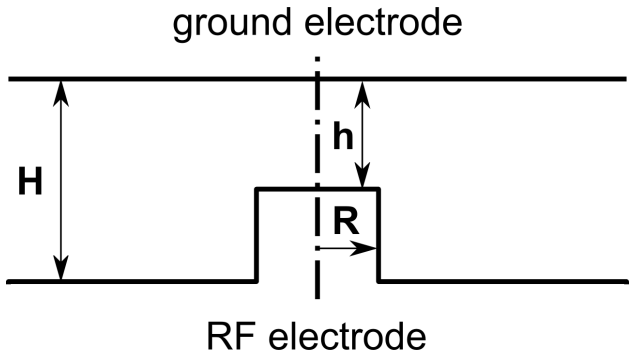

Figure 4.17: Schematic of a cylinder electrode

2.12 and via a separation of variables (r and z), the breakdown condition

$$\frac{\nu_\mathrm{i}}{D} = \frac{\pi^2}{\left(H - \frac{2V_\mathrm{e}}{\omega}\right)^2} + \left(\frac{2.4}{R}\right)^2 \tag{4.3}$$

can be found. The factor 2.4 comes from the fundamental diffusion mode distribution (a zero-order Bessel function of the first kind) [23], see chapter 2.

Following Kihara [15] further, we can equate $\nu_\mathrm{i} = \alpha V_\mathrm{e}$, and with the Townsend-formula $\alpha = A_0 p e^{\frac{-B_0 p}{E}}$ and rearranging, we get

$$A_1^2 p^2 e^{\frac{B_0 p}{E}} = \frac{1}{(H - 2A)^2} + \left(\frac{2.4/\pi}{R}\right)^2, \tag{4.4}$$

with the gas constants $A_1 = \frac{N}{p\pi}\sqrt{\frac{3\sigma\lambda}{c_i}}$, N the density of the gas, λ the collision cross section, σ a molecular constant for the effective cross section, $c_i = 0.8\sqrt{\frac{2eV_i}{m}}$, V_i the ionisation voltage and m the molecular mass; B_0 the coefficient from the well-known Townsend formula shown above and A is the electron oscillation amplitude $A = \frac{V_\mathrm{e}}{\omega} = \frac{E/(B_0 p)^2}{C_2 f/c}$ and $C_2 = \frac{\omega H}{\sqrt{2}} \frac{1}{c_i^2}\sqrt{\frac{\lambda}{3\rho}}$ and c the speed of light. For values for A_1, B_0 and C_2 see table 4.2. A calculation with the values of E, p and H used in the simulation found in figure 5.8 in chapter 5 gives an electron oscillation amplitude of $2A = 1.9$ mm, and this is indeed approximately the distance the electron density maximum is oscillating.

In the limit of a negligible electron oscillation amplitude A present on the right hand side of the breakdown curve - high pressure, high RF frequency,

Table 4.2: Coefficients from Lisovskiy and Yegorenkov, J. Phys. D:Appl. Phys., 27, 2340(1994) [43].

	A_1	B_0	C_2
	$\left[\mathrm{cm}^{-1}\mathrm{Torr}^{-1}\right]$	$\left[V\mathrm{cm}^{-1}\mathrm{Torr}^{-1}\right]$	[1]
Ar	9	184	7149
H_2	7.3	170	1250

low RF voltage; for example in a 9 mm parallel plate gap in argon, we find a breakdown voltage of 160 Volts at 10 mbar, which gives us $2A \sim 0.2$ mm - we can neglect the reduction of H by said amplitude, and directly write

$$A_1 p e^{\frac{B_0 p}{2E}} = \frac{1}{H_-} \tag{4.5}$$

with

$$\frac{1}{H_-^2} = \frac{1}{H^2} + \left(\frac{2.4/\pi}{R}\right)^2 \tag{4.6}$$

the reduced gap width (reduced due to diffusion to the sidewalls). We can then solve (4.5) for the breakdown voltage $V_\mathrm{B} = EH$:

$$V_\mathrm{B} = \frac{B_0 p H}{2\ln(A_1 p H_-)} \tag{4.7}$$

Which, in case of a parallel plate breakdown without sidewalls ($R \to \infty$), reduces to

$$V_\mathrm{B}^{||} = \frac{B_0 p H}{2\ln(A_1 p H)} \tag{4.8}$$

In a geometry as shown in Figure 4.17, we will assume that Equation 4.8 describes the breakdown voltage for the large gap H. We will further assume that the edge-fields do not contribute to breakdown, as shown experimentally (see figures 4.11 and 4.10). Breakdown in the small gap h above the cylinder with radius R is then described by the equation

$$V_\mathrm{B}^{c} = \frac{B_0 p h}{2\ln(A_1 p h_-)} \tag{4.9}$$

Already, we can see that all other parameters being equal, a smaller gap generally means a lower breakdown voltage for the right hand side of the breakdown curve. But if the cylinder in Figure 4.17 is small enough, the lateral diffusion effect (i.e. h_- in $\ln(A_1 h_-)$) will outweigh the advantage of the higher electric field E ($V_\mathrm{B}/h > V_\mathrm{B}/H$) for breakdown.

The threshold case, when breakdown is equally likely to happen on top of the cylinder or the surrounding parallel plate occurs when $V_\mathrm{B}^{||} = V_\mathrm{B}^{c}$. If R is smaller than in the threshold case, breakdown will happen between the parallel plates; if it is larger, then breakdown will happen on top of the cylinder.

Setting the height of the cylinder arbitrarily to half the gap-height (i.e. $h = H/2$), we get by equating (4.8) and (4.9)

$$\frac{B_0 pH}{2\ln(A_1 pH)} = \frac{B_0 pH}{4\ln(A_1 p h_-)} \quad \Rightarrow \quad \frac{1}{h_-^2} = \frac{A_1 p}{H}. \tag{4.10}$$

Using the relation (4.6) we get

$$\frac{1}{h^2} + \left(\frac{2.4/\pi}{R}\right)^2 = \frac{A_1 p}{H} \quad \Rightarrow \quad \frac{R}{h} = \frac{2.4}{\pi}\sqrt{\frac{2}{A_1 p h - 2}} \tag{4.11}$$

For a cylinder of 5 mm height in a 10 mm gap in argon, this ratio would be $R/h|_{10} = 0.19$ for a pressure of 10 mbar (i.e. a diameter of 2 mm), and $R/h|_{1} = 0.9$ for 1 mbar (a diameter of 9.2 mm). For pressures below $p = 2/(A_1 h)$ the radial losses prevail for any diameter - but as was mentioned earlier, this estimation is only valid for the right-hand branch, since we neglected the electron oscillation amplitude.

Comparison with experiment and simulation show that this analytical approach is only valid for a small range of pressures. A cylinder with 5 mm height and 4 mm diameter should have the crossover-point between parallel plate breakdown and breakdown on top of the cylinder at 2.7 mbar, according to Equation 4.11, while experiment and simulation show it at 2.2 mbar (see figure 4.13) . For a smaller cylinder the crossover point predicted by Equation 4.11 is too high: 9.2 mbar for a diameter of 2 mm, whereas simulation shows it at 2.3 mbar. This is because we made the assumption of a parallel plate field above the cylinder, which does not hold true for small cylinders. Likewise, for larger cylinders the pressure of the crossover point is so low that the electron oscillation can no longer be neglected, so the experimental values do not conform to Equation 4.11 any more.

This analytical treatment is then only useful for its qualitative assertions.

The inverse case, i.e. a hole in a parallel plate gap, is unfortunately not as easily treated. In small holes, the electric field will curve to the inside

walls, so the effective depth of the hole will be smaller. Still, it is reasonable to assume that the mechanism will be the same - lateral diffusion competing against increased ionisation. These cases are more accurately modelled using simulation, see chapter 5.

The results presented in this chapter have the potential of simplifying the design of dark space shielding or structured electrodes for industrial reactors. Even the highly simplified analytical treatment above can give an estimation for a minimum breakdown voltage of a given structure, by overlapping the parallel plate breakdown curves of the relevant gap-widths. It also shows that no special care has to be taken to prevent sharp corners in dark space shielding, and a simple way, especially with the simulation in chapter 5 to estimate the effects of protruding screw heads or holes.

Chapter 5

Breakdown Simulation

To complement and better understand the breakdown behaviour found and described earlier in chapter 4, a simulation using the fluid approximation was developed using the approach of Lisovskiy et al [44]. This chapter will show the implementation and swarm parameters used, compare the simulation to experimental data and present the results found via the simulation.

Breakdown generally occurs when the rate of electrons generated (by gas ionisation or secondary electron emission from the walls) is higher than the rate of electrons lost due to diffusion and drift to the walls, and recombination and attachment if applicable. Assuming the electrons behave like a fluid, the electron rate equation can be written as a drift-diffusion equation (shown by Kihara [15]), as already discussed in chapter 2 (see also equation 2.36):

$$\frac{\partial n_\mathrm{e}}{\partial t} = \nu_\mathrm{i} n_\mathrm{e} + \nabla \left(\mathfrak{D} \cdot \nabla n_\mathrm{e} \right) - \mathbf{V}_e \cdot \nabla n_\mathrm{e} \cos(\omega t). \tag{5.1}$$

Here n_e is the electron density, $\nu_\mathrm{i} = \alpha V_\mathrm{e}$ is the ionization frequency due to electron-neutral collisions, α is the third Townsend coefficient for ionisation, $\mathbf{V}_\mathrm{e}$ the amplitude of the electron drift velocity, $\mathfrak{D}$ is the electron diffusion tensor, $\omega = 2\pi f$ is the angular frequency of the electric field, and f the frequency of the RF supply.

As explained in chapter 2, equation 5.1 can be written as

$$\begin{aligned}\frac{\partial n_\mathrm{e}}{\partial t} = \nu_\mathrm{i} n_\mathrm{e} + \left(\frac{1}{r}\frac{\partial}{\partial r}(r D_\mathrm{L} \hat{E}_\mathrm{r}^2 + r D_\mathrm{T} \hat{E}_\mathrm{z}^2) \; - \frac{\partial}{\partial z}[\hat{E}_\mathrm{r}\hat{E}_\mathrm{z}(D_\mathrm{T} - D_\mathrm{L})] \right) \frac{\partial n_\mathrm{e}}{\partial r} + \\ + \left(\frac{1}{r}\frac{\partial}{\partial r}[r \hat{E}_\mathrm{r}\hat{E}_\mathrm{z}(D_\mathrm{T} - D_\mathrm{L})] \; + \frac{\partial}{\partial z}[D_\mathrm{T}\hat{E}_\mathrm{r}^2 + D_\mathrm{L}\hat{E}_\mathrm{z}^2] \right) \frac{\partial n_\mathrm{e}}{\partial z} - \mathbf{V}_e \cdot \nabla n_\mathrm{e} \cos(\omega t).\end{aligned} \tag{5.2}$$

in an arbitrary geometry, and as the simpler equation 2.12

$$\frac{\partial n_\mathrm{e}}{\partial t} = \nu_\mathrm{i} n_\mathrm{e} + D\frac{\partial^2 n_\mathrm{e}}{\partial z^2} - V_e \cos(\omega t)\frac{\partial n_\mathrm{e}}{\partial z}, \tag{5.3}$$

in a parallel plate geometry.

Similar work for parallel plate geometries was done by Lisovskiy et al [21, 44] who first published the fluid simulation used in this paper and investigated slightly larger electrode separations (∼20 mm), Sato and Soji [25] who concentrated on the right hand side of the breakdown curve and Smith et al [14] who investigated larger gaps of the order of centimetres.

5.1 Swarm Parameters

The swarm parameters $\alpha, D_\mathrm{T}, D_\mathrm{L}$ and V_e necessary to solve Equations 5.2 and 5.3 were taken primarily from [21, 45, 46] for argon, and [47, 48, 49, 50] for hydrogen. For E/N values where there were no experimental values, (i.e. $E/N > 3000$ Townsend) the Boltzmann solver BOLSIG+ (Kinema Research Software, www.kinema.com) developed by Hagelaar and Pitchford [51] was used to calculate the swarm parameters. They were then fitted with analytic formulas (see below) and together with Equation 5.1 inserted into the commercial finite-element solver Comsol (Comsol Inc., www.comsol.com).

Figure 5.1 shows the values for the measured reduced electric field E/N for breakdown curves in argon and hydrogen between parallel plates, for gaps of 4 and 9 mm. Accordingly, swarm parameters have to be found for values of the reduced electric field between 40 and 20000 Townsend.

5.1.1 Drift Velocity

Data for the drift velocity V_d was taken from [46] and [47]. For argon, the fit used was

$$V_\mathrm{e} = 1281.77\left(\frac{E}{N}\right)^{0.9042}, \tag{5.4}$$

and for hydrogen

$$V_\mathrm{e} = 1707.87\left(\frac{E}{N}\right)^{0.9579}. \tag{5.5}$$

This is close to the theoretical expression we get from [8]

$$\mu = \frac{V_\mathrm{e}}{E} = \frac{e}{m_\mathrm{e}\nu_\mathrm{en}}, \tag{5.6}$$

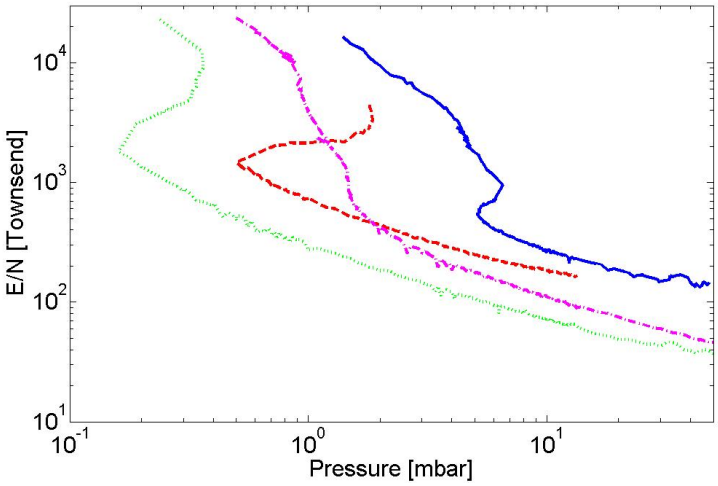

Figure 5.1: Reduced field values over pressure measured in hydrogen for 4 mm (solid line) and 9 mm (dashed line), and in argon for 4 mm (dash-dotted line) and 9 mm (dotted line) parallel plate breakdown.

with ν_{en} the electron-neutral collision frequency, which gives

$$V_{\text{e}} \propto \frac{E}{N}. \tag{5.7}$$

Figure 5.2 shows the fits and the experimental data for the electron drift velocity, plotted over the reduced field E/N in Townsend.

5.1.2 Townsend Coefficient

The third Townsend coefficient, which describes the ionising events per unit length for an electron of a certain energy (the first being the number of ions per unit length generated by a positive ion moving from anode to cathode, and the second being the number of electrons released from a surface by the impact of an ion) was fitted following the experimental data in [46] and [48]. The fit used for argon was

$$\begin{aligned}\alpha = \exp\Bigg[&-0.01193\ln^4\left(\frac{E}{N}\right) + 0.3265\ln^3\left(\frac{E}{N}\right) - \\ &-3.556\ln^2\left(\frac{E}{N}\right) + 18.85\ln\left(\frac{E}{N}\right) - 86.25\Bigg],\end{aligned} \tag{5.8}$$

which was arrived at by fitting the log-log plot with a fourth-order polynomial, and

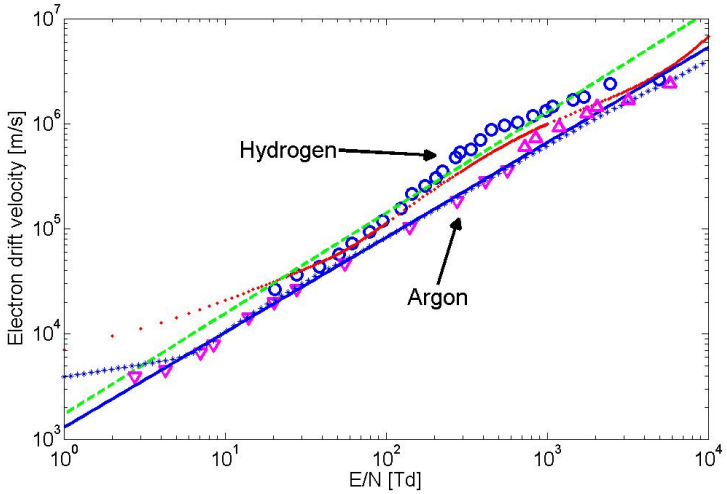

Figure 5.2: Electron drift velocity. Argon: solid line (fit, eq. 5.4), triangles (experimental data, from [46]) and stars (BOLSIG). Hydrogen: broken line (fit, eq. 5.5), triangles (experimental data,△ from [47]), ▽ from [46]) and dots (BOLSIG).

$$\alpha = \exp\left[-834.1\left(\frac{E}{N}\right)^{-1.184} - 47.17\left(\frac{E}{N}\right)^{-0.004184}\right] \tag{5.9}$$

was used as a fit for hydrogen, for which a rather simpler power-fit could be found. Figure 5.3 shows the fits and the experimental data, third Townsend coefficient plotted over the reduced field E/N in Townsend.

5.1.3 Diffusion

The diffusion coefficient is anisotropic, and was represented as the transversal diffusion coefficient D_{T} at right angles to the electric field, and the longitudinal diffusion coefficient D_{L} along the electric field. Figure 5.4 shows a comparison between the longitudinal diffusion coefficient over mobility $\mu = V_d/E$, plotted over the reduced field E/N for hydrogen and argon. Figures 5.5 and 5.6 show a comparison between the transversal and longitudinal diffusion coefficients for argon and hydrogen, respectively.

The fit used for the longitudinal diffusion coefficient in argon was, as for

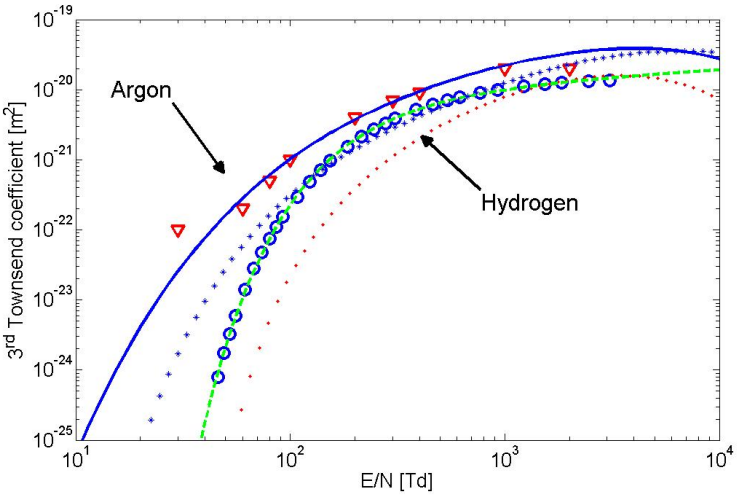

Figure 5.3: Third townsend coefficient. Argon: solid line (fit, eq. 5.8), triangles (experimental data, from [46]) and stars (BOLSIG). Hydrogen: broken line (fit, eq. 5.9), circles (experimental data, from [48]) and dots (BOLSIG).

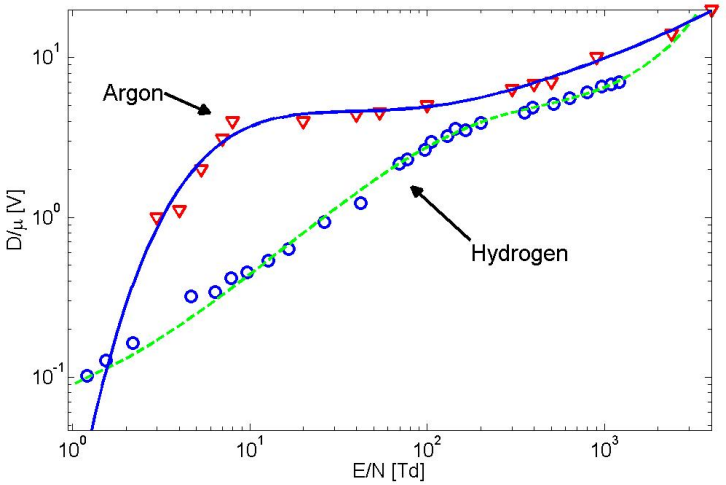

Figure 5.4: Longitudinal diffusion coefficient over mobility. Argon: solid line (fit, eq. 5.10) and triangles (experimental data, from [46]). Hydrogen: broken line (fit, eq. 5.12) and circles (experimental data, from [49]).

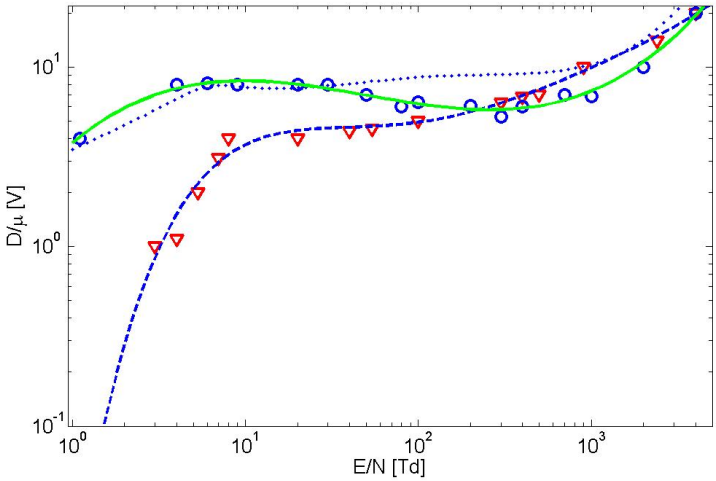

Figure 5.5: Diffusion coefficient over mobility in argon: solid line (fit, eq. 5.11), circles (experimental) transverse diffusion and dots (BOLSIG); broken line (fit, eq. 5.10) and triangles (experimental) longitudinal diffusion. Experimental data from [46].

the Townsend coefficient, a polynomial fit for the log-log plot,

$$D_{\mathrm{L}} = \exp\left[0.001236\ln^5\left(\frac{E}{N}\right) - 0.03671\ln^4\left(\frac{E}{N}\right) + \right.$$
$$\left. +0.4232\ln^3\left(\frac{E}{N}\right) - 2.3\ln^2\left(\frac{E}{N}\right) + 5.952\ln\left(\frac{E}{N}\right) - 4.42\right], \tag{5.10}$$

while the transverse diffusion coefficient was fitted as

$$D_{\mathrm{T}} = \exp\left[0.001236\ln^3\left(\frac{E}{N}\right) - \right.$$
$$\left. -0.2489\ln^2\left(\frac{E}{N}\right) + 0.8063\ln\left(\frac{E}{N}\right) - 1.33\right]. \tag{5.11}$$

In hydrogen, the longitudinal diffusion coefficient was

$$D_{\mathrm{L}} = 0.0907\left(\frac{E}{N}\right)^{0.7}, \tag{5.12}$$

and the transverse diffusion coefficient was fitted as

$$D_{\mathrm{T}} = \left[4.134\exp\left(4.545\times10^{-4}\frac{E}{N}\right) - \right.$$
$$\left. -4.085\exp\left(-9.529\times10^{-3}\frac{E}{N}\right)\right]. \tag{5.13}$$

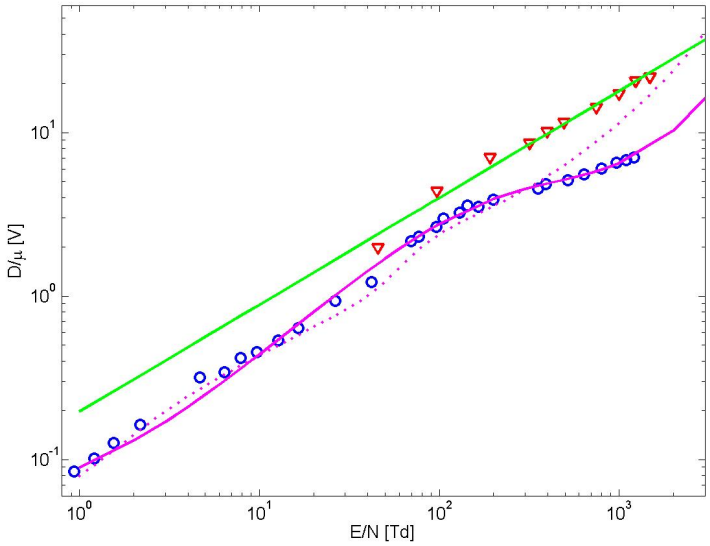

Figure 5.6: Diffusion coefficient over mobility in hydrogen: solid line (fit, eq. 5.12) and triangles (experimental data, from [50]) longitudinal diffusion; broken line (fit, eq. 5.10), circles (experimental data, from [49]) and dots (BOLSIG) transverse diffusion.

5.2 Implementation

The simulation was implemented in a commercial finite element solver [52], controlled by a numerical computing environment [53]. Both two-dimensional geometries like rotationally symmetric electrodes with surface structures and parallel plates with finite dimensions and a one-dimensional geometry (infinite parallel planes) could be simulated. All surfaces were assumed as electron sinks, with the boundary condition for the electron density

$$n_e|_{\text{surface}} = 0. \tag{5.14}$$

The ionisation rate ν_i, i.e. the ionisation of atoms or molecules by electron impact was assumed to be invariant with time and therefore determined by the effective RF field E_{eff} [18, 44] :

$$E_{\text{eff}} = \frac{E_{\text{rf}}}{\sqrt{2}} \frac{\nu_{\text{en}}}{\sqrt{\omega^2 + \nu_{\text{en}}^2}} \tag{5.15}$$

where E_{rf} is the amplitude of the RF field, and ν_{en} the rate of electron-neutral collisions.

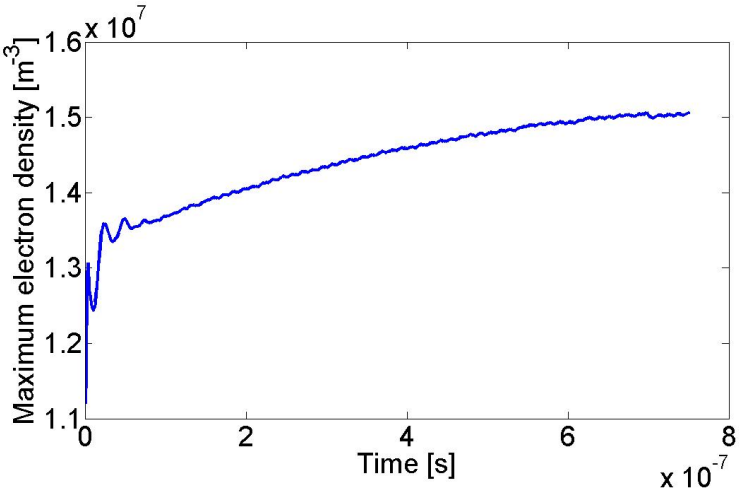

Figure 5.7: Maximum electron density over time for breakdown in hydrogen, for an electrode plate with a cylindrical protrusion.

The initial electron density at $t = 0$ was arbitrarily set to $n_{e0} = 10^7 \mathrm{m}^{-3}$. This low density will not distort the RF-field generated by the voltage of the RF electrode in the gap, which means that not only instead of using the Poisson equation

$$\nabla^2 \phi = \frac{e(n_\mathrm{e} - n_\mathrm{i})}{\epsilon_0}, \tag{5.16}$$

with ϕ the electric potential, to calculate the electric field in the gap, we can rely on the simpler Laplace equation

$$\nabla^2 \phi = 0, \tag{5.17}$$

but we can disregard the ions entirely, only simulating the electrons. This follows from the assumption that we can decide whether breakdown will happen or not at the very beginning of an electron avalanche, before the electron or ion densities become great enough to generate a space charge. Furthermore, in an RF field of the frequencies considered in this work, ions are too slow to have a part of ionisation events (see chapter 2), with a maximum kinetic energy of much less than 1 eV.

These considerations speed up the drift-diffusion simulation (the field labelled "Solve diffusion/drift equations" in figure 5.9) considerably, since it now reduces to a calculation of the static electric field $\mathbf{E_0}$, which is then modulated by $\cos(\omega t)$ and subsequently used in the drift-diffusion part to calculate the fluid equations of a single species, n_e.

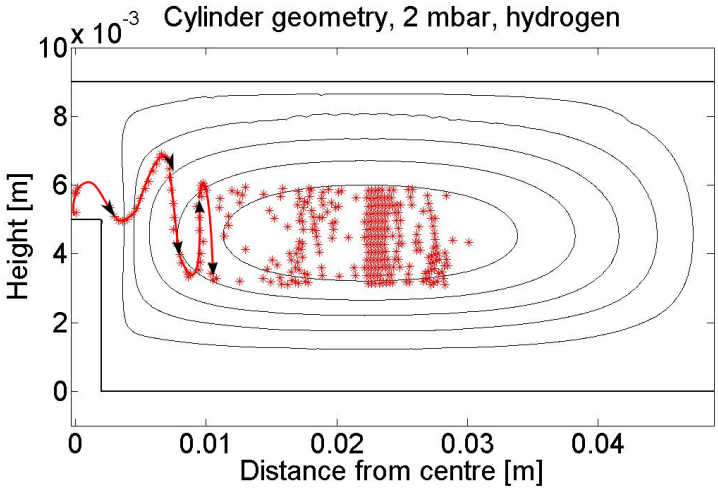

Figure 5.8: Electron density for a breakdown in hydrogen at 10 mbar, for an electrode plate with a cylindrical protrusion. The symmetry axis is on the left side. The crosses show the location of the maximum electron density during the simulation.

To decide whether or not breakdown had happened, the program monitored the maximum electron density n_e^{max} in the simulation. Since breakdown prior to the forming of space-charge and sheaths can be viewed as a runaway multiplication of electrons, a given RF voltage was considered to result in breakdown if, after a number of RF cycles (30 to 60, depending on the pressure, since high pressures (>5 mbar) can take longer to equilibrate), the maximum electron density was either flattening out, or continued to rise, as shown in figure 5.7.

Using the maximum electron density in the discharge volume instead of the electron density at a fixed point, while slowing down the calculation because of the sorting needed, did allow to localise *where* the breakdown happened. Figure 5.8 shows a breakdown simulation for an electrode with a cylindrical protrusion in 10 mbar hydrogen. As time passes, the maximum electron concentration, which starts off on top of the cylinder because of the localised, higher electric field encouraging ionisation, moves to the wider gap surrounding the cylinder as the diffusive losses near the cylinder overwhelm the higher ionisation rate there. Breakdown then happens in the middle of the wider gap, where the maximum can be seen oscillating with the applied RF field.

Figure 5.9 shows a flowchart of the simulation implementation for the right-hand branch of the breakdown curve. The program first reads the geometry, the fits for the swarm parameters and the boundary conditions.

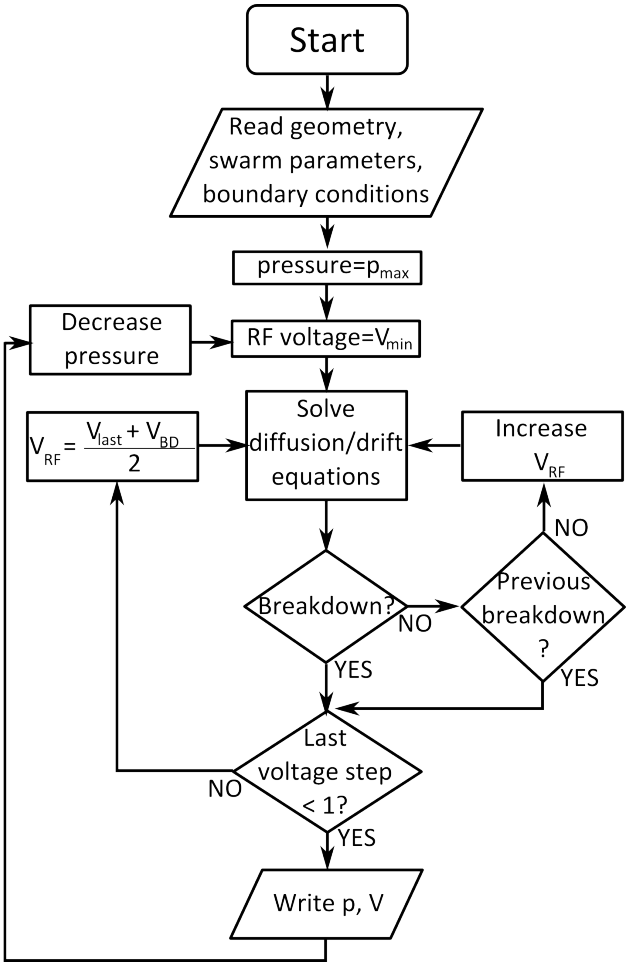

Figure 5.9: Flow chart of the simulation code. V_{last} is the last RF voltage that did not result in a breakdown.

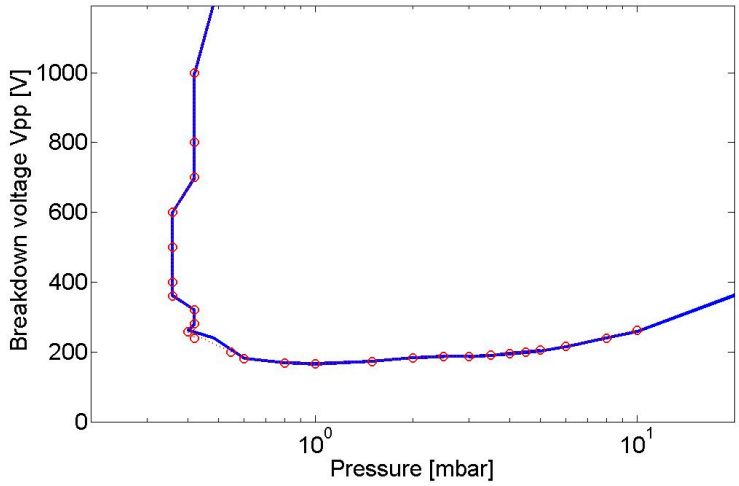

Figure 5.10: Comparison between anisotropic (circles, red) and isotropic (solid line) diffusion coefficient in a simulation for a 8 mm radius cylinder electrode in argon.

Then, starting from a maximum pressure and minimum RF voltage supplied by the user, the RF voltage is increased until breakdown happens. Then the program tries again, using an RF voltage halfway between the breakdown voltage and the last RF voltage that did not result in a breakdown. When the voltage step is smaller than 1 V, the lowest RF voltage that did result in a breakdown is considered the definitive breakdown voltage, and is recorded together with the pressure. Then the pressure is reduced with a step-size determined by the user.

The left-hand branch is found by a similar algorithm, except here the voltage is fixed step by step, and the program varies the pressure to find the breakdown point in the (p, V) phase-space.

5.3 Anisotropic and Isotropic Diffusion

As has been previously mentioned (see chapter 2), electron diffusion in gases is generally anisotropic with regard to an applied electric field. However, running the simulation with isotropic (using D_{L} as diffusion coefficient) and anisotropic diffusion showed only very small differences when simulating cylinder and hole electrodes, as shown in figures 5.10 for a 16 mm diameter cylinder in argon, and in figures 5.11 and 5.12 for 16 mm diameter holes in hydrogen.

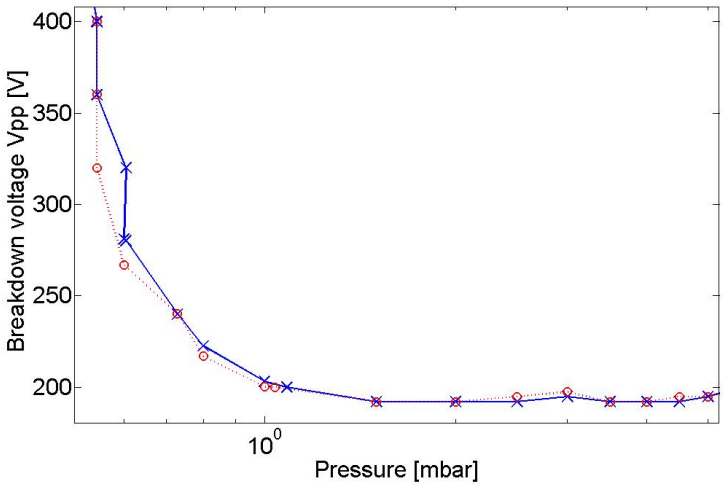

Figure 5.11: Comparison between anisotropic (circles, dotted red) and isotropic (crosses, solid blue) diffusion coefficient in a simulation for a 8 mm radius hole electrode in argon.

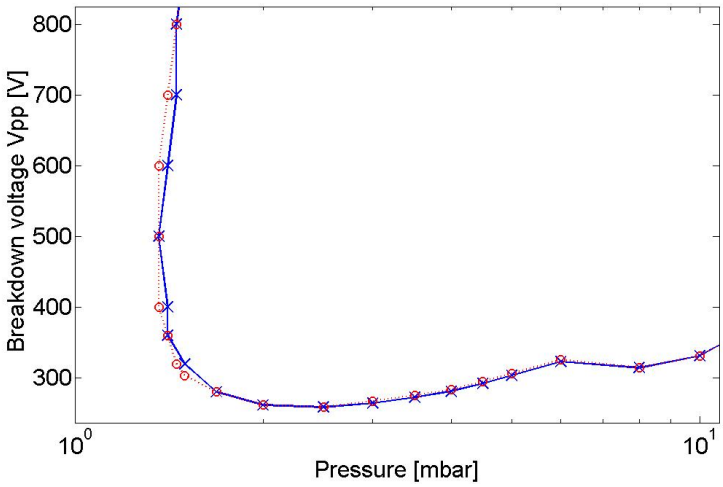

Figure 5.12: Comparison between anisotropic (circles, dotted red) and isotropic (crosses, solid blue) diffusion coefficient in a simulation for a 8 mm radius hole electrode in hydrogen.

Therefore, all simulations shown in this thesis were run using an isotropic diffusion coefficient (equation 5.3, see also equation 2.12 in chapter 2), as the simulation ran noticeably faster this way.

5.4 Influence of the Swarm Parameters

The swarm parameters drift velocity V_e, third Townsend coefficient α and diffusion coefficient D have different influences on the breakdown voltage. In this section this influence will be investigated in argon. Knowing how argon behaves if we change its swarm parameters will help to judge how gases different from argon will break down, based on the difference of their swarm parameters from argon.

Figure 5.13 shows how changing the drift velocity V_e will influence the breakdown voltage. The simulation was run with the fit for drift velocity presented in equation 5.5, and then with $V_e \times 0.75$ and $V_e \times 1.75$. It is logical to assume that the influence of V_e is greatest on the left-hand side of the breakdown curve, where convection dominates, and this is indeed born out by the simulation. The effect of changing the drift velocity is most dramatic on the position of the left-hand branch relative to pressure. This is easy to understand: a lower drift velocity will result in a lowering of the breakdown pressure in this region - effectively shifting the left-hand branch to a lower pressure - since the electrons, being slower, will have a longer residence time between the electrode plates. The turning point of the breakdown curve, where it doubles back on itself as the electron oscillation amplitude becomes larger than the gap-width, is shifted to the left if we decrease the drift velocity. Then, the 'curving back' of the breakdown curve as described in chapter 2 is also less pronounced, since the lower drift velocity and therefore longer residence time results in less of a need for higher neutral densities. As previously explained (see chapter 2), at higher pressures the electron oscillation amplitude becomes negligible, hence the near convergence of the three different simulation curves to the right in figure 5.13.

Varying the third Townsend coefficient α also impacts the breakdown voltage at low pressures most. Electrons here will not last a whole RF cycle before being absorbed by the wall, so the ionisation frequency $\nu_i = \alpha V_e$ is most important for breakdown. Increasing α will lower the breakdown pressure for the left-hand branch even more dramatically than lowering V_e did above, as shown in figure 5.14. With a greater Townsend coefficient, even a few electrons remaining in the gap between half-cycles will suffice, so the turning point is pushed to lower pressures. And since a higher Townsend coefficient directly results in higher ionisation rates, the curving back of the

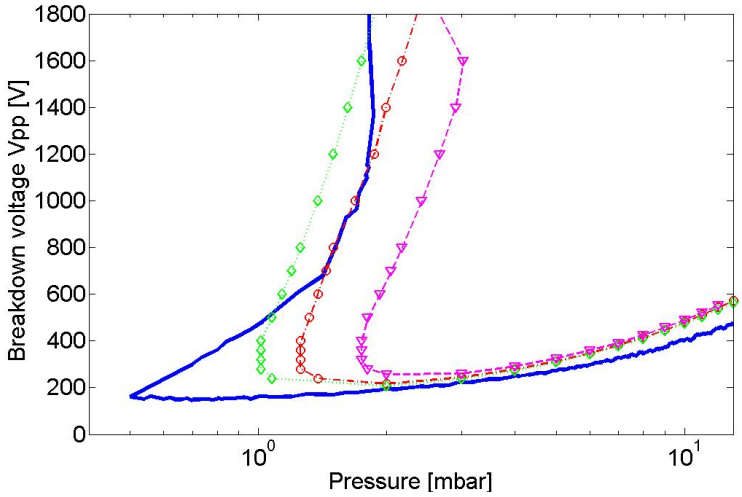

Figure 5.13: Influence of varying the drift velocity V_e on the breakdown curve between parallel plates, 9 mm gap-width, hydrogen: Solid line experiment, red circles simulation, green diamonds $V_e \times 1.5$ and magenta triangles $V_e \times 0.75$.

breakdown curve is again less pronounced. Contrary to the drift velocity, even at high pressures α is an essential parameter, and its influence remains important.

Changing the diffusion coefficient presents a more complicated effect, as shown in figure 5.15. At high pressures, decreasing D will effectively increase the number of electrons in the gap, since diffusion to the walls will be decreased, hence the lowering of the breakdown voltage at high pressures. The steep left-hand branch of the breakdown curve, however, shows the opposite behaviour: a decreased diffusion coefficient shifts the breakdown curve to the right, as electron losses in this region are mostly convective, and strong diffusion will counteract them partially.

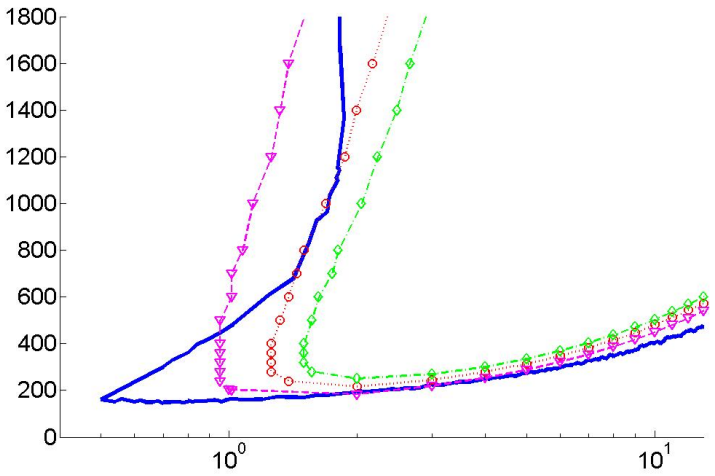

Figure 5.14: Influence of varying the third Townsend coefficient α on the breakdown curve between parallel plates, 9 mm gap-width, hydrogen: Solid line experiment, red circles simulation, green diamonds $\alpha \times 0.75$ and magenta triangles $\alpha \times 1.5$.

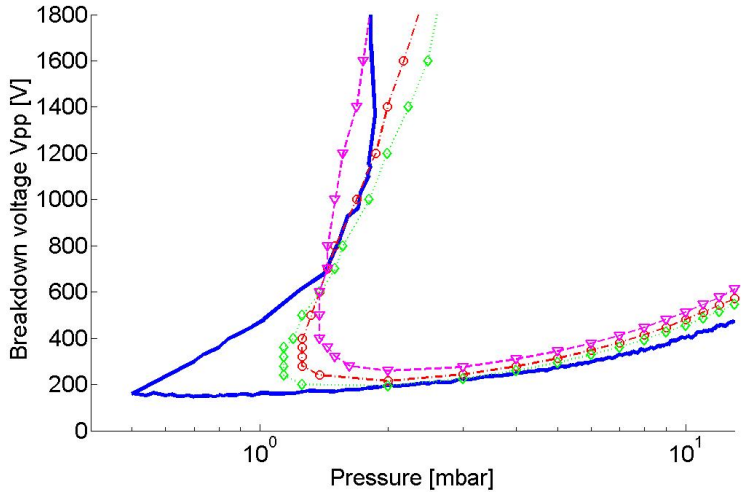

Figure 5.15: Influence of varying the diffusion coefficient D on the breakdown curve between parallel plates, 9 mm gap-width, hydrogen: Solid line experiment, red circles simulation (isotropic diffusion), green diamonds $D \times 0.75$ and magenta triangles $D \times 1.5$.

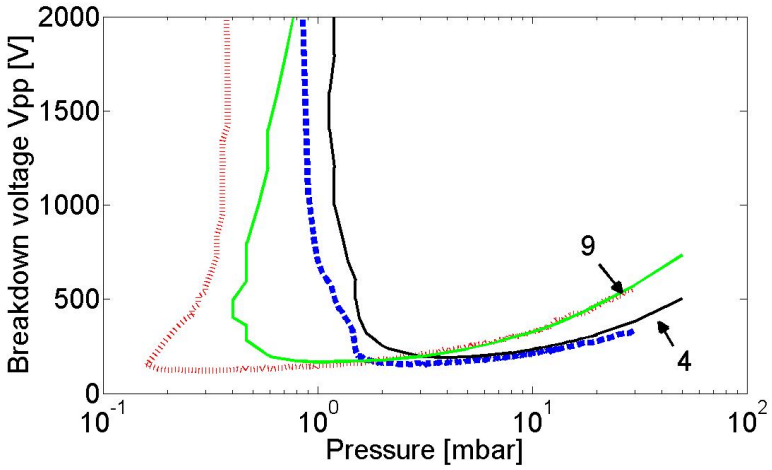

Figure 5.16: Comparison between experiment (dashed lines) and simulation (solid lines) for parallel plates (4 and 9 mm gap, see arrows) in argon.

5.5 Comparison with Experiment

Comparison between parallel plate experiment and simulation (see Figure 5.16) in argon shows a reasonably good agreement, especially for the right-hand side of the breakdown curve. The left-hand side of the simulated breakdown curve is situated at somewhat higher pressures than in the experiment, and furthermore the shape at the lower left (i.e. low pressure, low voltage) is much sharper in the experiment. This is probably due to surface effects like secondary electron emission, which are not included in the simulation.

In hydrogen, the simulation is somewhat less accurate, consistently predicting somewhat higher breakdown voltages at the right-hand side of the breakdown curve (see figure 5.17). Furthermore, the left-hand branch of the 4 mm parallel breakdown simulation shows lower pressures at high voltages than the experiment. It is unclear why the simulation in hydrogen performs worse than the one in argon. It is not the result of incorrect swarm parameters, as varying them did not improve the simulation. However, it is possible that the measured breakdown voltages were slightly lowered due to impurities in the vacuum chamber.

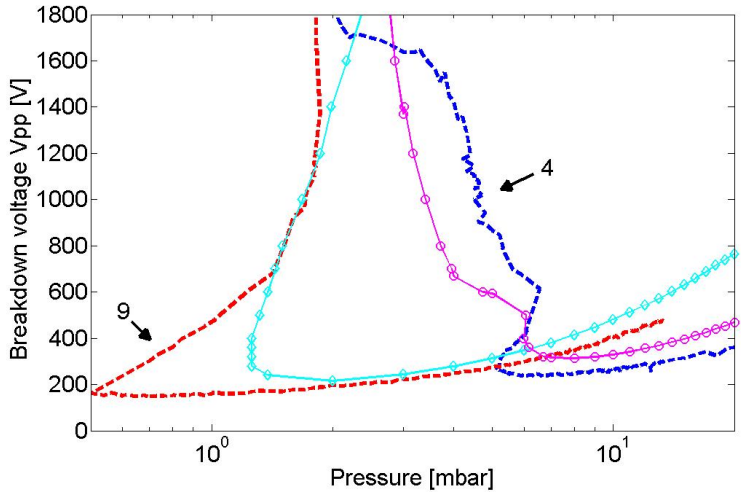

Figure 5.17: Comparison between experiment (dashed lines) and simulation (solid lines) for parallel plates (4 and 9 mm gap, see arrows) in hydrogen.

5.6 Breakdown Between Structured Parallel Plates

The simulation confirmed the behaviour of breakdown in cylinder and hole electrodes (see section 4.2.4). In a structured electrode with two different gap-widths, breakdown will predominantly happen in the wider gap at low pressures, and in the narrow gap at high pressures. This is illustrated in figures 5.18 and 5.19. Figure 5.18 shows the electron density at breakdown in a cylinder electrode in hydrogen. At lower pressures, breakdown happens in the wide gap surrounding the cylinder (top), increasing the pressure moves the breakdown to the narrow gap between the ground electrode and the top of the cylinder (bottom). Figure 5.19 shows the same behaviour for a hole electrode: At low pressures (top) breakdown happens in the wider gap, i.e. inside the hole, while at higher pressures (bottom) it shifts to the narrower gap surrounding the hole.

The simulation also shows how the electron cloud will oscillate during an RF cycle: Figure 5.20 shows the electron density in phase-steps of 45 degrees during one RF cycle for breakdown in argon. The cloud, which has its maximum density above the cylinder to the left, oscillates about 90 degrees out of phase with the RF electric field.

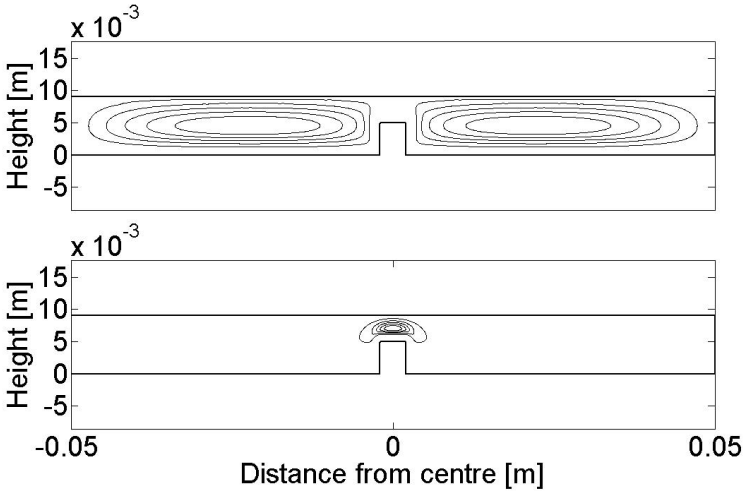

Figure 5.18: Electron density in hydrogen at breakdown for an electrode plate with cylindrical protrusion (5 mm height, 4 mm diameter). The contour lines represent steps of about $8 \cdot 10^6$ electrons/m^3. Breakdown occurs between the parallel plates at low pressure (2 mbar, 217 V_{pp}, top), but above the cylinder at high pressure (10 mbar 347 V_{pp}bottom).

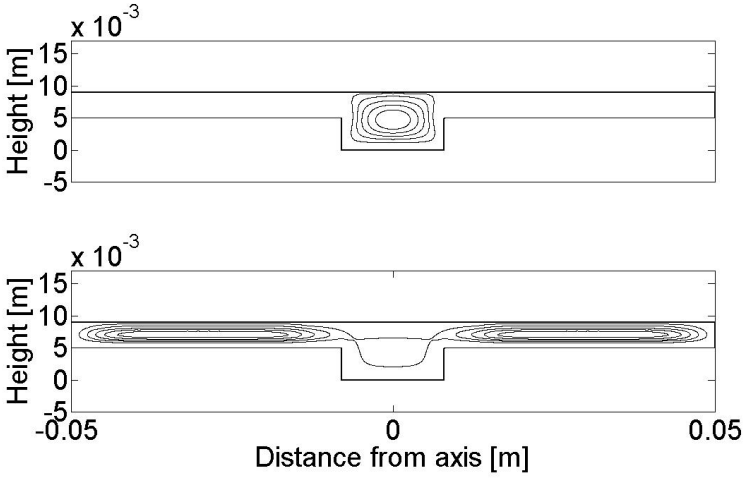

Figure 5.19: Electron density in hydrogen at breakdown for an electrode plate with a hole (5 mm deep, 16 mm diameter). The contour lines represent steps of about 10^6 electrons/m^3. Breakdown occurs in the hole at low pressure (2 mbar, 260 V_{pp}, top), but between the parallel plates at high pressure (10 mbar, 332 V_{pp}, bottom).

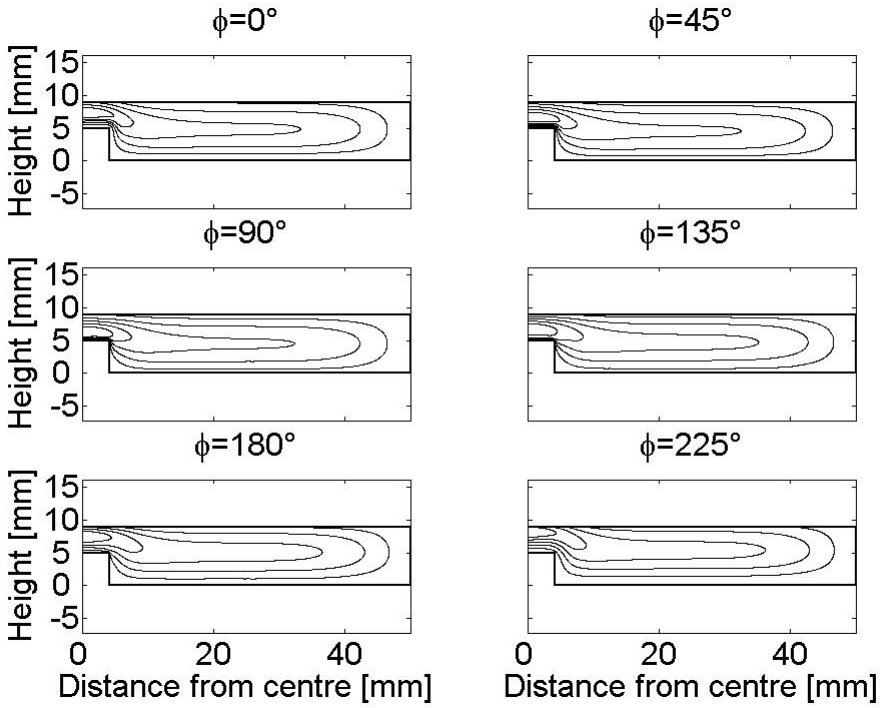

Figure 5.20: Electron density in argon at breakdown for an electrode plate with a cylinder (5 mm high, 8 mm diameter) at 95 V_{pp} for different points in the RF cycle. The contour lines represent steps of about 10^6 electrons/m^3. The maximum electron density on top oscillates with a phase-shift of about 90 degrees to the electric field.

5.7 Conclusion and Further Work

With the fluid simulation we developed a tool that can be used to calculate the breakdown voltage for arbitrary geometries in common plasma-processing pressure ranges, as long as surface effects like secondary electron emission can be neglected. The simulation also shows that the conclusions drawn in chapter 4 are correct: Breakdown in a structured electrode will happen where the gap-width presented to the gas equals the equivalent parallel plate whose breakdown voltage is lowest, as long as the structure providing the gap is sufficiently wide, as diffusive losses to either side walls for a hole, or to the surrounding wider gap for a protrusion will limit its influence otherwise.

It should be possible to include some sort of secondary emission mechanism into the simulation as well, for example by sampling the electron density and drift velocity near the surface and assuming a Maxwellian energy distribution of the electrons. This would make the simulation more accurate at low pressures.

Even as it stands now, the breakdown simulation should take out much of the guesswork involved in designing showerheads or dark space shielding in general, and facilitate and speed up the design stage.

Chapter 6

Hollow Cathodes

As part of the investigation into parasitic plasmas (see chapter 1), hollow cathodes were investigated. Hollow cathodes were first mentioned by Paschen in 1916 as a means of investigating helium lines [54], and are normally driven as DC discharges [55, 56], but an RF hollow cathode discharge exists as well. Figure 6.1 shows the basic principle of an RF driven hollow cathode (from [57]). Briefly, the most important features that differentiate hollow cathodes from normal RF glow discharges are:

(i) High energy electrons oscillating between the sheaths of the opposing walls. Electrons emitted via secondary electron emission or thermal emission from the walls are accelerated by the sheath potential and can fall into a kind of pendulum motion between the walls, enhancing ionisation in the bulk and sheaths [58].

(ii) The secondary electron emission from the cathode plays an important role in the discharge, and is mainly caused by positive ions impacting the surface.

(iii) Photoemission from the surface, caused by high energy photons from the bulk of the hollow cathode discharge, further enhances the density of the discharge.

(iv) Due to the hot oscillating electrons ionisation processes can happen inside the sheath (α-processes). The gas pressure inside the electrode can be higher than in the rest of the reactor, and even almost independent of the reactor pressure [57].

(v) The dense discharge heats up the cathode walls by ion bombardment, leading to thermionic emission. At high RF powers this can lead to an arc regime - it is probably this that causes the most severe damage to PECVD reactors.

(vi) The ion bombardment and high cathode temperature can lead to damage to the cathode walls, and the material removed (by sputtering, evap-

oration or melting) can be ionised and will further enhance the discharge.

(vii) The RF plasma outside of the hollow cathode acts as a virtual anode.

Taken together, these differences mean that hollow cathodes present both a danger and an opportunity for plasma processing. A danger, because they can damage PECVD reactors when occurring as parasitic plasmas in an RF discharge, and an opportunity because their high plasma density makes them very efficient at dissociating the gas precursors, and as such could be used as radical-source for new PECVD reactors.

In this chapter research into the type of hollow cathodes that could burn in pumping grids and/or showerheads is presented. We can detect metal lines in optical emission spectroscopy of argon discharges, proof that the electrode walls are affected by the discharge. Lastly, research sparked by an idea from U. Kroll of Oerlikon led to a development of a new plasma source [59].

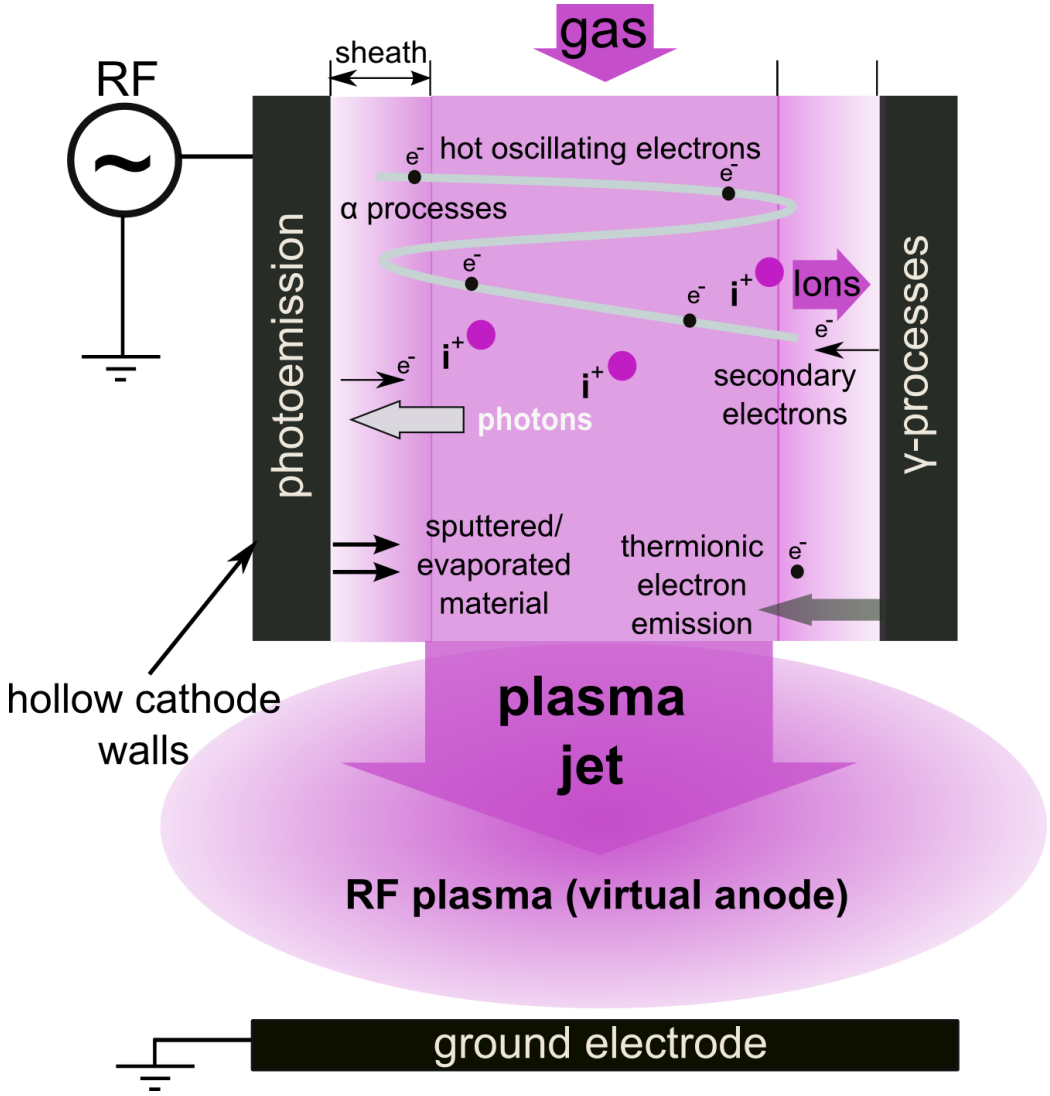

Figure 6.1: Simplified schema for a RF hollow cathode discharge, after [57].

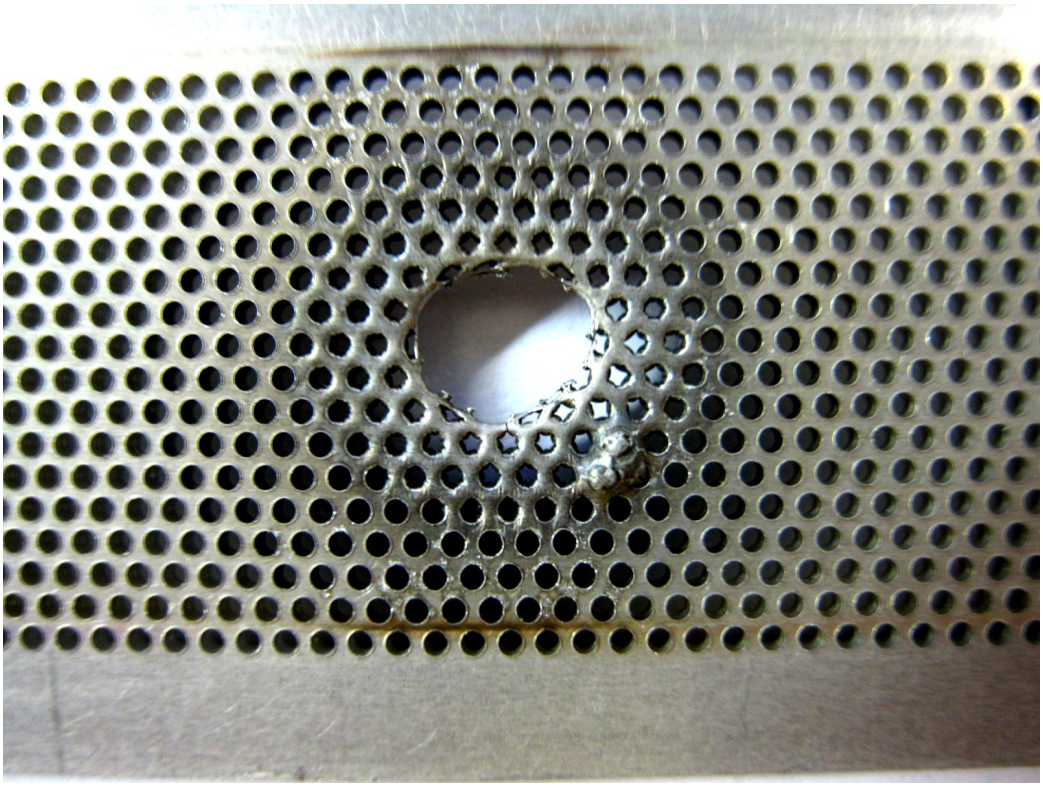

Figure 6.2: Pumping grid of a Very Large Area PECVD reactor, damaged in operation.

6.1 Motivation

With new processes like μc-Si:H layers demanding more power, and ever-larger reactor areas doing the same, once innocuous parasitic plasmas like small hollow cathodes burning in pumping grids and showerheads can damage reactors. The danger lies mainly in starting a runaway-process, where the parasitic plasma starts, for whatever reason, to represent a lower impedance than the normal glow discharge. Naturally, more power will flow to it, intensifying the discharge, and under certain circumstances this in turn lowers the impedance of the discharge again, which eventually leads to a large part of the power of the reactor (tens of kW) to go into a small area. Automatic matching will adapt to the altered impedance, maintaining full RF power to the hollow cathode, destroying the reactor in a worst-case scenario.

Figure 6.2 shows a close-up of a pumping grid that suffered an event similar to the one described above, melting a centimetre-wide hole into it. It was fairly easy to get hollow cathodes to burn in the same pumping grid

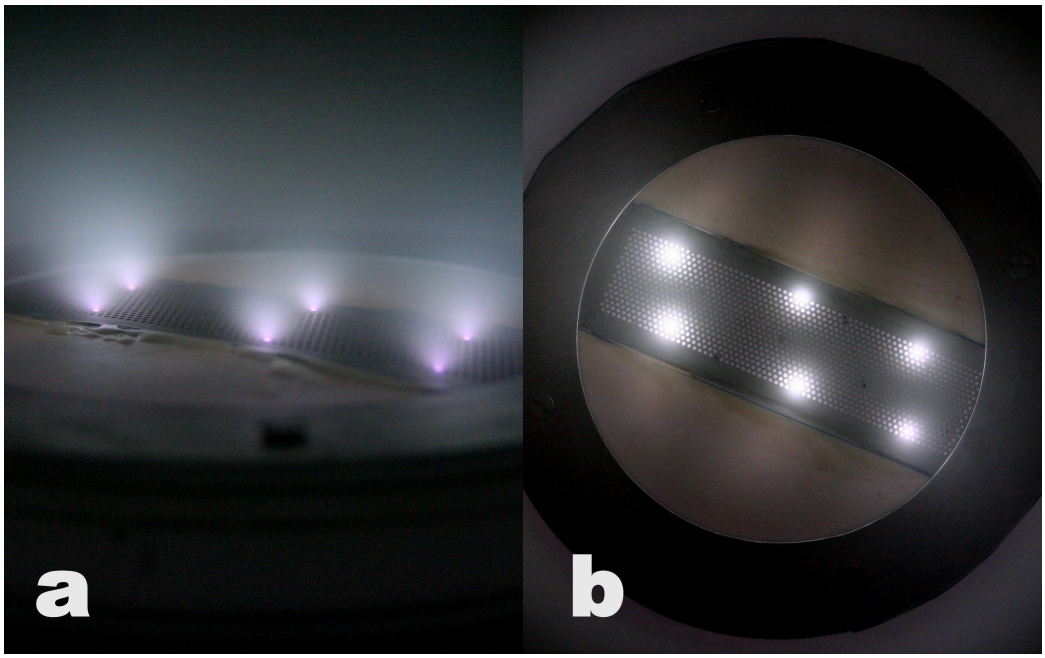

Figure 6.3: Hollow cathodes burning in a pumping grid in argon, 1 mbar, 105 V_{pp}. The hole diameter is 0.6 mm. The grid is screwed to the RF electrode in an RF glow discharge, with a gap of 4 mm between them.

as shown in figure 6.2, see figure 6.3 for an example in argon at 1 mbar of pressure, photographed from the side (a) and above (b).

To simplify the experiment, the decision was taken to concentrate on a plate with a single hole in it, since we were unable to predict where the hollow cathode would strike in a pumping grid, which made positioning of the optical emission spectrometer difficult.

6.2 Evidence of sputtered/evaporated wall material

To find out if a hollow cathode would be hot enough to damage a PECVD reactor, optical spectroscopy was used to detect metal lines in the plasma. 1.5 mm thick brass and aluminium plates with a 1 mm hole in the middle were used to ignite a hollow cathode. The resulting spectra are shown in figure 6.4, while a photo of the hollow cathode can be seen in figure 6.5, burning in argon, with an aluminium electrode. The spectra in figure 6.4 clearly show that the electrode is being damaged; Strong copper and zinc lines are visible

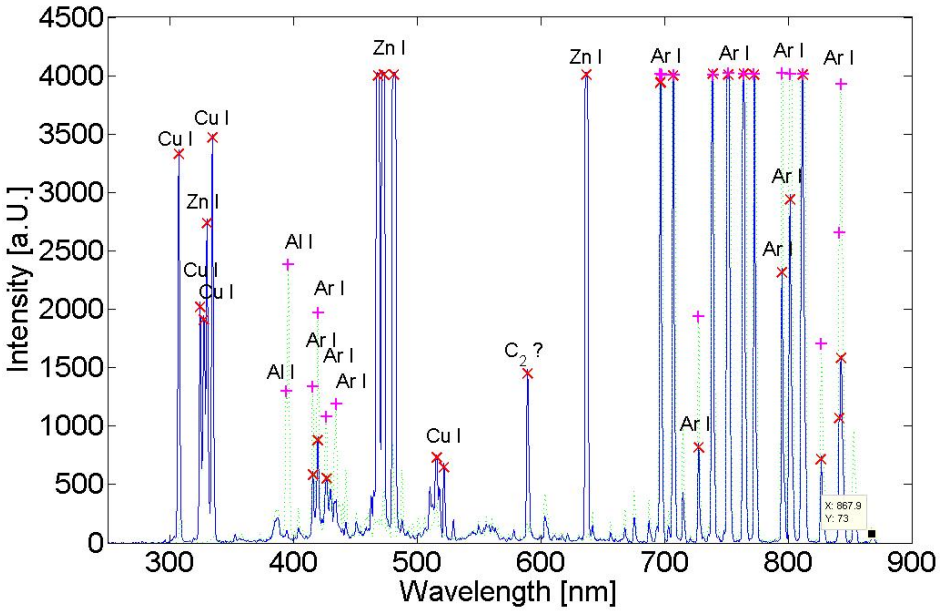

Figure 6.4: Spectra of hollow cathodes in 1 mbar argon, with a brass (solid line, crosses) and an aluminium (dotted line, plusses, see also figure 6.5) electrode. Major spectral lines are labelled above the peak.

around 320 nm, and the strong zinc lines at 468, 472 and 481 nm as well as 636 nm in case of the brass electrode, and aluminium lines around 420 nm for the aluminium electrode. The zinc lines around 470 nm and strongest argon lines at 700+ nm are saturated, because of the spectroscopes minimum integration time of 3 ms, and to show the smaller peaks more clearly. The line at 587 nm could not be identified with certainty, it could be a line of the Swan-band from carbon contamination.

The spectral lines were identified using [30] and [60]. Since metal lines are in fact detected, it follows that the electrode is being damaged by the hollow cathode, at RF voltages not too dissimilar from industrial processes. Hollow cathodes therefore should be avoided in industrial reactors if at all possible. Not only is there a danger of damage to the reactor, but the deposition plasma can be contaminated and the quality of the deposited layer reduced.

Furthermore, this might be contraindication for use of hollow cathodes in large-area PECVD reactors - as the surface area and number of hollow cathodes grows, the danger of one of the cathodes running hot and melting the surrounding electrode grows accordingly, especially as in a larger reactor much more power is also available. Even if no runaway process is started, wear on the hollow cathode holes would at least indicate the need for a

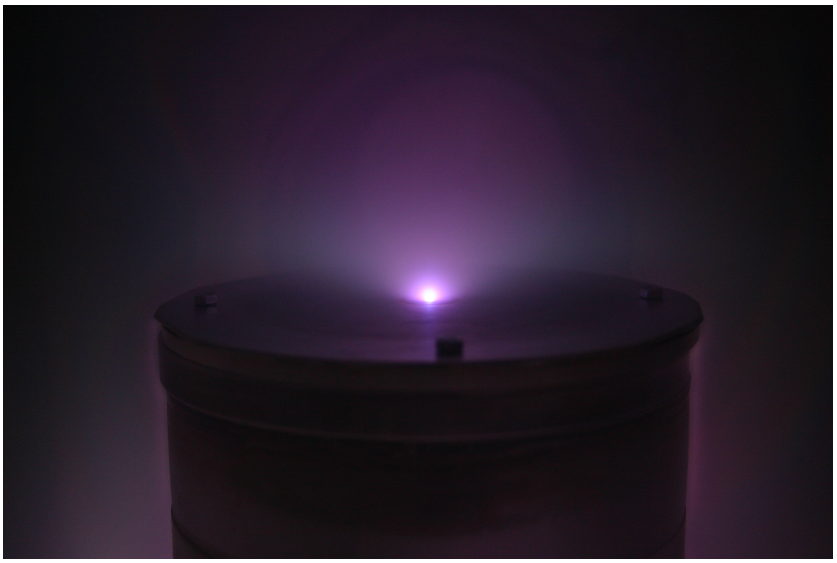

Figure 6.5: Hollow cathode, aluminium electrode in argon, 1 mbar, 250 W RF, 118 V_{pp}.

reactor-design with easily exchangeable electrodes.

While not used in industrial reactors due to its low thermal stability, Teflon (Polytetrafluoroethylene) is often used in research as an insulator. Care has to be taken to shield it from contact with plasma however, since it will contaminate the plasma with CF_4. Furthermore, re-deposition of Teflon on other reactor parts will result in an insulating layer that can charge up in a glow discharge, a problem especially for delicate scientific instruments like retarding field energy analysers. An extreme case is shown in figure 6.6, where Teflon was used as a spacer below the plate containing the hole for the hollow cathode. The spectrum of the discharge is shown in figure 6.7, and the identification of the continuum between 400 and 800 nm posed quite a problem. A comparison with a CF_4 discharge (see figure 6.8) showed the culprit to be degrading Teflon, as a discharge in CF_4 will show two continua of chemoluminescence [61, 62, 63], between 450 and 800 nm due to CF_3^* prevalent at low power, and between 280 and 480 nm due to CF_2^*, dominant at high power. The line at 388 nm could not be positively identified, it is probably an overlapping of C_2 and Fe from the electrode.

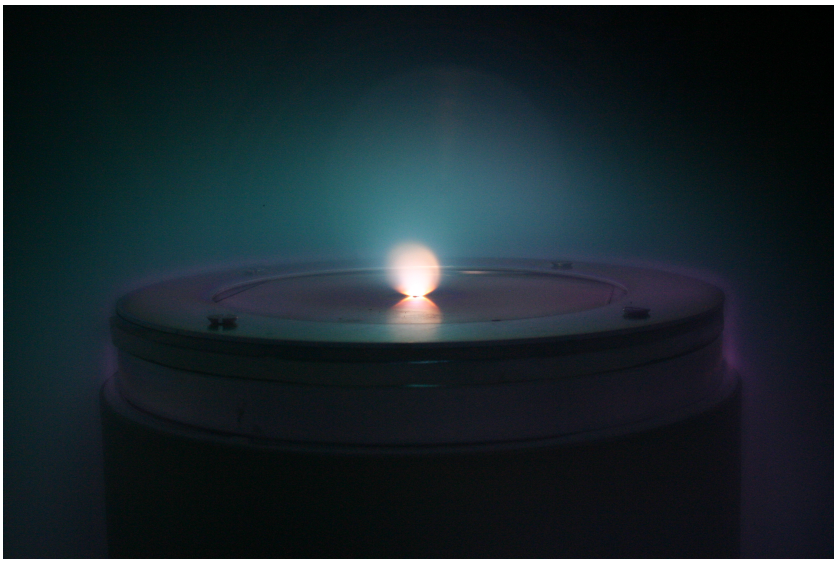

Figure 6.6: Hollow cathode, aluminium electrode in an argon discharge, 1 mbar, 100 W RF, 87 V_{pp}. The electrode plate is screwed to the RF electrode, with a 4 mm high Teflon ring as a spacer. The yellow plume is due to Teflon contamination, see spectrum in figure 6.7.

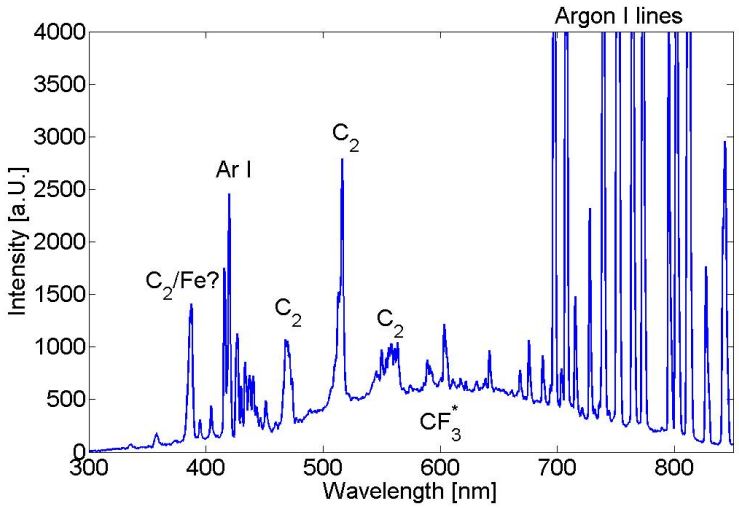

Figure 6.7: Optical spectrum of the hollow cathode in figure 6.6. The CF_3^* continuum is clearly visible, as well as the C_2 Swan-bands. Compare the CF_4 spectrum in figure 6.8.

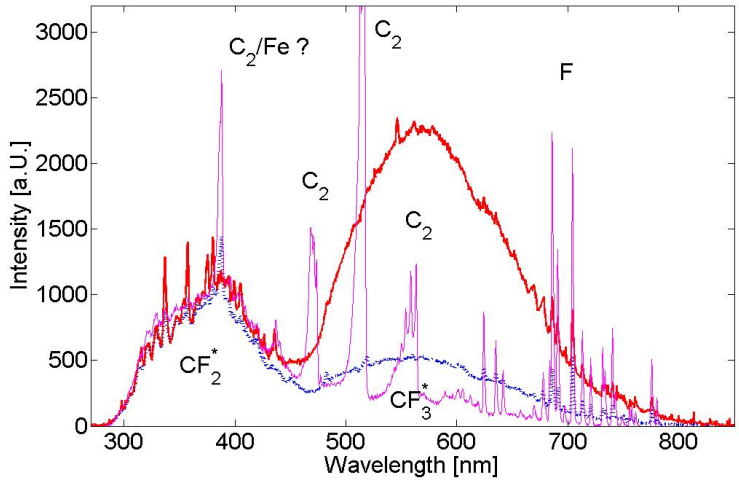

Figure 6.8: CF_4, glow discharge at 40 W/120 V_{pp} (thick solid red line), hollow cathode at 200 W/160 V_{pp} (dash-dotted blue line) and hollow cathode at 400 W/190 V_{pp} (thin magenta line), at 1 mbar.

6.3 Avoiding hollow cathodes

Experiments were carried out to determine at which pressure for a given diameter hollow cathodes would ignite in argon. To simulate a pumping grid, holes with a diameter of 1.4 to 2.2 mm where drilled into a 1 mm thick stainless steel plate. The plate was then mounted to the RF electrode, with a gap of 1.6 mm and 2.8 mm between them. Figure 6.9 shows the pressures at which hollow cathodes could be made to ignite in the holes. The distance to the RF electrode plays a major role in determining if hollow cathodes ignite. Furthermore, the spacing of the holes also seems to matter: While no hole smaller than 1.4 mm diameter could be made to ignite in this experiment, a pumping grid with 0.6 mm holes was able to sustain multiple hollow cathodes in a discharge (see figure 6.3).

No hard and fast rule for avoiding hollow cathodes could be drawn from the experiments, and further work in understanding RF hollow cathode discharges is necessary to discover such. For now, it is necessary to test pumping grids, showerheads and similar structures in a geometry and with plasma parameters as close as possible to their eventual application, to ensure their performance in the industrial reactor later on.

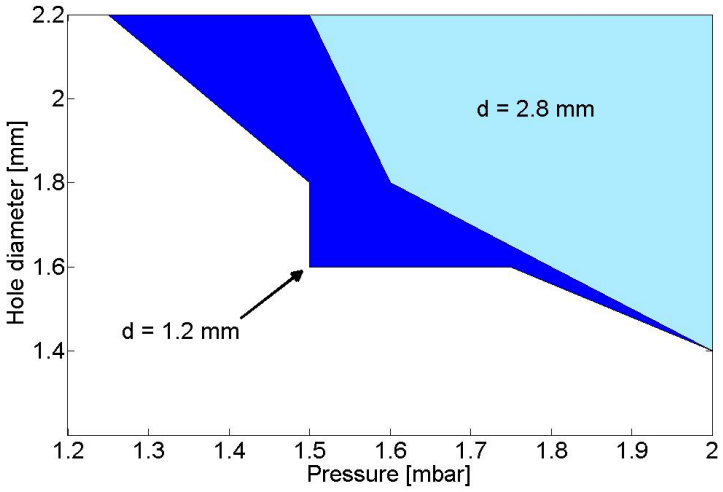

Figure 6.9: Ignition of hollow cathodes in argon, for a separation of the holeplate from the RF electrode of 1.2 and 2.8 mm. Hollow cathodes will ignite in the parameter space covered by the both the dark and light area for a 1.2 mm separation, and in the lighter area for a 2.8 mm separation.

6.4 Grounded grid

An important outcome of the research into hollow cathodes was a patent [59] in collaboration with Oerlikon, for a new plasma source using hollow cathodes. The basic idea is to have a plasma burning in the holes of a grounded grid plate, with the RF electrode close. The substrate would be farther away, also resting on a ground electrode. As the plasma would be confined behind or in the grounded grid, with at the most a decaying plasma left to contact the substrate, the most energetic ions should be screened out, while radicals can still pass the grid to deposit on the substrate. Since high-energy ions have been shown [64] to degrade, causing defects in silicon thin-film deposition, this could result in better quality μc-Si:H-films.

Figure 6.10 shows an early prototype - the RF electrode is below, and a CF_4 plasma is burning in the holes of the grounded grid, which is separated from the RF electrode by a gap of 1 mm.

Another prototype can be seen in figure 6.11, a plate covered with 8 mm diameter holes, with an argon plasma burning in all of them. This plate was used to make the carbon deposition shown in figure 6.12 as a proof of concept, using acetylene as a working gas. The non-uniformity in the centre is probably due to the lack of a showerhead, as the gas was only supplied to the vacuum chamber.

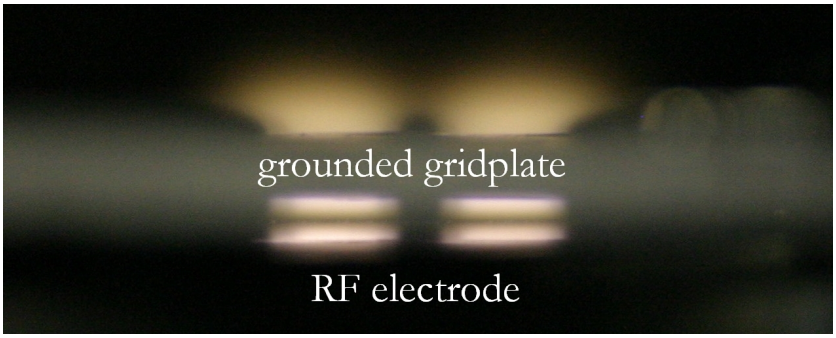

Figure 6.10: Hollow cathode burning in a 2x2 8 mm diameter grounded grid (1 mm gap to RF electrode). 1.2 mbar CF_4, 100 W RF. Seen from the side, the plasma burns only in the four holes in the grid. The gap between the grounded grid and the RF electrode is plasma free. The lowest yellow spots are the reflection on top of the RF electrode of the light given off by the plasma.

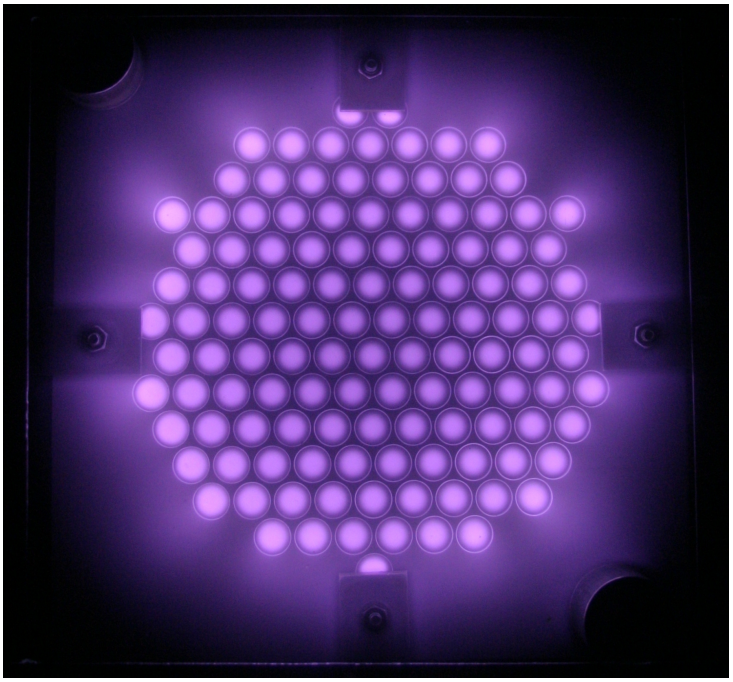

Figure 6.11: Hollow cathodes burning in a gridplate with 8 mm diameter holes in 1 mbar argon. The gap between gridplate and RF electrode was 1 mm.

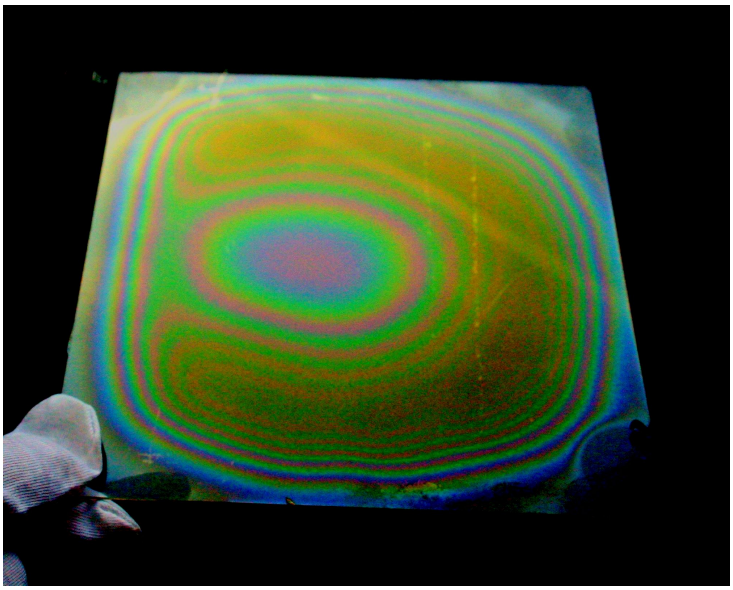

Figure 6.12: Colour-enhanced photo of a carbon deposit using acetylene plasma.

With the success of the prototype, the research was spun off in another doctorate, by M. Cheseaux [65], which should be published in 2012.

Chapter 7

Conclusion and Future Work

This work presented an investigation into two of the four arcing and parasitic plasma events identified by members of the industry [13], namely RF non-contact breakdown across gaps (mm, cm) in absence of plasma, and RF plasma hollow cathodes. A small research reactor was turned into a test-bed for components of large area PECVD reactors, providing better access and faster experimental turn-over as well as the possibility to isolate phenomena from the rest of an already complex machine, which simplifies their study.

For breakdown across millimetric gaps, experiments and simulations show that for pressures of the millibar range, sharp corners play a negligible role in RF breakdown. This was shown by the fact that protruding wires, even if they stretch for more than half the inter-electrode gap-width between parallel plate electrodes, do not change the breakdown curve from that of undisturbed parallel plates. This despite the fact that the electric field at the tip of the wire was shown to be 52 times higher than the equivalent parallel plate field.

Rather, the RF breakdown voltage in irregular gaps is dominated by the extrema of the gap-width, providing the protrusions/holes are wide enough. This conclusion is supported by an extension of the analytical work done by Kihara and Lisovskiy et al. The breakdown curve of a structured electrode will be a mix of the parallel plate equivalents of the various gap-widths present. This was shown by multiple breakdown experiments in argon and hydrogen, featuring cylindrical protrusions and holes between parallel plates. Breakdown for a given pressure can be shown to happen at the location whose parallel plate equivalent with the same gap-width has the lowest breakdown voltage, as long as the feature in question is wide enough so that electron diffusion to walls or the surrounding, wider gap can not overcome the effect. This diffusion is the reason why wires or other, narrow features will not influence the breakdown voltage.

In short, if the goal is to prevent breakdown between the electrodes,

for example using dark space shielding in showerheads of industrial plasma deposition reactors, then the design rule to follow is to examine the geometry for the largest and smallest gap, whose parallel plate equivalents will then give the maximum sustainable voltage before breakdown. Conversely, the same method can be used to predict breakdown voltages for plasma reactors with structured electrodes.

With the breakdown simulation presented in chapter 5, we have developed a tool that can be used to predict the breakdown location for arbitrary geometries. The simulation was used to confirm that breakdown will, for example, happen on top of protrusions for high pressures, and in holes for low pressures, as long as those features are wide enough, as explained above. Furthermore, the simulation provides an excellent tool for the design of dark space shielding, as possible danger spots for RF breakdown can be identified already in the design stage, and the design improved. With this, there is less need for relatively costly experiments during reactor design.

RF plasma hollow cathodes were shown to be a danger to plasma deposition reactors. Not only can they lead to catastrophic failure (this was unfortunately already known to the industry), but electrode material sputtered and/or evaporated by the hollow cathode can contaminate the deposition plasma, reducing the quality of the deposited layers. We have also shown that care has to be taken with isolating material in contact with plasma, as it, too, can degrade and contaminate the experiment, both by its presence in the plasma and by re-deposition on instruments or walls. While it was not possible to develop design-rules for the avoidance of hollow cathodes in the available time, which was largely due to the complexity of the phenomenon and its dependence on a large amount of parameters such as pressure, gas type, power density, RF voltage, hole diameter and spacing and the presence or absence of other hollow cathode discharges, we could show that hollow cathodes and components of industrial reactors prone to the ignition of hollow cathodes can be studied easily in a small research reactor like the one described in this work.

Finally, as a small side project, a new plasma source using hollow cathodes was developed following an idea of U. Kroll of Oerlikon.

Future Work

All of the four categories identified by the industry as parasitic plasmas and arcing events could be studied. The remaining two, RF breakdown in micron gaps between surfaces which are nominally in contact and RF plasma with insulating layers & DC circulating currents are still worthy of study,

and will continue to present a problem as reactor sizes and their RF power requirements increase.

The breakdown simulation developed in this work could be extended to incorporate surface effects such as secondary electron emission, which would improve the simulation especially at low pressures.

Much remains to be done to further the understanding of RF hollow cathodes, especially as it translates to design rules for their avoidance in industrial reactors. Ignition conditions for different gases, electrode materials and geometries need to be understood much better.

Bibliography

[1] H. Schmidt. *Characterization of a high-density, large area VHF plasma source*. PhD thesis, Ecole Polytechnique Fédérale de Lausanne, 2006.

[2] B. Strahm. *Investigations of Radio-Frequency, Capacitively-Coupled Large Area Industrial Reactor: Cost-effective Production of Thin Film Microsrystalline Silicon for Solar Cells*. PhD thesis, Ecole Polytechnique Fédérale de Lausanne, 2007.

[3] M A Lieberman, J P Booth, P Chabert2, J M Rax, and M M Turner. Standing wave and skin effects in large-area, high-frequency capacitive discharges. *PSST*, 11:283, 2002.

[4] A. A. Howling, L. Sansonnens, J. Ballutaud, Ch. Hollenstein, and J. P. M. Schmitt. Nonuniform radio-frequency plasma potential due to edge asymmetry in large-area radio-frequency reactors. *J. Appl. Phys.*, 96(10):5429, 2004.

[5] H. Schmidt, L. Sansonnens, A. A. Howling, Ch. Hollenstein, M. Elyaakoubi, and J. P. M. Schmitt. Improving plasma uniformity using lens-shaped electrodes in a large area very high frequency reactor. *Journal of Applied Physics*, 95(9):4559 –4564, 2004.

[6] L Sansonnens, A A Howling, and Ch Hollenstein. Electromagnetic field nonuniformities in large area, high-frequency capacitive plasma reactors, including electrode asymmetry effects. *PSST*, 15:302, 2006.

[7] J.D. Huba. *NRL Plasma Formulary*. Naval Research Laboratory, Washington, 2009.

[8] M. A. Lieberman and A. J. Lichtenberg. *Principles of plasma discharges and materials processing*. John Wiley and Sons, Inc., New York, 1994.

[9] W. Crookes. Cathode rays. In *Cathode Rays*, Philadelphia, PA, 1879. James W. Queen & Co.

[10] J. J. Thomson. Cathode rays. *Philosophical Magazine*, 44:293, 1897.

[11] I. Langmuir. Oscillations in ionized gases. *Proc. Nat. Acad. Sci. U.S.*, 14:628, 1928.

[12] William R. Stowell. Ion-plated titanium carbide coatings. *Thin Solid Films*, 22(1):111 – 120, 1974.

[13] Ch Ellert. Arcing in PECVD reactors. private communication, 2007.

[14] H. B. Smith, C. Charles, and R. W. Boswell. Breakdown behaviour in radio-frequency argon discharges. *Phys. Plasmas*, 10(3):875–881, 2003.

[15] T. Kihara. The mathematical theory of electrical discharges in gases. *Rev. Mod. Phys.*, 24(1):45–61, 1952.

[16] P.T. Farnsworth. Television by electron scanning. *J. Franklin Inst.*, 218(4):411–444, 1934.

[17] J.R.M. Vaughan. Multipactor. *IEEE Trans. Electron Devices*, 35(7):1172–118, 1988.

[18] Y. Raizer. *Gas Discharge Physics*. Springer, Berlin, 1991.

[19] H. B. Smith. Studies of plasma breakdownand decay in a capacitive rediofrequency argon discharge. *Phys. Plasmas*, 5(9):3469–3476, 1998.

[20] A. Fick. Ueber Diffusion. *Poggendorff's Annel. Physik.*, 94:59Ű86, 1855.

[21] V. A. Lisovskiy and V. D. Yegorenkov. RF breakdown of low-pressure gas and a novel method for determination of electron-drift velocities in gases. *J. Phys. D: Appl. Phys.*, 31:3349–3357, 1998.

[22] M. L. Boas. *Mathematical Methods in the Physical Sciences*. John Wiley & Sons, Inc., New York, 1966.

[23] P. J. Chantry. A simple formula for diffusion calculations involving wall reflection and low density. *J. Appl. Phys.*, 62(4):1141–1148, 1987.

[24] B. Legradic, A. A. Howling, and C. Hollenstein. Radio frequency breakdown between structured parallel plate electrodes with a millimetric gap in low pressure gases. *Phys. Plasmas*, 17(10):102111, 2010.

[25] M. Sato and M. Shoji. Breakdown characteristics of rf argon capacitive discharge. *Jpn. J. Appl. Phys.*, 36:5729–5730, 1997.

[26] V. A. Lisovskiy, J.-P. Booth, K. Landry, D. Douai, V. Cassagne, and V. Yegorenkov. A technique for evaluating the rf voltage across the electrodes of a capacitively-coupled plasma reactor. *Eur. Phys. J. Appl. Phys.*, 36:177–182, 2006.

[27] Momčilo M. Pejović and G. S. Ristić. Analysis of mechanisms which lead to electrical breakdown in argon using the time delay method. *Phys. Plasmas*, 9(1):364–370, 2002.

[28] Momčilo M. Pejović, E. N. Živanović, and Milić M Pejović. Kinetics of ions and neutral active states in the afterglow and their influence on the memory effect in nitrogen at low pressures. *J. Phys. D: Appl. Phys.*, 37:200–210, 2004.

[29] R. Ludwig and P. Bretchko. *RF Circuit Design*. Tom Robbins, Upper Saddle River, New Jersey, 2000.

[30] J. Reader, C.H. Corliss, W. Wiese, and G. A. Martin. *Wavelengths and Transition Probabilities for Atoms and Atomic Ions*. US Department of Commerce, Washington, DC, 1980.

[31] S. M. Levitskii. An investigation of the sparking potential of a rf discharge in a gas in the transition range of frequencies and pressures. *Sov. Phys. - Tech. Phys.*, 2:887–893, 1958.

[32] V. A. Lisovskiy, S.D. Yakovin, and V. D. Yegorenkov. Low-pressure gas breakdown in uniform dc electric field. *J. Phys. D: Appl. Phys.*, 33(21):2722, 2000.

[33] V. Lisovskiy, J.-P. Booth, K. Landry, D. Douai, V. Cassagne, and V. Yegorenkov. Similarity law for rf breakdown. *EPL (Europhysics Letters)*, 82(1):15001, 2008.

[34] V Baglin, J Bojko, O Gróbner, B Henrist, N Hilleret, C Scheuerlein, and M Taborelli. The secondary electron yield of technical materials and its variation with surface treatments. *Proceedings of EPAC 2000, Vienna, Austria*, pages 217–221, 2000.

[35] H.A. Bethe. *Handbuch der Physik*, volume 24. Julius Springer Verlag, Berlin, 1933.

[36] J. R. Young. Penetration of electrons in aluminum oxide films. *Phys. Rev.*, 103(2):292–293, Jul 1956.

[37] F. M. Penning. Ueber Ionisation durch metastabile Atome. *Naturwissenschaften*, 15(40):818, 1927.

[38] Dimitris P. Lymberopoulos and Demetre J. Economou. Fluid simulations of glow discharges: Effect of metastable atoms in argon. *J. Appl. Phys.*, 73(8):3668, 1993.

[39] W. M. Haynes. *CRC Handbook of Chemistry and Physics*. Taylor and Francis Group, LLC, Boulder, Colorado, 91 edition, 2011.

[40] J. W. D. Connolly and K. H. Johnson. Calculation of the ionization energies of the sulphur hexafluoride molecule by the multiple scattering method. *Chemical Physics Letters*, 10(5):616 – 622, 1971.

[41] P. A. Chatterton. A theoretical study of field emission initiated vacuum breakdowns. *P. Phys. Soc.*, 88(1):231–245, 1966.

[42] G. E. Vibrans. Vacuum voltage breakdown as a thermal instability of the emitting protrusion. *J. Appl. Phys.*, 35(10):2855–2857, 1964.

[43] V. A. Lisovskiy and V. D. Yegorenkov. Low pressure breakdown in combined fields. *J. Phys. D: Appl. Phys.*, 27:2340–2348, 1994.

[44] V. A. Lisovskiy, S. Martins, K. Landry, D. Douai, J.-P. Booth, V. Cassagne, and V. D. Yegorenkov. The effect of discharge chamber geometry on the ignition of low-pressure RF capacitive discharges. *Phys. Plasmas*, 12:093505, 2005.

[45] J. Bambring. Driftgeschwindigkeit von Elektronen in Argon. *Z. Phys. A*, 179:539–543, 1964.

[46] H. N. Kücükarpaci and J. Lucas. Electron swarm parameters in argon and krypton. *J. Phys. D: Appl. Phys.*, 14:2001–2014, 1981.

[47] V. A. Lisovskiy, J.-P. Booth, K. Landry, D. Douai, V. Cassagne, and V. Yegorenkov. Electron drift velocity in argon, nitrogen, hydrogen, oxygen and ammonia in strong electric fields determined from rf breakdown curves. *J. Phys. D: Appl. Phys.*, 39:660–665, 2006.

[48] D. J. Rose. Townsend ionization coefficient for hydrogen and deuterium. *J. Phys. D: Appl. Phys.*, 104:273–277, 1956.

[49] W. Roznerski. The ratio of lateral diffusion coefficient to mobility for electrons in hydrogen and nitrogen. *J. Phys. D: Appl. Phys.*, 11:197–201, 1978.

[50] W. Roznerski, J. Mechlińska-Drewko, and K Leja. The characteristic energy and ratio of longitudinal diffusion coefficient to mobility for electrons in hydrogen and nitrogen. *J. Phys. D: Appl. Phys.*, 23:1461–1463, 1990.

[51] G. J. M. Hagelaar and L.C. Pitchford. Solving the boltzmann equation to obtain electron transport coefficients and rate coefficients for fluid models. *Plasma Sources Sci. T.*, 14:722–733, 2005.

[52] COMSOL Inc. http://www.comsol.com.

[53] MathWorks. http://www.mathworks.com.

[54] F. Paschen. Bohrs Heliumlinien. *Ann. Phys.*, 355(16):901–940, 1916.

[55] H. Eichhorn, K. H. Schoenbach, and T. Tessnow. Paschen's law for a hollow cathode discharge. *Applied Physics Letters*, 63(18):2481 –2483, November 1993.

[56] A. D. White. New hollow cathode glow discharge. *J. Appl. Phys.*, 30(5):711 –719, May 1959.

[57] L. Bárdoš. Radio frequency hollow cathodes for the plasma processing technology. *Surf. Coat. Tech.*, 86-87:648–656, 1996.

[58] P.F. Little and A. von Engel. The hollow-cathode effect and the theory of glow discharges. *Proc. Roy. Soc.*, 224:209, 1954.

[59] U. Kroll and B. Legradić. Plasma processing apparatus and method for the plasma processing of substrates, 2009. PCT/EP2009/055302.

[60] R.W.B Pearse and A. G. Gaydon. *The Identification of molecular spectra.* John Wiley & Sons, Inc., New York, 2 edition, 1950.

[61] W.R. Harshbarger, R.A. Porter, T.A. Miller, and P. Norton. A study of the optical emission from an RF plasma during semiconductor etching. *Appl. Spectrosc.*, 31(3):201, 1977.

[62] Masako Suto and Nobuaki Washida. Emission spectra of CF3 radicals I. *J. Chem. Phys.*, 78(3):1007, 1983.

[63] T.Y. Jung, D. H. Kim, and H.B. Lim. Molecular emission of cf4 gas in low-pressure inductively coupled plasma. *Bull. Korean Chem. Soc.*, 27(3):373, 2006.

[64] A.H.M. Smets and M. Kondo. The role of ion-bulk interactions during high rate deposition of microcrystalline silicon by means of the multi-hole-cathode vhf plasma. *Journal of Non-Crystalline Solids*, 352(9-20):937 – 940, 2006.

[65] M. Cheseaux. PhD Thesis, Ecole Polytechnique Fédérale de Lausanne. To be published, 2012.

Acknowledgements

Writing a thesis is a long and often torturous process, and I could not have done it without the help of the many kind people who lent a hand. First among those are of course my supervisors, Christoph Hollenstein and Alan Howling, whom I have to thank not only for accepting me as a PhD candidate, but also for putting up with all my mistakes and the sometimes glacial progress of my work. Through long and frequent discussions and with quite a bit of patience they transformed the flailing proto-scientist I was at the beginning of this work into somebody who can submit his thesis to the almighty *école doctorale*. Thanks!

This work would not have been possible without the help and input by our partners in the industry, notably Christoph Ellert, Ulrich Kroll and Stefan Rhyner from Oerlikon, whose data on plasma breakdown in industrial reactors and technical advice was invaluable.

I would also like to thank the members of my jury, Christophe Ballif, Christoph Ellert and Jean-Paul Booth for being interested enough in my work to come all the way to Lausanne for my thesis defence.

Further thanks should go to my colleagues, Alban, Ben, David & David, Marina, Michael, Lukas, Sylvain, Ralph and Phillipe:

Alban, Ben and Lukas, for welcoming me to the group and showing me how stuff worked, especially Ben who even let me play with his reactor, even though it was near the end of his thesis, a very courageous thing to do.

Marina, who started a month before me and kept the destruction in the lab to a minimum, and for showing us that Italian families really care.

David M., who never would say no to a game of darts, and David G. who not only kept me supplied with coffee after lunch, but kept me from being the last at darts by virtue of being even worse than I.

Ralph, for showing me how you are supposed to play darts, and for still having the guts to start his PhD with our group after suffering through his masters thesis with me as a supervisor.

Michael, for not wrecking my car while learning to drive, for inviting me to his role-playing group and for quite a few shared beers.

Sylvain for putting up with having his desk next to mine, and for suffering quietly while my jungle of house plants expanded.

Phillipe, for helping me with the terror that is the obligatory French abstract, and for pounding the concepts of matching in my stubborn head.

I would also like to thank all the technicians of the CRPP who helped me with my experiments, especially the mechanics, who were always most accommodating in translating my cryptic drawings into mechanical masterpieces.

Many thanks go to the secretaries as well, Céline, Edith, Heidi, Hugo, Nadia, Séverine and Véronique, who helped me immensely in navigating the Byzantine bureaucracy of the EPFL, and made sure I had all my forms in order.

I also have to thank my friends in Austria, too numerous to name, for keeping in contact and making sure that after my annual winter holidays back home I usually needed at least another week of recuperation, thanks to many-a 'Krug'.

Thanks go also to Charlotte, not only for being the reason I came to Switzerland in the first place, but also for keeping me grounded: angsting over the latest deadline seems silly when your friend is telling you stories about her helicopter nearly getting shot down in Darfur.

A big part of keeping me sane was also due to my friends and colleagues at the martial arts school 'Són Long Quền Thuật', where I could work off any accumulated frustration over experiments that just would not work by getting pounded on twice a week. Nothing is better for your health, mental or otherwise, than a regular thrashing, or so they maintain.

Speaking of taking a beating, I'd better thank my family for all the support they have given me (and for being properly horrified by all the injuries I sustained in working off my frustrations): My parents for always encouraging my interest in science and my love for reading - I hope when it is my time being a parent I will do half as well as you! My sisters for still loving their continually absent brother, and my nephews for forgiving me that I always have and always will give them books as presents. Last but not least I must thank my beautiful Fabiana, for making the otherwise stressful last months of my doctorate a complete joy: Ti amo!